Design and Fabrication of Thermo – Mechanical Thermal Detector Arrays with Optical Readout

by

Hamdi Torun

A Thesis Submitted to the
Graduate School of Engineering
in Partial Fulfillment of the Requirements for
the Degree of

Master of Science

in

Electrical & Computer Engineering

Koc University

August 2005

Koc University

Graduate School of Sciences and Engineering

This is to certify that I have examined this copy of a master's thesis by

Hamdi Torun

and have found that it is complete and satisfactory in all respects,
and that any and all revisions required by the final
examining committee have been made.

Committee Members:

_____

Hakan Ürey, Ph. D. (Advisor)

_____

Erdem Alaca, Ph. D.

_____

Alper Kiraz, Ph. D.

Date: _____

ABSTRACT

Infrared (IR) imaging technology has found many important application areas such as military, automobile heads-up-displays (HUD), medical diagnostics, surveillance for security, victim search for rescue teams, non – destructive testing for industrial applications, and geo – thermal event detection for environmental control.

In this thesis, design and realization of an uncooled opto – mechanical IR detector with optical readout is presented. It is shown that our calculated noise equivalent temperature difference (NETD) is <10 mK including the readout noise sources (assuming 50um pixels, f/1 optics and 60Hz frame rate). This performance level is far superior to the other current state-of-the-art uncooled microbolometer-based detector arrays and is comparable to that of the best cooled IR detector arrays, which are far more complicated and expensive compared to the uncooled counterparts. In addition to the high-performance, the architecture proposed is scalable to high-resolutions as the pixel readout is based on an integrated diffraction grating and the pixelated readout electronics is completely eliminated by the use of MEMS scanners for the serial pixel readout.

The detector pixels are tiny membranes that are connected to bimaterial legs, which are connected to a substrate through thermal isolation legs. The conversion of IR radiation into temperature difference causes deflection along bimaterial legs. The mechanical deflection is detected optically with sub-nm accuracy using diffraction gratings placed underneath each pixel. Fixed diffraction gratings and the movable pixel membrane form an interferometer. This type of interferometric readout offers operation at detector shot-noise limit using a coherent light source, thus the contribution of the readout noise to the overall system noise level is negligible. Another important advantage of the optical readout is that electrical conductive paths that increase the thermal conduction are not needed. Thus higher sensitivity compared to microbolometers and some of the cooled detectors can be obtained.

As the design prototypes, different design variations for single pixels and small arrays of 3 x 3 pixels were fabricated. The microfabrication was done at Microelectronics Research Center (MIRC), Georgia Institute of Technology, Atlanta-USA. The microfabrication requires 4-lithography masks and uses the following standard IC materials: Silicon Nitride, Aluminum, and Chromium on top of Quartz substrate and is limited to low temperature processes that are below 250 °C.

Keywords: Infrared imaging, thermal image sensors, infrared absorber, bimaterial cantilevers, thermal deformation, diffraction grating, interferometer, microscanners, MEMS, microfabrication.

ÖZET

Kızılötesi görüntüleme teknolojisinin uygulama alanları çok geniştir. Askeri uygulamalar, otomotiv endüstrisi, tıbbi görüntüleme, güvenlik uygulamaları, arama – kurtarma çalışmaları, endüstriyel test ve jeo – termal olay tespiti ile çevre kontrolü belli başlı uygulama alanları olarak sayılabilir.

Bu tezde; optik okumalı, opto – mekanik tipi soğutmasız kızılötesi detektör dizini tasarım ve üretim çalışmaları sunulmaktadır. Detektörler için hesaplanan NETD (*Gürültü Eşlenikli Sıcaklık Farkı*) 10 mK'den daha küçüktür (60 Hz'de okunan 50 μm'lik pikseller için ve f/1 kızılötesi lens ile birlikte). Bu performans seviyesi, en gelişmiş soğutmasız mikrobolometre tipi detektörlerle elde edilecek performanstan çok daha ileride olup; en gelişmiş soğutmalı kızılötesi detektör dizinleri – ki bunlar soğutmasız detektörlere göre çok daha karmaşık ve pahalıdırlar – ile elde edilecek performansla karşılaştırılabilir durumdadır. Piksellere entegre edilmiş dağıtma ızgarası (*diffraction grating*) tabanlı optik okuma ve piksel seviyesinde okuma elektroniği gereksinimini ortadan kaldıran MEMS tarayıcı sayesinde; önerilen konfigürasyon yüksek performansının yanı sıra yüksek çözünürlükte detektör dizini oluşturmaya da uygundur.

Detektör pikselleri çift-katlı bacaklara bağlı küçük zarlardan oluşmaktadır. Zarları tutan çift-katlı bacaklar, termal yalıtım bacakları ile alttaşa (substrate) bağlanmıştır. Emilen kızılötesi ışınların sıcaklık farkına çevrilmesi, çift-katlı bacaklarda bükülmeye yol açar. Bu bükülme her pikselin altına yerleştirilen dağıtma ızgaralarıyla optik olarak nanometre-altı hassasiyetle ölçülmektedir. Sabit dağıtma ızgaralarıyla hareketli piksel zarları girişim-ölçer oluşturmaktadır. Girişim-ölçer sayesinde okuma gürültüsü; okuma için gerekli ışık kaynağının Shot-gürültü seviyesine indirilebilmektedir. Dolayısıyla okuma gürültüsünün toplam gürültüye katkısı ihmal edilebilir.

Tasarım prototipleri olarak, 3 x 3 formatında detektör dizinleri Georgia Institute of Technology, Atlanta – USA bünyesindeki Microelectronics Research Center (MIRC) isimli merkezde üretilmiştir. Kuvars alttaş üzerine Silikon Nitrat, Alüminyum ve Krom materyallerini büyütme ve aşındırma adımlarını içeren mikrofabrikasyon, 4-lithografi maskesine gereksinim duymakta olup, düşük sıcaklıklarda tamamlanabilmektedir (<250°C).

Anahtar Kelimeler: Kızılötesi görüntüleme, termal görüntü sensörleri, kızılötesi emici, çift – katlı kaldıraçlar, termal bükülme, dağıtma ızgarası, girişim ölçer, mikro tarayıcılar, MEMS, mikrofabrikasyon.

ACKNOWLEDGEMENTS

Above all, I would like to express my sincere appreciation to my thesis advisor Prof. Hakan Ürey for his encouragement, support and advice throughout this work. Introducing me to micro-optics and microsystems, the experience and knowledge he taught me is beyond from this thesis. It was always a pleasure for me to be a member of Optical Microsystems Laboratory (OML) under the supervision of Prof. Ürey. Together with him I would like to thank Prof. Levent Degertekin from Georgia Institute of Technology, Atlanta allowing me to spend 4 months with his research group to fabricate the design prototypes. He was always available to give me guidance and encouragement not only in Atlanta but during the entire work. It has been an invaluable experience to work with both Prof. Ürey and Prof. Degertekin.

I also would like to thank Dr. Erdem Alaca and Dr. Alper Kiraz for taking part in my thesis jury.

The most enjoyable part of being a member of OML was to work with Arda, Çağlar, Olgaç, and Özgür. This work would not be complete without their friendship and support. They were the most relaxing times when we had "rakı-balık" together. I want to thank to Çağlar also being a perfect roommate for more than one year.

Many thanks go to Rasim, Wook, Omkar, and Barış for both helping me in cleanroom and helping me to get used to Atlanta. Particularly, I would like to thank Rasim for spending long hours in cleanroom with me. I also want to acknowledge Sherron for her help during my stay in Atlanta and Julian for being a friendly home mate.

It is certain that this thesis would be impossible without the emotional support from my family and Sonya. I appreciate the caring and understanding they have shown (especially towards the end). Thanks to mom, dad, and Hande for their love and unlimited support and to Sonya for adding a meaning to my life.

I'll pay a beer to anyone I forgot.

TABLE OF CONTENTS

LIST OF TABLES

LIST OF FIGURES

NOMENCLATURE

E_λ	the energy emitted per unit volume per unit wavelength from a blackbody
h	Planck's constant
c	speed of light
c	specific heat coefficient
λ	wavelength of the radiation
k	Boltzmann's constant
k	spring constant
T	temperature of the black body
$g(x)$	electron – hole generation rate
r	Fresnel reflection coefficient
t	Fresnel transmission coefficient
E_q	photon irradiance
α	absorption coefficient
J	current density
$n(E)$	number of electrons per unit volume between energy E and E+ΔE
$g(E)$	density of states per unit volume in the energy interval ΔE
$f(E)$	distribution function that an electron is in energy state E
TCR	temperature coefficient of resistance
R_B	bolometer resistance
β	fill – factor
G_e	effective thermal conductance
η	absorption efficiency
i_b	bias current
ω	optical angular frequency
τ_e	effective thermal response time
$NETD$	noise equivalent temperature difference

NEP	noise equivalent power
R	responsivity
D^*	normalized detectivity
L	radiance
M_p	photon exitance
N	number of photons emitted per unit cavity volume of the blackbody target
$\bar{v}$	average velocity of the photons
DOS	density of states
$P(\lambda,T)d\lambda$	power radiated by unit area of a blackbody target in a unit time in a spectral width of dλ
n	real part of complex refractive index
k	imaginary part of complex refractive index
k	thermal conductivity
Δ	accumulated phase
σ_R	real part of the complex conductivity
σ_I	imaginary part of the complex conductivity
ε_0	permittivity of air
$CTE,\ \alpha$	coefficient of thermal expansion
E	Young's modulus
ρ	radius of curvature
f_{no}	f-number
τ_0	transmittance of the medium
$(dP/dT)_{\lambda 1-\lambda 2}$	change in power per unit area radiated by a blackbody at temperature T measured within spectral window λ_1 to λ_2
T_D	detector temperature
T_B	background temperature
σ	Stefan – Boltzmann's constant
Q	quality factor
Δf	bandwidth of the detector
G	thermal conductance

ε	emissivity
g	gravitational constant
μ	viscosity
u_∞	mass average fluid viscosity
ν	kinematic viscosity
Gr_L	Grashof number
Re_L	Reynold number
Λ	period of the diffraction gratings

Chapter 1

INTRODUCTION

Creating the thermal map of the environment finds itself a wide variety of applications in several areas such as medical, military, industrial, and fire fighting. The devices used to generate the thermal map of the targets are passive devices that collect the optical signal radiated from the targets according to Planck's radiation law assuming that the targets behave as black bodies. According to Planck's radiation law, the energy emitted per unit volume per unit wavelength from a blackbody (E_λ) can be expressed as follows:

$$E_\lambda = -\frac{8\pi hc}{\lambda^5}\frac{1}{1-\exp\left(hc/\lambda kT\right)} \tag{1.1}$$

where *h, c,* λ*, k,* and *T* are the Planck's constant, speed of light, wavelength of the radiation, Boltzmann's constant and the temperature of the black body. It is possible to generate the thermal map of the target by detecting the radiated energy since the only parameters that determine the amount of energy are the temperature and the radiation wavelength. The interested spectrum of the radiation is classified as infrared (IR) band and IR band is further divided into bands as a function of wavelength as follows:

- Near IR (NIR): 0.78 – 1 μm
- Short wavelength IR (SWIR): 1 – 3 μm
- Mid – wavelength IR (MWIR): 3 – 5 μm
- Long – wavelength IR (LWIR): 8 – 14 μm
- Very long – wavelength IR (VLWIR): 14 – 100μm

Each of these specific bands has their own properties and specific detector technologies have been developed for these bands. For infrared imaging applications, MWIR and LWIR bands, where the transmittance of the atmosphere is high, are especially important. Transmittance of air is reduced by several factors as a result of scattering and absorption processes. The bands of operation should be selected specifically to each application. For instance, MWIR band is favorable if the target is relatively hot and the weather is clear, on the other hand LWIR band offers high sensitivity in hazy weather conditions. After choosing the operation band, the detector can be designed.

Infrared imaging devices can basically be classified into two main groups according to the detection mechanism. Photon detectors deal directly with the interaction of the incoming photons with the electrons in the detector material. On the other hand, thermal detectors are the devices whose properties can be modulated by its temperature. Therefore, the detection mechanism of thermal detectors is indirect in the sense that the incoming radiation is first converted into heat energy and the generated heat energy is used to change an appropriate material property of the detector.

The infrared imaging device presented in this thesis is a thermal detector in which the incoming radiation is first converted into heat energy and then the heat energy is converted into mechanical energy that deflects the pixels of the detector array. To achieve mechanical deflection, the working principle of thermostats is employed. The pixels in the detector array have structures that are connected to bimaterial layers as shown in Fig.1.1

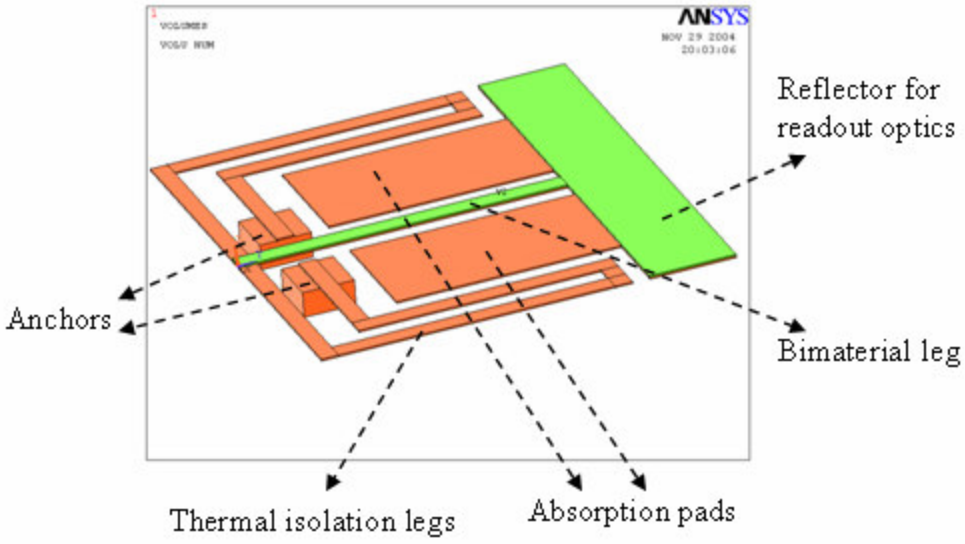

Fig.1.1 Detector schematic of one of the IR detector pixel designs fabricated during this research

Functionlity of the different parts are labeled in the figure and treated in separate chapters of the thesis:

- The incident IR radiation is absorbed by the absorption pads to generate heat energy. IR absorption, IR absorber design and optimization are discussed in Chapter 3. A novel thin-film metal detector combined with an optical resonant cavity is proposed to enhance the absorption and reduce the detector response time.
- The induced temperature difference causes thermal stress on the bimaterial leg and as a result of this the reflector structure bends. The analysis of thermal stresses and deformation is presented in Chapter 4. Compact analytical formulas to compute the thermal deflection of multilayer MEMS structures are developed.
- The bimaterial legs are connected to longer thermal isolation legs, which thermally isolate the pixel from its substrate, and determine the “detectivity (D*)”

of the detector. Isolation leg design and D* calculation are also detailed in Chapter 4.

- The resultant deflection along the bimaterial leg can be detected in various methods. We adapted an integrated optical readout method based on diffraction grating interferometer, which is superior to the other types of detectors such as capacitive, piezoresistive and other optical methods proposed in the literature. The optical detector and the array readout mechanism is detailed in Chapter 5.
- Various different pixel geometries are analyzed and most promising ones are fabricated at MiRC, Georgia Tech (USA). Microfabrication details are given in Chapter 6.

Chapter 2

LITERATURE REVIEW

2.1 Overview

Detection of optical signal requires interaction of optical signal with the medium called the detector. Due to this interaction, generally reduction of the energy of the optical signal is observed. From a general point of view the reason behind this reduction in energy can be explained by using two physical phenomena which are absorption and scattering. Absorption is defined as the loss in the power in the propagating EM wave which is due to conversion of light energy into other forms of energy such as heat energy because of lattice vibrations, polarization of molecules of the medium, local vibrations of impurity ions and excitation of electrons from the valence band to the conduction band. On the other hand, scattering can be defined as the light diffraction by particles, particularly if the particle diameter is smaller than the wavelength. During the scattering process, light deviates at arbitrarily arranged statistical objects. It is clear from the given definitions that the scattering phenomenon is nothing to do with detection mechanism since the power in the optical signal is not effectively coupled to the lattice of the detector medium.

The energy transfer from the optical signal to the detector medium by way of absorption can be in various forms. Photon detectors and thermal detection are the two main categories for optical detectors. Photon detection process deals with the concept of converting a photon of light into an electron, therefore the excitation of electrons from valence band to conduction band during absorption is the process used by photon detectors. The other type of detector is called thermal detector. Thermal detectors respond to optical signal thermally. That means that their temperature can be modulated by the incident optical radiation. During

the absorption process, because of lattice vibrations occurring in the detector medium, the optical energy is converted into heat energy. The resultant temperature change in the medium produces a corresponding change in another material parameter that can be used for the detection purposes. Figure 2.1 shows different types of infrared detector technologies based on photon detectors, discussed in Sec. 2.2, and thermal detectors, discussed in Sec. 2.3. This thesis focuses on a new type of thermal-detection-based thermo-mechanical detector, which is reviewed in Sec. 2.4.

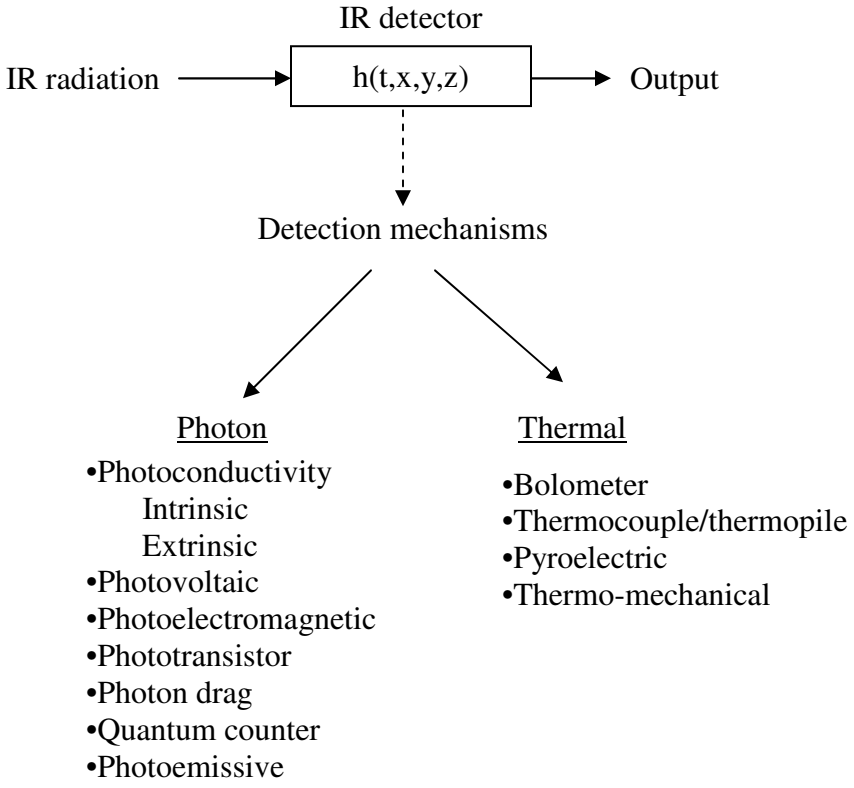

Fig.2.1 Classification of infrared detectors

2.2 Photon Detectors or Cooled IR Detectors

The efficiency of converting a photon of light to an electron is defined to be quantum efficiency (η). Quantum efficiency is a normalized parameter which takes into account reflectance, absorptance, scattering, and electron recombination. This parameter can be used to compare the performances of given infrared detector technologies, and is expressed in percent in this case. Table 2.1 compares the quantum number for the given detector technologies[1].

The electron – hole generation rate as a function of distance into the detector (x) is given as:

$$g(x) = (1-r)E_q ae^{-\alpha x} \tag{2.1}$$

where r is the Fresnel reflectance coefficient of the detector, E_q is the photon irradiance and α is the absorption coefficient of the medium material.

Detector Type	Quantum efficiency (%)
Photoconductor (intrinsic)	60
Photoconductor (extrinsic)	30
Photovoltaic	60
Photoemissive	10
Photographic film	1

Table2.1: Quantum efficiency values for given photon detectors.

Then the magnitude of the current density (A/cm^2) for a generic IR detector with an active layer thickness of l_x can be defined as follows[1]:

$$J = q\int_0^{lx} g(x)dx = (1-r)\cdot q\cdot E_q \cdot \int_0^{lx} ae^{-ax}dx \tag{2.2}$$

$$J = (1-r)\cdot q\cdot E_q \cdot (1-e^{-alx}) \tag{2.3}$$

At this point, quantum efficiency can be given analytically as follows:

$$\eta \equiv \frac{J}{q\cdot E_q} = (1-r)\cdot(1-e^{-alx}) \tag{2.4}$$

The Fresnel reflectance coefficient and l_x terms are the parameters that can be engineered for each detector design. What really determines the performance value for several detector technologies is the absorption coefficient. Therefore for a given family of detectors, this number, which is strongly dependent on the wavelength, should be known.

As wavelength of the optical radiation decreases, the absorption increases. That fact can be explained in terms of band gap of the detector material. The power of the radiation incident on the detector should be sufficient to excite an electron in the valance band to the conduction band. Since the energy of a photon is directly proportional to its frequency through Plank constant, the decrease in wavelength causes more and more electron liberation from the valance band for a unit power of radiation. Therefore, as the wavelength of the radiation decreases for a specific detector technology, the thickness of the detector slab can be made thinner, on the other hand in order to compensate the drop in the absorption coefficient the slab thickness should be thicker for detectors operating at longer wavelengths.

As the bandgap of the detector material decreases, the chance of liberation of electrons in the valance band because of thermal energy. These electrons are not desired for detection

purposes they contribute to dark – current generation. The total number of thermally generated electrons per unit volume can be given as follows:

$$n(E)\Delta E = g(E)f(E)\Delta E \tag{2.5}$$

where n*(E), g(E)* and *f(E)* are the number of electrons per unit volume between energy E and E+ΔE, density of states per unit volume in the energy interval ΔE and the distribution function that an electron is in energy state *E,* respectively. According to Maxwell – Boltzmann, the distribution function can be defined as:

$$f(E) = \frac{1}{A\exp(\varepsilon_g / kT)} \tag{2.6}$$

where *A* is a normalization term which may change with temperature. From Eq.2.6, it is apparent that the total number of thermally generated electrons increases exponentially as temperature increases. Therefore it is required to cryogenically cool the photon detectors to prevent the thermally generated electrons become dominant.

2.3 Thermal Detectors or Uncooled IR Detectors

Although the cooled infrared detectors offer good performance, they have some important drawbacks such as the need for the cryogenic coolers, having high cost, and responding to specific spectral bands. Research on uncooled thermal detectors has been going on to offer a technology to solve these problems so that it will be feasible to use cameras for night vision applications. The microbolometer technology is the most mature one among other uncooled thermal detector technologies like pyroelectric detectors or thermopiles in the sense that they offer both better noise performance and resolution.

Microbolometers are the sensors whose resistance can be modulated by temperature changes as a result of absorption of incident infrared radiation. The sensitive element of the detector can be a thin metal layer or a semiconductor layer. For a metal layer, the resistance of the bolometer increases as the temperature increases[2,3], whereas the resistance decreases if the active layer is made of a semiconductor material[4].

Special materials with high temperature coefficient of resistance (TCR), which is a parameter specifying quantitatively how much resistance change per degree Kelvin change is expected, such as VO_x is used in order to increase the responsivity for microbolometers.

$$TCR = \frac{1}{R_B}\frac{dR_B}{dT} \tag{2.7}$$

where R_B is the bolometer resistance. Together with TCR, responsivity of a microbolometer can be defined as in Eq.2.8[5]:

$$R = \frac{TCR \cdot \beta \cdot \eta \cdot i_b \cdot R_B}{G_e(1+\omega^2 \tau_e{}^2)^{1/2}} \tag{2.8}$$

where β is the fill – factor of the FPA with pixels having an effective thermal conductance G_e including Joule heating effect as a result of heating of detectors due to the bias current. η, i_b, ω and τ_e are the absorption efficiency, bias current, angular frequency of IR radiation and the effective thermal response time, respectively. Using VO_x as the active material Raytheon reported a TCR value of >2.2% / °C with a 25μm pitch size microbolometer[6]. Despite the increasing sensitivity, VO_x is not a standard IC material; therefore it requires expensive fabrication steps. One other disadvantage is the high stress

inherent to that material. For low cost microbolometer, standard CMOS n-well layer is used as the sensing layer[4,7], with a TCR value of 0.34%/ °K that is much smaller than the one obtained with VO_x.

The current trend is to decrease the pixel pitch from 50 μm without degrading the performance of the FPAs. NEC reported a microbolometer with a pitch size of 37 μm[8] that has NETD less than 0.1 K at 60Hz frame rate. NETD (noise equivalent temperature difference) is the figure of merit for an infrared detector which specifies the temperature difference at the target that causes unity SNR. Further decreasing the pitch size to 25 μm without performance degradation is reported by Raytheon[9]. Less than 50mK NETD at 30 Hz is reported by Raytheon. Despite the decrease in the pitch size, the performance is not degraded much. The solution for this is to fabricate the detectors in multi-levels, which allows maintaining the active area space for thermal isolation.

Apart from microbolometers, pyroelectric thermal detectors with high performance have been reported. The temperature difference on the pyroelectric detectors modulates the electric polarization of the active material used. The responsivity of such detectors to steady state temperature difference is zero since the polarization change is neutralized by surface charges. Therefore, a mechanical chopper is usually used to detect the IR radiation. 100 x 100 FPAs with 100 μm pitch size pixels, 87 mK NETD value is reported by Marconi[10] whereas the NETD value goes up to 130mK when the pitch size goes down to 40 μm in a FPA configuration of 384 x 288. Earlier Texas Instruments worked on pyroelectric detectors and they announced a NETD value of 120mK for a FPA with 50 μm pitch size pixels[11].

Another category of widely used thermal detectors is the thermocouples. Thermocouples employ Seebeck effect to map the temperature difference on the target to the voltage signal on the detector. As the temperature on the active layer changes, voltage is simply generated

between two ports of the detector. Such a single detector is called thermocouple, if several of these structures are connected in series to increase the generated voltage; the device is called as thermopile. Responsivity values of 12 and 28 V/W are achieved with detectivity of $1.7 \cdot 10^7 cm\sqrt{Hz}/W$ [12]

2.4 Thermo – Mechanical Thermal Detectors

Thermo – mechanical thermal detector technology is the newest uncooled infrared detection technology that offers high performance. The mechanical structure of the detectors is borrowed from thermostats in the sense that they are composed of bimaterial layers that undergo thermal deformation by inducing temperature difference on them. Further classification among this detector technology is possible according to the detection mechanism used for the thermally induced mechanical deflection. Researchers have studied capacitive[13,14,15,16], piezoresistive[17,18,19] and optical[20,21,22,23,24,25,26,27,28,29] methods to map the temperature of the target to the detection signal.

One method to map the incoming IR radiation into the capacitance change on the detector is to design a parallel plate capacitor, whose top plate is in motion with respect to the bottom one[15]. Top plate is anchored to the substrate through a bimaterial leg in series with thermal isolation leg. In this configuration, top plate both serves as an IR absorber and a movable electrode. One drawback of this configuration is the need to have an electrically conductive path on the thermal isolation legs in order to sense the capacitance change that increases thermal conductivity and decreases sensitivity. Another problem is the uniformity of pixels in large format FPAs. As a result of microfabrication limitations for surface micromachining, the pixels deform initially in an arbitrary fashion which reduces uniformity. In order to increase the responsivity of this type of detectors, parallel plate capacitor architecture with movable bottom electrode[16] is introduced. In this configuration as the temperature of pixels

increases bottom and top electrodes deflect in opposite directions, as a result of which higher capacitance change is possible. One other advantage of such architecture is the design flexibility in the sense that the resonant cavity to boost IR absorption and the parallel plate capacitor gap can be engineered separately.

By coating commercially available piezoresistive microcantilevers with IR absorbing materials, a NEP value of $70nW/\sqrt{Hz}$ is estimated for another microcantilever type thermal detectors[17]. Although that cantilevers are not useful for the formation of large format FPAs, the researchers obtained thermal images by scanning the target area by the sensor cantilever[18].

The first optical readout scheme developed for thermo-mechanical thermal detectors at ORNL was based on optical lever method commonly used in AFM instruments. In this method, laser beam is focused on the tip of a microcantilever and the reflected beam is monitored by a position sensitive photodetector (PSD). The cantilever sensor put in the vacuum cell absorbs the incoming IR radiation and due to its bimaterial structure, it deflects. A quad cell monitors the reflected light from the tip of the cantilever[20].

This method is proved to be a high sensitive measurement technique for single detectors. The readout optics is not integrated with the mechanical structure since the optical elements used are bulky ones. Because of that fact, fine alignment of the optics with the mechanical structure must be done by the user each time. Since the readout scheme is not a compact, interference with the ambient light is a problem. This fact makes it clear that alignment must be precise to get higher sensitivities. It is stated that the bandwidth of the PSDs limits the high speed operation of the readout[22]. Pulsing the readout laser at high frequencies reduces the thermal heating by the readout laser and lowers the power consumption significantly.

There are several limitations that make this readout scheme not feasible for large area FPAs. In order to implement an optical readout method for FPAs, one should offer an integrated solution because of the space limitations. The same laser can be used to illuminate all the pixels at the same time; however one quad cell or bi cell detector is required for each pixel. One cell is composed of four sub – cells each of which is coupled to one separate transimpedance amplifier. Therefore large number of optical elements that are not integrated with the mechanical structure will be needed for the FPAs. The other important issue for this readout is the power consumption. It is reported that 5mW of laser power is required per cantilever[22]. Therefore it is not feasible to offer a low cost solution with this method. Another important drawback of such a high readout laser power incident on the cantilever heats up the cantilever, introducing a large readout noise source and reducing the sensitivity of the system

For the FPA readout, the ORNL group offers a solution by using a CCD rather than one quad cell per cantilever[23]. In this scheme, the pixels in the FPA are illuminated by a readout laser and the reflected beams fall onto a CCD. In terms of sensitivity, using CCD to monitor the reflected light is not as good as quad cell. The reason behind low sensitivity is that the ambient light will interfere with the reflected light, and this will reduce the sensitivity significantly. This problem is solved in quad cell measurement method, since it offers differential measurement opportunity which cancels the interference and refractive index variations in the medium.

Another optical readout method is offered by the researchers at U.C. Berkeley, USA[24]. The first design from that group is based on interdigitated fingers with a pixel size of 130 μm x 100 μm. Again the incoming IR radiation is mapped to the motion on the pixels. Here, some fingers are attached to the movable part of the detector and some stationary ones are left on the substrate. Therefore the interdigitated fingers are in motion. By illuminating the

fingers with a coherent light source, transmitted light can be steered to diffraction orders. The intensities of light at diffraction orders created by interdigitated fingers are measured as the detection signal. It is important that the grating frequency is much larger than the frequency of the cantilever array, to achieve distinct diffraction orders in frequency domain at focal plane of the lens. This principle works for a large pixel that is capable of accommodating sufficiently large number of fingers. As the pixel size becomes smaller (<50um), this method is not practical because of the fabrication limitations. Moreover the fill – factor for that design is low as a result of the need for space for the fingers.

The second design[27], which solves the scalability problem, has a pixel size of 65um x 65um. For this design the laser light scattered from the edge of the pixels forms a diffraction pattern. The intensities of light at the diffraction orders are measured to map the deflection of the cantilevers to the temperature variations. Since the diffraction occurs only at the edges, the orders can not be separated completely and the diffraction efficiency will be poor. That's the weakest point for this readout scheme. The structure is scalable; however the readout signal is not reliable. For both designed structures, readout light escapes through the fingers or edges. Therefore the power of the laser should be higher in order to obtain measurable signal levels at the detectors. Similar to the architecture offered by ORNL, the components given for this architecture are also bulky, since there is not an integrated readout solution for this imager.

Interesting optical readout architectures that completely remove the need of optical detectors to measure the intensity of readout beam are offered by different groups in which the returning beam from the pixels directly steered to the retina of the viewer so that the pattern can be imaged on to the viewer's eye[26,29]. Still they do not provide an integrated readout architecture since bulky readout lasers are needed for these thermal detector arrays.

In this thesis, an integrated optical readout scheme is adapted from the ones used for micromachined ultrasonic transducer arrays, which has a diffraction grating on the back side of the deflecting membrane[30]. The pixel and the readout scheme developed in this research are covered in Ch. 5.

References:

1. E.L. Dereniak, G.D. Boreman, "Infrared Detectors and Systems", John Wiley & Sons
2. Hyung-Kew Lee, Jun-Bo Yoon, Euisik Yoon, Sang-Baek Ju, Yoon-Joong Yong, Wook Lee, and Sang-Gook Kim, "A High Fill-Factor Infrared Bolometer Using Micromachined Multilevel Electrothermal Structures", IEEE TRANSACTIONS ON ELECTRON DEVICES, VOL. 46, NO. 7, JULY 1999
3. R. B. Spielman, C. Deeney, D. L. Fehl, D. L. Hanson, N. R. Keltner, J. S. McGurn, and J. L. McKenney, "Fast resistive bolometry", REVIEW OF SCIENTIFIC INSTRUMENTS VOLUME 70, NUMBER 1 JANUARY 1999
4. D.S. Tezcan, S. Eminoglu, O. S. Akar, and T. Akin, "A low cost uncooled microbolometer focal plane array using the CMOS n – well layer", 2001 IEEE 0-7803-5998-4
5. P. W. Kruse, "Uncooled Thermal Imaging, Arrays, Systems, and Applications", Tutorial Texts in Optical Engineering Vol. TT51, 2001
6. D. Murphy, M. Ray, R. Wyles, J. Asbrock, N. Lum, A. Kennedy, J. Wyles, C. Hewitt, G. Graham, and T. Horikiri, J. Anderson, D. Bradley, R. Chin, and T. Kostrzewa, "HIGH SENSITIVITY (25 μmPITCH) MICROBOLOMETER FPAs", Proceedings of SPIE Vol. 4454 (2001)
7. D. S. Tezcan, S. Eminoglu, Member,T. Akin "A Low-Cost Uncooled Infrared Microbolomete Detector in Standard CMOS Technology", IEEE TRANSACTIONS ON ELECTRON DEVICES, VOL. 50, NO. 2, FEBRUARY 2003
8. N. Oda, Y. Tanaka, T. Sasaki, A. Ajisawa, A. Kawahara, S. Kurashina, "Performance of 320x240 Bolometer – Type Uncooled Infrared Detector", NEC Res. & Develop. Vol. 44, No. 2, April 2003
9. D. Murphy, M. Ray, J. Wyles, J. Asbrock, C. Hewitt, R. Wyles, E. Gordon, T. Sessler, A. Kennedy, S. Baur, D. Van Lue, S. Anderson, R. Chin, H. Gonzalez, C. Le

Pere, S.Ton, and T. Kostrzewa, “PERFORMANCE IMPROVEMENTS FOR VOx MICROBOLOMETER FPAs”, Proc. of SPIE Vol. 5406, 2004

10. R. K. McEwen, P. A. Manning, “EUROPEAN UNCOOLED THERMAL IMAGING SENSORS”, SPIE Vol. 3698, April 1999
11. C. Hanson, H. Beratan, “Uncooled Pyroelectric Thermal Imaging”, 0-7803, 1847, IEEE, 1995
12. R. Lenggenhager, H. Baltes, J. Peer, M. Forster, ”Thermoelectric Infrared Sensors by CMOS Technology”, IEEE Electron Devices Letters, Vol.13, No.9, September 1992
13. R. Amantea, C. M. Knoedler, et.al., "An Uncooled IR imager with 5mK NETD" Proceedings of SPIE, 3061, 210-222 1997
14. R. Amantea, L. A. Goodman, F. P. Pantuso, et.al., "Progress Towards an Uncooled IR Imager with 5mK NETD", Proceedings of SPIE, 3436(2), 647-659 1998
15. S. R. Hunter, R. Amantea, L. A. Goodman, et.al., “High Sensitivity Uncooled Microcantilever Infrared Imaging Arrays”, Proceedings of SPIE Vol. 5074, 2003
16. B. Li, “Design and simulation of an uncooled double-cantilever microbolometer with the potential for ~mK NETD”, Sensors and Actuators A 112 (2004) 351–359
17. P. G. Datskos, P. I. Oden, T. G. Thundat, E. A. Wachter, R. J. Warmack, and S. R. Hunter, "Remote Infrared Radiation Detection Using Piezoresistive Microcantilevers," Appl. Phys. Lett. 69, 2986 (1996)
18. P.I. Oden, P.G. Datskos, T. Thundat, and R.J. Warmack, "Uncooled Thermal Imaging Using a Piezoresistive Microcantilever," Appl. Phys. Lett. 69, 3277 (1996)
19. S. Rajic, B.M. Evans III, P.G. Datskos, P.I. Oden, T. Thundat, and C.M. Egert, "Piezoresistive Microcantilever Optimization for Uncooled Infrared Detection Technology," Infrared Spaceborne Remote Sensing IV, SPIE, 2817, 179 (1996)
20. E. A. Wachter, T. G. Thundat, P. G. Datskos, P. I. Oden, S. L. Sharp, and R. J. Warmack, "Remote Optical Detection Using Microcantilevers," Rev. Sci. Instr. 67, 3434 (1996)

21. J.L. Corbeil, N.V. Lavrik, S. Rajic, and P.G. Datskos, "Self-Leveling Uncooled Microcantilever Thermal Detector," Applied Physics Letters, 81, 1306 (2002)
22. L.R. Senesac, J.L. Corbeil, S. Rajic, and P.G. Datskos, "IR imaging using uncooled microcantilever detectors", Ultramicroscopy 97, 451-458 (2003)
23. P.G. Datskos, S. Rajic, L.R. Senesac, D.D. Earl, B.M. Evans, J.L. Corbeil, and I. Datskou, "Optical Readout of Uncooled Thermal Detectors," Infrared Technology and Applications XXVI, SPIE, 4130, 185 (2000)
24. T. Perazzo, M. Mao, O. Kwon, A. Majumdar, J. Varesi, and P. Norton, "Infrared vision using micro-optomechanical camera," *Applied Physics Letters,* Vol. 74, pp. 3567-3569 (1999)
25. Y. Zhao, M. Mao, A. Majumdar, "Application of Fourier Optics for Detecting Deflections of Infrared-Sensing Cantilever Arrays," *Microscale Thermophysical Engineering*, Vol. 3, pp245-251 (1999)
26. M. Mao, T. Perazzo, O. Kwon, A. Majumdar, J. Varesi, P. Norton, ”Direct-View Uncooled Micro-Optomechanical Infrared Camera”, 0-7803-5109, IEEE, 1999
27. Y. Zhao, M. Mao, R. Horowitz, A. Majumdar, J. Varesi, P. Norton, J. Kitching, "Optomechanical Uncooled Infrared Imaging System: Design, Microfabrication, and Performance," JOURNAL OF MICROELECTROMECHANICAL SYSTEMS, VOL. 11, NO. 2, APRIL 2002
28. J. Zhao, “High Sensitivity Photomechanical MW-LWIR Imaging using an Uncooled MEMS Microcantilever Array and Optical Readout”, Proc. of SPIE Vol. 5783, 2005
29. Tohru Ishizuya, Junji Suzuki, Keiichi Akagawa, Tsuneyuki Kazama, “Optically Readable Bi-material Infrared Detector”, Proceedings of SPIE Vol. 4369 (2001)
30. W. Lee, N. A. Hall, Z. Zhou, F. L. Degertekin, “Fabrication and Characterization of a Micromachined Acoustic Sensor With Integrated Optical Readout”, IEEE Journal of Selected Topics in Quantum Electronics, Vol. 10, No. 3, May/June 2004

Chapter 3

INFRARED ABSORBER

3.1 Introduction

The transmittance of atmosphere as a function of radiation wavelength is given in Ref.1. Transmittance is over 80% from 3-5 μm in the middle infrared (MWIR) band and it is over 70% in the 8-14 μm long-wave infrared (LWIR) band. Because of such a high transmittance in these bands, they serve as a window for IR applications. Specific IR detector and imaging technologies have been developed for these transmission bands. In this chapter, starting with blackbody radiation physics, the infrared absorber design for both MWIR and LWIR bands are detailed. The absorption formulas for 2-layer media with resonant cavity are developed. One of the important contributions of this chapter is the proposal for use of thin-film metals as IR absorber in microcantilever IR detectors. Thin film absorbers, when combined with resonant cavities, give high absorption and low thermal mass, which are critical performance parameters for IR detectors.

3.2 Blackbody Radiation

The first energy conversion takes place in IR detector is the transfer of the radiation energy inherent to the target into heat energy on the detector. In order to express the radiation energy quantitatively, the term radiance (L) is defined. Radiance is the amount of power radiated per unit area of the target per unit solid angle. The explicit spatial dependence of radiance is implicit for the term photon exitance (M_p), which is the number of photons emitted by unit area of a blackbody target in a unit time[2] as given in Eq.3.1. For a

Lambertian source, which has an intensity directly proportional to the cosine of the angle from which it is viewed, $L = M_p/\pi$.

$$M_p = \frac{1}{2} N\bar{v} = \frac{cN}{4} \tag{3.1}$$

where N is the number of photons emitted per unit cavity volume of the blackbody target, $\bar{v}$ is the average velocity of the photons and c is the speed of light. N can be found by integrating the product of density of states *(DOS)* per unit cavity volume that is $1/4\pi^3$ and the expected number of photons ($\bar{n}$) in any state with an energy of $E = h\nu$, over all β space. For a spherical coordinate system:

$$N = \int DOS \cdot \bar{n} \cdot d\beta = \int \frac{1}{4\pi^3} \frac{1}{\exp(h\nu/kT) - 1} 4\pi\beta^2 d\beta \tag{3.2}$$

Where *h, k,* ν and *T* are the Planck's constant, Boltzmann's constant, optical frequency and the temperature of the blackbody, respectively. N can be interpreted in terms of wavelength as given in Eq.3.3, since $\beta = 2\pi/\lambda$.

$$N = \int \frac{8\pi}{\lambda^4} \frac{1}{\exp(h\nu/kT) - 1} d\lambda \tag{3.3}$$

Combining Eq.3.1 and Eq.3.3, power radiated by unit area of a blackbody target in a unit time in a spectral width of $d\lambda$ can be interpreted as in Eq.3.4 since the energy associated per photon is hc/λ. For T = 300 °K, radiated power is plotted as a function of wavelength in Fig.3.1.

$$P(\lambda,T)d\lambda = \frac{2\pi hc^2}{\lambda^5}\frac{1}{\exp(hc/\lambda kT)-1}d\lambda \tag{3.4}$$

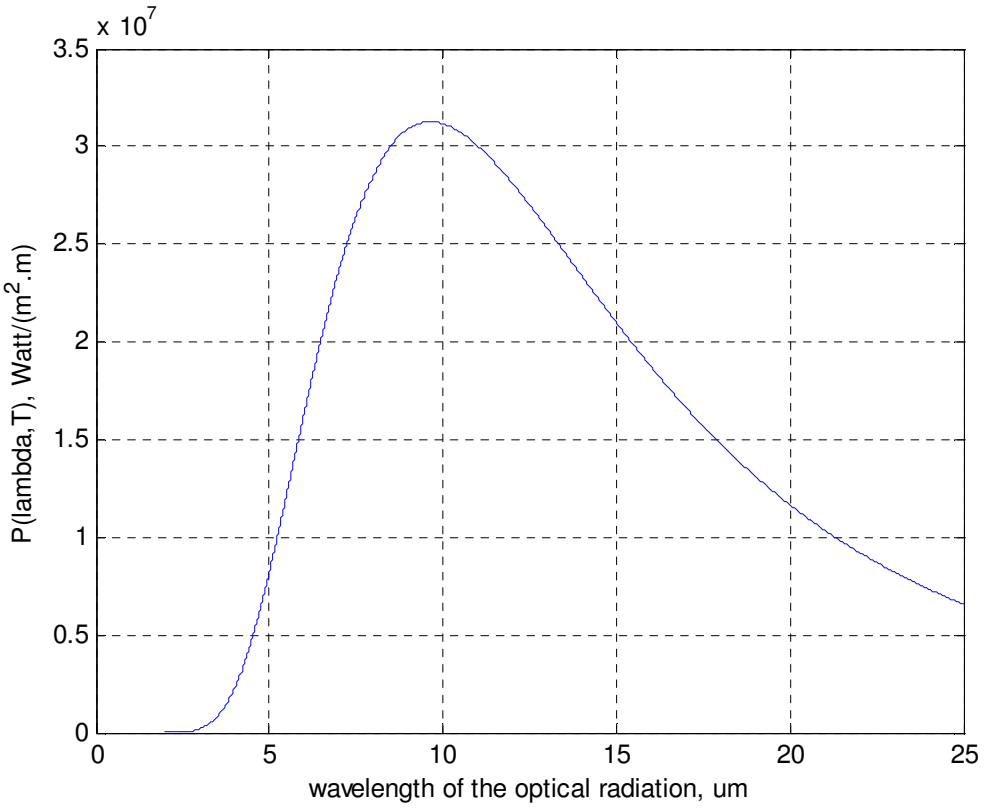

Fig.3.1 Power radiated by unit area of a blackbody target in a spectral width of dλ

Eq.3.4 is very important to quantify the radiation power. The total area under the curve given in Fig.3.1 gives the total exitance from a blackbody at temperature T. This relationship is called Stefan – Boltzmann law.

Historically the noise performance of infrared detectors is given in terms of temperature. Therefore, it is important to figure out the rate of change in power per unit area radiated by a blackbody at a temperature at T, with respect to T measured within the wavelengths of λ_1 – λ_2[3]. This parameter can be calculated numerically as follows:

$$(\Delta P/\Delta T)_{\lambda 1-\lambda 2} = \int_{\lambda 1}^{\lambda 2} \frac{1495}{\lambda^6 \cdot \sinh^2(\frac{24}{\lambda})} d\lambda \tag{3.5}$$

For the LWIR and MWIR bands, the $(\Delta P/\Delta T)_{\lambda 1-\lambda 2}$ is given by 2.6285 W/m^2 and 0.2120 W/m^2, respectively. Thus there is about 13x more radiation energy in the LWIR compared to MWIR.

3.3 Design of IR Absorber

The absorption of the radiation from the target by the thermal detector should be maximized in order to increase the responsivity, thus sensitivity. Simplest model for absorption is given in Ref.4 in which the amplitude of the light inside an active layer with a thickness of *d* is attenuated by a factor of $\exp(-\frac{2\pi kd}{\lambda})$ where k is the imaginary part of the refractive index of the medium. It is assumed that the power is not lost at the boundaries of the active layer. The real and imaginary parts of the refractive index of LPCVD Silicon Nitride, which is commonly used as an infrared absorber material in LWIR band, are given[4] for the wavelength of 2 – 16 μm. From that data the expected absorption can be plotted as a function of wavelength for a nitride thickness of 500 nm.

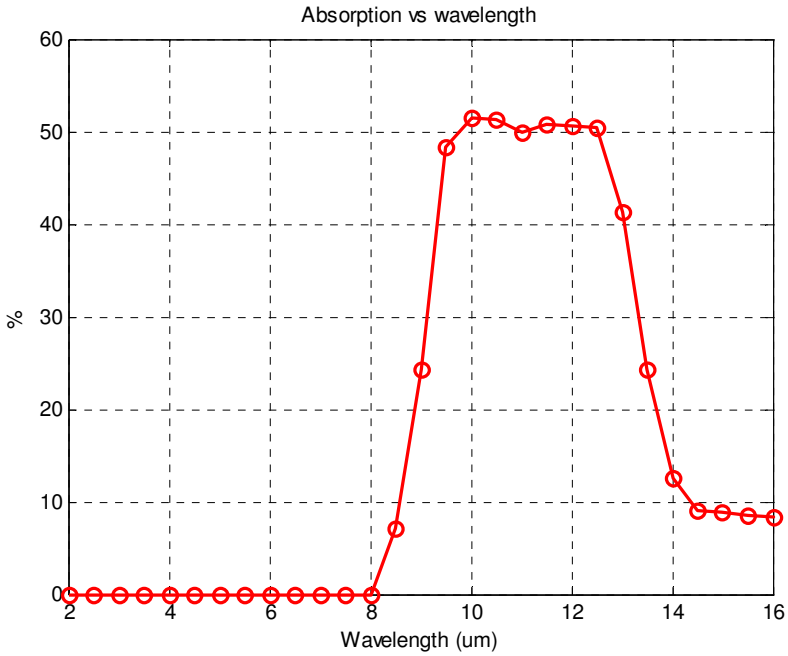

Fig.3.2 Simplest estimation of absorption for a 500 nm thick nitride layer based on data given in Ref.4

Since the building blocks of microstructures are thin layers with the current microfabrication technology; the absorption process should be studied with a thin active layer as generalized in Fig.3.2. For a complete analysis the Fresnel coefficients at the boundaries and their effects on the power transfer should be modeled. For this analysis, the incoming radiation, which is incident on the intersection of the boundary of the regions with refractive indices n_0 and n_1, is assumed to have unity intensity. Normal incidence is assumed for the following analysis for the sake of simplicity for calculation of absorptance when the active slab is composed of multi – layers.

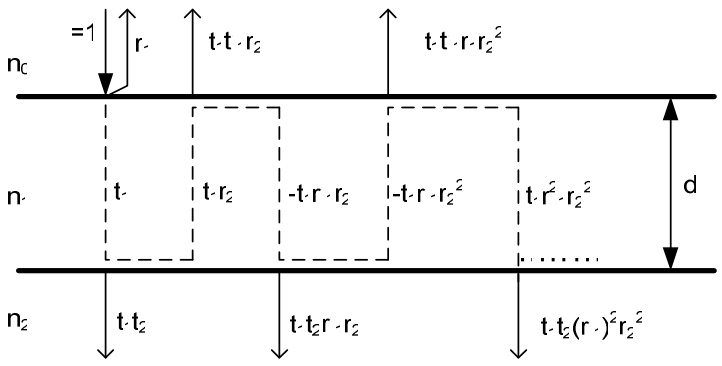

Fig.3.3 Active layer with infinite extent which absorbs incoming light with unity intensity

The Fresnel coefficients for the reflectivities (r_i's) and the transmittivities (t_i's) given in Fig.3.2 are given as follows:

$$r_i = \frac{n_{i-1} - n_i}{n_{i-1} + n_i} \quad ; \qquad r_i' = \frac{n_i - n_{i-1}}{n_i + n_{i-1}} \tag{3.6}$$

$$t_i = \frac{2n_{i-1}}{n_{i-1} + n_i} \quad ; \qquad t_i' = \frac{2n_i}{n_{i-1} + n_i} \tag{3.7}$$

where r_i is the reflectivity coefficient for light incident from the boundary from the media with the refractive index n_{i-1} to the one with the refractive index n_i; whereas r_i' is the reflectivity in the reverse direction. Here the refractive indices n_0, n_1 and n_2 are complex parameters for the sake of generality, $n = \bar{n} - i \cdot \bar{k}$. The amplitudes of the beams reflected and transmitted successively are given clearly in Fig.3.2. The total amplitude of the reflected beam (r) from the first boundary and the transmitted beam (t) into the third media are given as follows:

$$r = r_1 + t_1 t_1' r_2 \exp(-2i\Delta) - t_1 t_1' r_1 r_2^{\,2} \exp(-4i\Delta) + \ldots \tag{3.8}$$

$$t = t_1 t_2 \exp(-i\Delta) - t_1 t_2 r_1 r_2 \exp(-3i\Delta) + t_1 t_2 r_1^{\,2} r_2^{\,2} \exp(-5i\Delta) - \ldots \tag{3.9}$$

where $\Delta = \frac{2\pi}{\lambda} n_1 d$ is the phase accumulated in the media with the refractive index n_1 for each traversing of beam through the layer with thickness d.

The infinite sum given in Eq.3.8 can be rewritten as in Eq.3.10

$$r = r_1 + ax + ax^2 + ax^3 + \ldots$$
$$a = t_1 t_1' r_2 \exp(-i\Delta); \qquad x = -r_1 r_2 \exp(-i\Delta) \tag{3.10}$$

Therefore, the resultant reflectivity amplitude and the corresponding intensity of the beam ($R = n_0 rr^*$) can be given explicitly as follows:

$$r = r_1 + \frac{a}{1-x} = r_1 + \frac{t_1 t_1' r_2 \exp(-2i\Delta)}{1 + r_1 r_2 \exp(-2i\Delta)} \tag{3.11.a}$$

$$R = n_0 \frac{r_1^{\,2} + r_1^{\,4} r_2^{\,2} + t_1^{\,2} t_1'^{\,2} r_2^{\,2} + 2 t_1 t_1' r_1^{\,2} r_2^{\,2} + 2 r_1 r_2 (r_1^{\,2} + t_1 t_1') \cos(2\Delta)}{1 + r_1^{\,2} r_2^{\,2} + 2 r_1 r_2 \cos(2\Delta)} \tag{3.11.b}$$

The infinite sum given in Eq.3.9 can be rewritten as in Eq.3.12

$$t = b + by + by^2 + by^3 + \ldots$$
$$a = t_1 t_2 \exp(-i\Delta); \qquad y = -r_1 r_2 \exp(-2i\Delta) \tag{3.12}$$

Eq.3.12 can be used to give the amplitude of the transmittivity and the intensity of the light ($T = n_2 tt^*$) that pass through the layer with a refractive index n_1 explicitly:

$$t = \frac{b}{1-y} = \frac{t_1 t_1' \exp(-i\Delta)}{1 + r_1 r_2 \exp(-2i\Delta)} \tag{3.13.a}$$

$$T = n_2 \frac{t_1^{\,2} t_2^{\,2}}{1 + r_1^{\,2} r_2^{\,2} + 2 r_1 r_2 \cos(2\Delta)} \tag{3.13.b}$$

By the conservation of energy the absorption can be given as A = 1 – R – T; since light generation cannot be possible in any of the media. The resultant reflectance, transmittance, and absorptance is plotted in Fig.3.4. The effective absorptance is below 40% for the interested infrared band 8 – 14 μm. Therefore to use the thin dielectric slab itself as an IR absorber is not the best choice. **The absorption can also change with the angle of incidence but the effect is ignored in this analysis.**

It is well known that the optical absorption can effectively be enhanced for a specific wavelength by implementing an appropriate resonant cavity. The idea behind the resonant cavity enhancement of absorption is to trap the radiation in a transparent cavity with an optical thickness of λ/4 on top of a good reflector. The enhancement is theoretically shown in Ref.3.5 and 3.6 for a structure composed of a thin absorber layer placed in between reflectors that serve as an optical cavity.

For the sake of generality, the absorption is studied for a multilayer structure as given in Fig.3.5.a where n_j is the refractive index ($n_j = \bar{n}_j - i \cdot \bar{k}_j$, j = 0,1…m) and r_j is the reflectivity amplitude of layer j with a thickness of d_j.

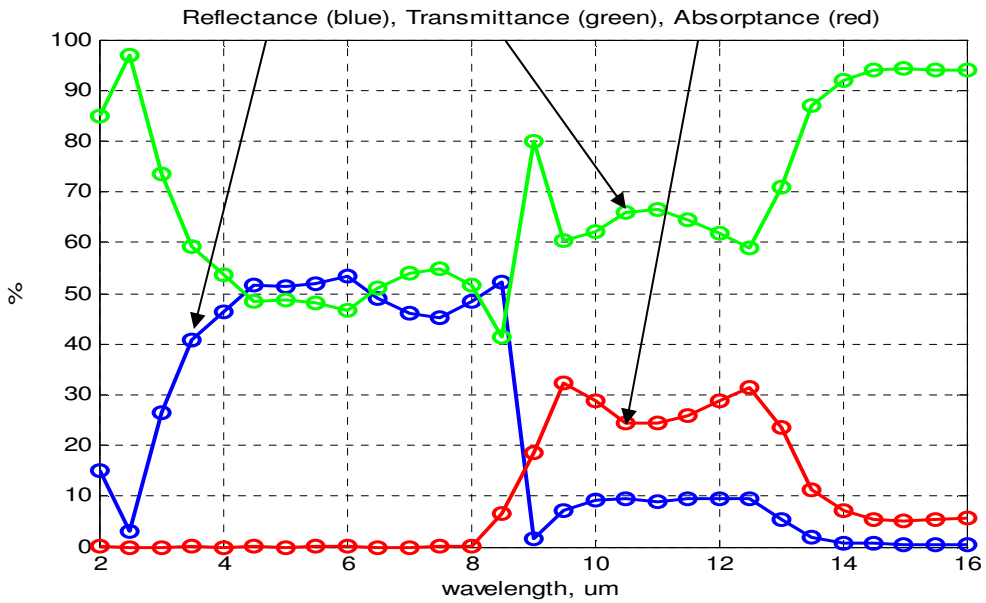

Fig.3.4 Spectral response of a 500 nm thick SiN_x layer

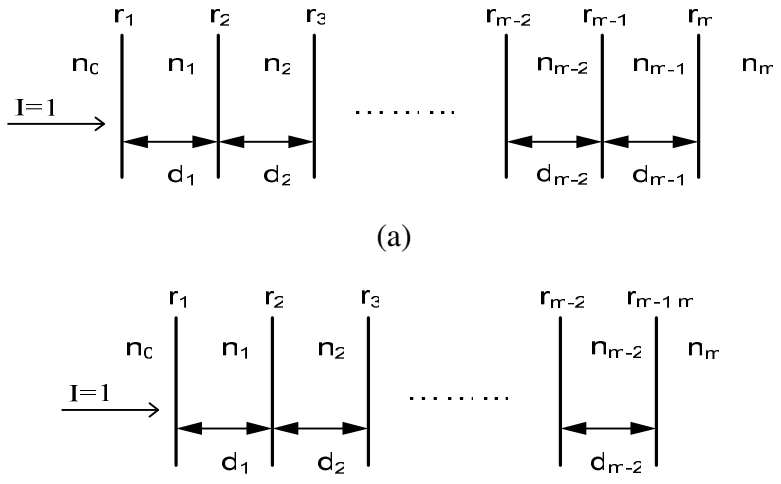

(a)

(b)

Fig.3.5 (a) Schematics for multilayer infrared absorber (b) Equivalent structure after 1 level elimination

The effective amplitude reflectivity for the radiation incident on the boundary between layers m-2 and m-1 can be found by modifying Eq.3.11.a as follows:

$$r_{m-1,m} = r_{m-1} + \frac{t_{m-1}t_{m-1}'r_m \exp(-2i\Delta_{m-1})}{1 + r_{m-1}r_m \exp(-2i\Delta_{m-1})} \tag{3.14}$$

where $\Delta_{m-1} = \frac{2\pi}{\lambda} n_{m-1}d_{m-1}$ is the phase accumulated in the layer with the thickness of m-1 together with the amplitude reflectivity and transmittivity defined in Eq.3.6 and Eq.3.7. Recursively, the layers in the multilayer structure may be eliminated starting from the last layers. After 1-level elimination, the equivalent structure is given in Fig.3.5.b. The second step is to eliminate the layer with the thickness of d_{m-2} by finding the amplitude reflectivity "$r_{m-2,m-1,m}$". Following that pattern overall reflectivity "$r_{1,2,3\ldots,m-2,m-1,m}$" can be calculated. The explicit expression for the overall reflectivity and transmittivity is lengthy even for 3 layers and closed-form formulas are not given in here. The calculations for n-layer media absorption are carried out using MATLAB.

The multilayer infrared absorber solution is used to model the enhancement of absorption of optical radiation for a hypothetical absorber with a resonant cavity as given in Fig.3.6

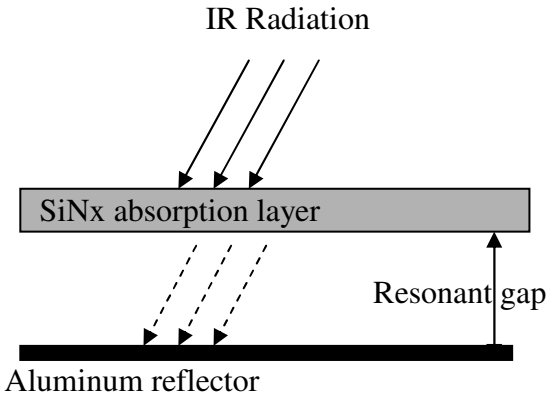

Fig.3.6 Hypothetical infrared absorber with a resonant cavity

By changing the gap between the absorption layer and the reflector of the cavity, the wavelength at which the absorption is maximized can be engineered. For this design the resonant cavity is designed such that the absorption at the wavelength of 10 μm is maximized since that is the point at which a blackbody at room temperature (300 °K) has its spectral exitance peak as given in Fig.3.1.

The plot given in Fig.3.7 shows the dependency of absorptance to the wavelength of the radiation for an active layer of 0.5 μm thick SiN_x. Theoretically it is expected to have the peak point at a gap of quarter of the wavelength. Since the bottom reflector layer made of Aluminum is not a perfect reflector, the absorptance peak point shifts as seen from Fig 3.7.

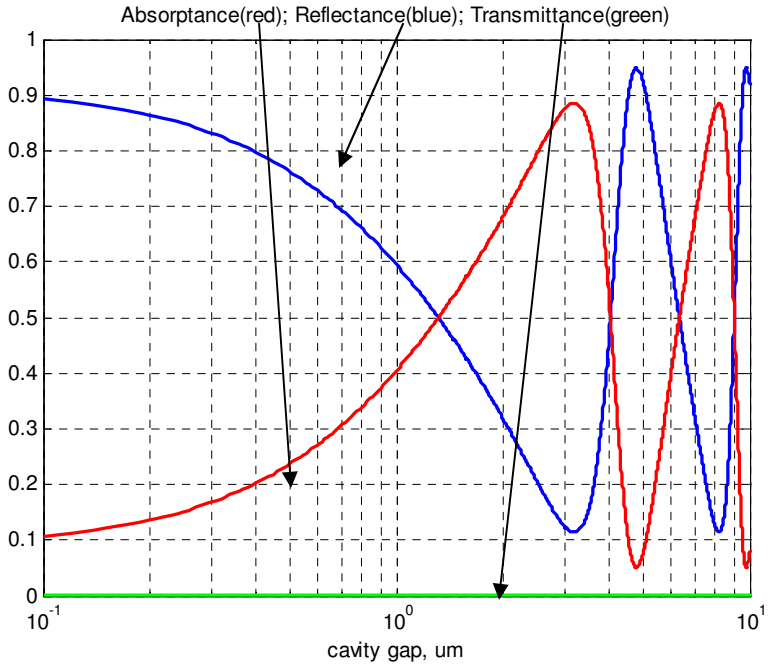

Fig.3.7 Absorption at 10 μm wavelength as a function of resonant cavity gap.

The absorption is at maximum when the gap of the resonant cavity is around 2.5 μm independent of the active layer thickness. Therefore it is possible to further optimize the IR absorber to maximize the absorption at the wavelength of 10 μm, center of the LWIR band, by varying the thickness of the nitride layer. Calculations show that the peak absorptance level is achieved when the active layer is 770 nm thick. The analytical model for multilayer absorber predicts absorption, transmission and reflectance considering the penetration depth into account, which is given as:

$$d_{penetration} = \frac{\lambda}{4\pi \cdot k} \tag{3.15}$$

k is around unity for the band of 8 – 12 μm[4], which makes the penetration depth approximately 0.8 μm. This fact can also be seen from Fig.3.8 where absorptance is plotted

as a function of active layer thickness. When the active layer is thicker than the penetration depth, absorptance degrades since the resonant cavity is not functional anymore.

Considering the above analytical results and the microfabrication constraints, a good design choice for the infrared absorber is a 0.5 μm thick silicon nitride together with a 2.5μm resonant cavity, which corresponds to λ/4 at 10μm, where a blackbody at room temperature (300 °K) has its spectral exitance peak. The infrared absorber pads are labeled on the schematic of the designed detector as given in Fig.3.9.

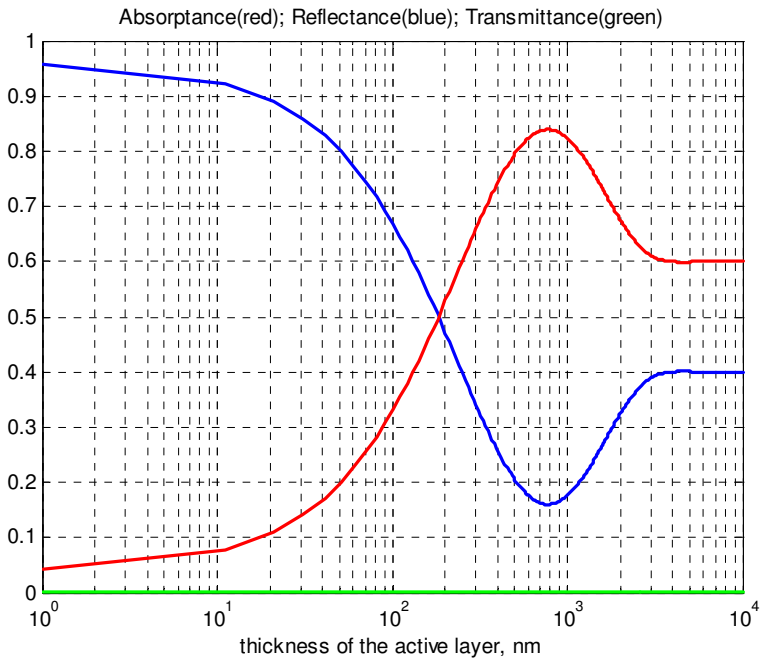

Fig.3.8 Variation of absorptance using 2.5 μm resonant cavity as a function of nitride layer thickness. Design point is chosen as 0.5μm.

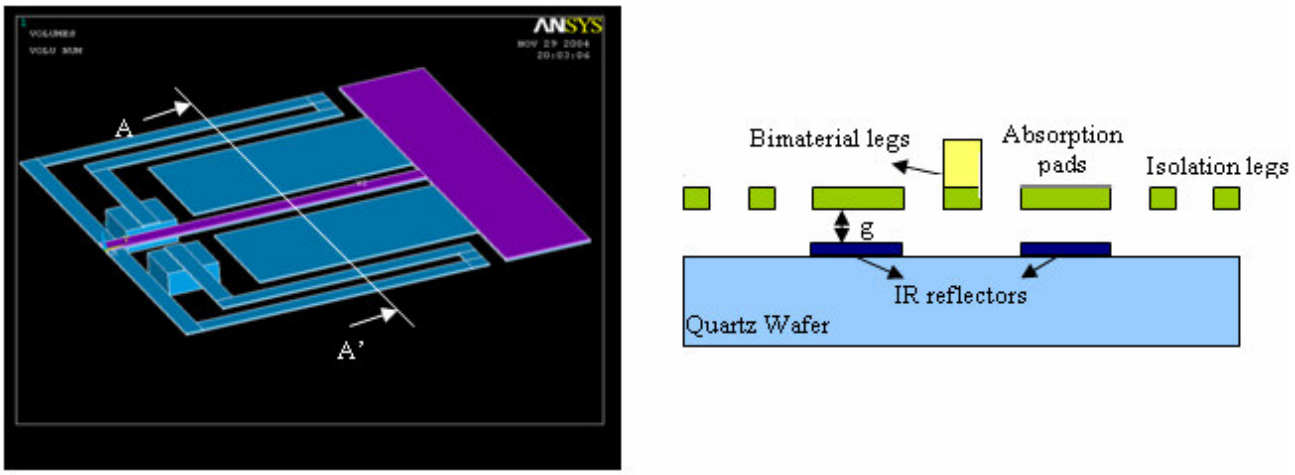

(a) (b)

Fig.3.9 (a) One pixel of FPA; (b) Cross section of the detector pixels

3.4 IR Absorber Alternatives

One method to increase IR absorption is to use optically black materials among which black – gold and black – platinum offer high absorptance. The blackness of the absorber layer is due to the porous microstructure and the dendrites formed on the surface of the layer. It is possible to reach an absorptance level of >90% in the far infrared band with black platinum absorber[7]. Due to the porosity of the structure, the absorber behaves as if there are many small cavities in which absorption process takes place. That is the main reason for the enhancement of the absorption.

Generally the black – metal absorbers are deposited by the method of evaporation at higher vacuum environment[8]. For the black – gold preparation, a two-step fabrication is described in Ref.4.6. First, a droplet of gold is evaporated at low vacuum environment in order to ensure the adhesion of gold layer to the substrate. Secondly, the vacuum chamber is

rinsed by the gas for 20 min in order to increase the pressure and ensure the porosity of the deposited layer. Then second droplet of gold is evaporated. The resultant layer is usually very thick (>20 μm). Therefore the heat capacity of a thermal detector employing black – metal layer as an IR absorber becomes large, so does the thermal time constant, which prevents to have a fast detector. Moreover such a thick and porous layer is not easy to pattern, which is a must to realize a large format pixilated imager.

Metals are good absorbers in a wide optical spectrum; however they emit most of the radiation they absorb. It was studied to make the surface of silver be very rough in order to prevent it be reflective. By using a rough silver layer with a thickness of 5 to 7 μm, it was shown that near 100% absorption is possible[9]. Since the required surface roughness cannot be guaranteed among an array of small pixels, that method is not very compatible with the current microfabrication technology. Also, the layers need to be sufficiently thick to ensure the required surface roughness, thus not suitable for small pixilated detector arrays.

3.4.1 Thin Film Metal Absorber

Finally a thin layer of metal is studied as an infrared absorber. It is experimentally shown that a thin layer of gold is capable of effectively absorbing infrared radiation[10]. The researches measured that the absorptance for ~17 nm thick Au layer is ~50%. This phenomenon is observable when the thickness of the metal layer is much smaller compared to the wavelength of optical radiation. When that condition holds, the layer becomes partly transparent. The reason for that can be explained by considering the granularity in the structure of the layer. Due to the granular structure the conductivity of the metal layer decreases. The decrease for Aluminum layer is as much as 500 times[11]. For such a large difference from bulk material properties, thin layer of Aluminum behaves as if it is a semiconductor. That's why it can be used as an infrared absorber. The dependence of the refractive index to the conductivity is given as follows[11]:

$$nk = \frac{\sigma_R}{2\varepsilon_0 \omega} \tag{3.16}$$

$$n^2 - k^2 = \varepsilon'_\infty - \frac{\sigma_I}{\varepsilon_0 \omega} \tag{3.17}$$

where σ_R and σ_I are the real and imaginary parts of the complex conductivity at the optical angular frequency ω. The expressions given above may further be simplified as in Eq.3.18 if λ<13 μm.

$$n \approx k \cong \sqrt{\frac{\sigma_0}{2\varepsilon_0 \omega}} \tag{3.18}$$

where $\sigma_0 = 1\text{x}10^5\ \Omega^{-1}\text{m}^{-1}$ is the DC conductivity for the thin Al layer, which is almost 500 times smaller than that of bulk material property. The resulting real and imaginary parts of the complex refractive index of thin Al layer are plotted in Fig.3.10 as a function of wavelength.

Once the metal's refractive index components are known, the expected absorptance as a function of layer thickness can be calculated by using the above analytical model. The absorption results for Aluminum are given in Fig.3.11. In conclusion, 50% absorption can be obtained at 10μm wavelength using a 50nm thin Al film.

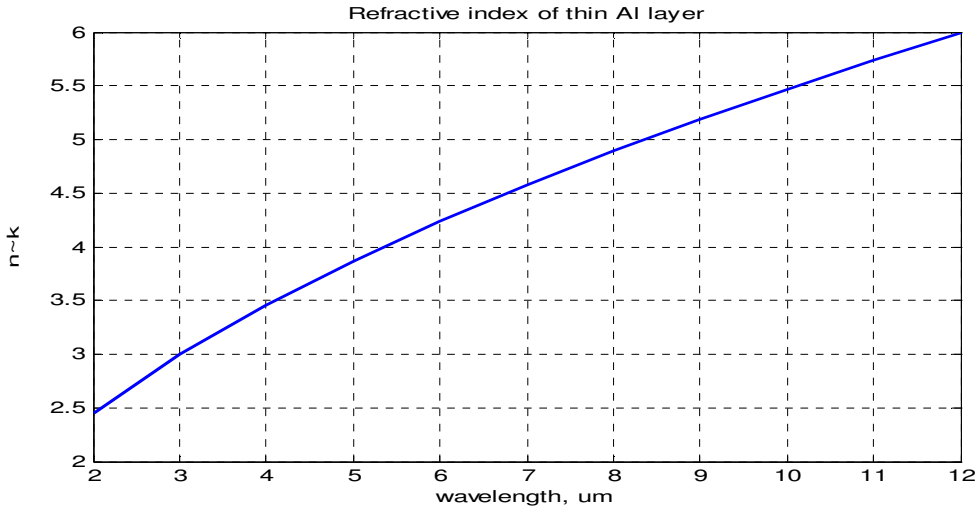

Fig.3.10 Real and imaginary parts of the complex refractive index of thin Al layer as a function of wavelength

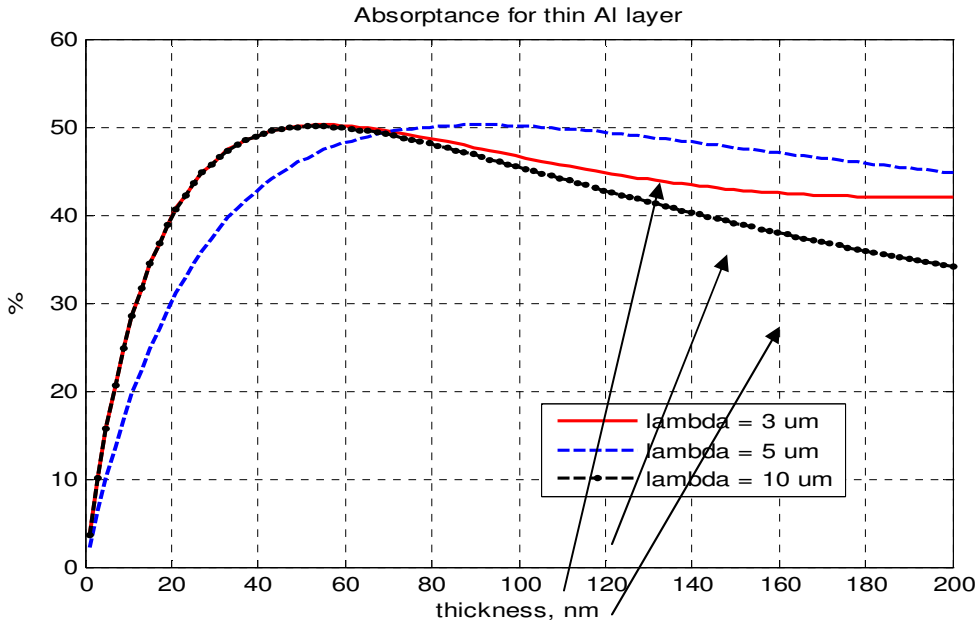

Fig.3.11 The expected absorptance by thin Al layer as a function of thickness for important IR wavelengths

The absorption can be further improved by implementing a resonant cavity under the metal absorber as discussed earlier. As seen in Figure 3.12, in theory, 100% absorption is possible at 10μm wavelength using approximately 20nm Al layer in combination with a 2.5μm thick resonant cavity.

Thin metal absorbers are important not only because they offer high theoretical absorption, but only due to the fact that they decrease the heat capacity of the detector, which means faster response time is possible. Testing of the thin-film IR absorber concept developed here is left as a future work.

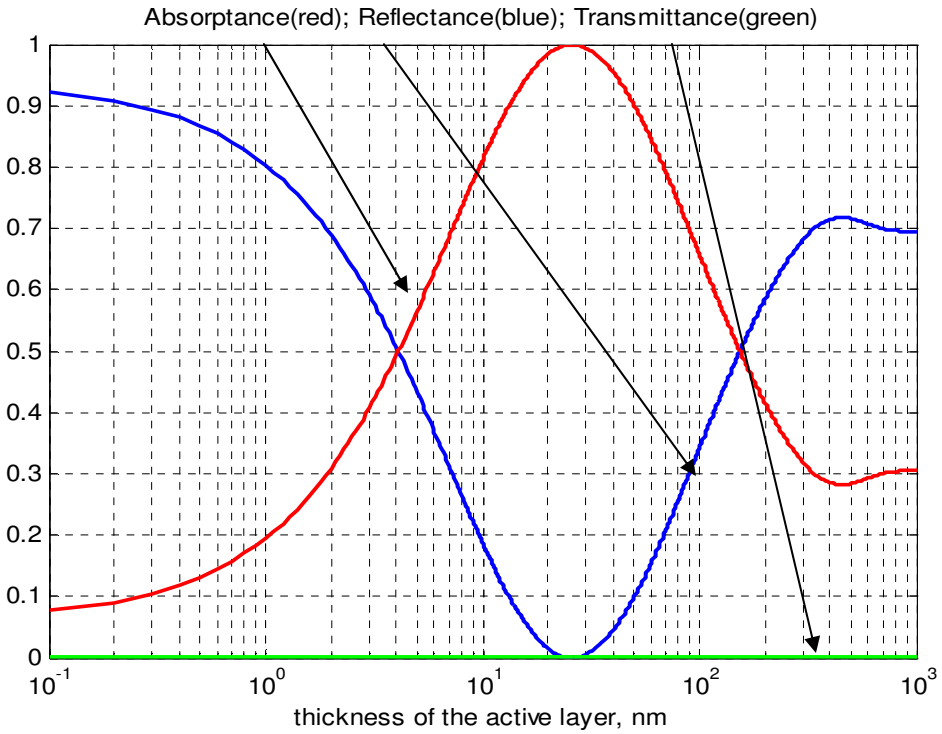

Fig.3.12 Theoretical enhancement of absorption for a thin Al layer by resonant cavity at the wavelength of 10 μm

References

1. R. Hudson, “Infrared System Engineering”, John Wiley and Sons, Inc., 1969
2. E.L. Dereniak, G.D. Boreman, “Infrared Detectors and Systems”, p.64, John Wiley and Sons, Inc., 1996
3. P.W. Kruse, “Can the 300K radiating background noise limit be attained by uncooled thermal imagers?”, Proc. of SPIE Vol.5406, p.437-p.447, 2004
4. Yang Zhao, “Optomechanical Uncooled Infrared Imaging System”, Dissertation for the Degree of Doctor of Philosophy, University of California, Berkeley, Fall 2002.
5. M. S. Unlu, S. Strite, “Resonant cavity enhanced photonic devices”, J. Appl. Phys. 78 (2), 15 July 1995
6. M. S. Unlu, K. Kishino, H. J. Liaw, H. Morkoc, “A theoretical study of resonant cavity – enhanced photodetectors with Ge and Si active regions”, J. Appl. Phys. 71 (8), 15 April 1992
7. P. Muralt, “Micromachined Infrared Detectors Based on Pyroelectric Thin Films”, Rep. Prog. Phys. 64 (2001) 1339–1388
8. W. Becker, R. Fettig, W. Ruppel, “Optical and electrical properties of black gold layers in the far infrared”, Infrared Physics & Technology ,40, 1999, p.431–p.445
9. N. Neff, “Optical properties of ultrarough silver films on silicon”, J. Appl. Phys. 80 (2), 15 July 1996
10. W. Lang, K. Kuhl, H. Sandmaier, “Absorbing layers for thermal infrared detectors”, Solid-State Sensors and Actuators, 1991. Digest of Technical Papers, Transducers ‘91 Digest, p.635-p.638
11. A. Hadni, X. Gerbaux, “Infrared and millimeter wave absorber structures for thermal detectors”, Infrared Phys. Vol.30, No.6, p.465-p.478, 1990

Chapter 4

MECHANICAL DESIGN OF THE DETECTOR

4.1 Introduction

This chapter gives the details of the mechanical structure designed for the thermal detector pixels. The detector converts thermal energy into mechanical displacement. In section 4.2 analytical formulations are given for a general multi – layered thin film structures. The analytical model is then compared with finite element method (FEM) simulations by using Ansys™. In section 4.3, the analytical and numerical results are validated with a test structure and the experimental results agree well.

Noise analysis, which gives a measure of the performance of the detector, is given together with the thermal model of the detector. In section 4.4, fundamental noise sources are discussed and formularized. In section 4.5, a thermal model of the detector is developed and detector noise and response time is computed using the mechanical model developed in this chapter. It is shown that the detector arrays are suitable to be operated as imaging systems.

4.2 Analytical Modeling and Verification of the Model

4.2.1 Thermal Deflection for n – layer Structures

Many micromachined structures are formed by adding layers of materials on top and bottom of a substrate wafer. Coefficients of thermal expansion (CTE) mismatch between those layers can produce large stress and strains and deform the structure. Thermal deformation can have a significant effect in the device performance, particularly in optical MEMS applications where optical grade surface flatness is required[1] and in applications that

employ an array of microstructures where the array uniformity is critical[2,3]. CTE mismatch problems are often encountered in silicon MEMS devices that employ metallic films due to low CTE of silicon. Thermal deformation for two layers can be found in the literature[4]. A recent theoretical work discusses the deformation on hinged multilayer media considering developed initial strains[5].

The same phenomenon may also be implemented as a transducer that converts thermal energy into mechanical deflection, which is the basic energy transformation for the designed thermal detector arrays. In order to understand the basics, thermal deflection is studied for multi – layer structures. Fig.4.1 shows a general m-layer structure anchored from one edge. Assume the thickness, CTE, and Young's modulus of material in "layer i" are h_i, α_i and E_i, respectively, and all layers have the same length (L) and width (b). N_i and M_i are the effective force and moment assigned to the tip of each layer with the sign convention illustrated in the figure.

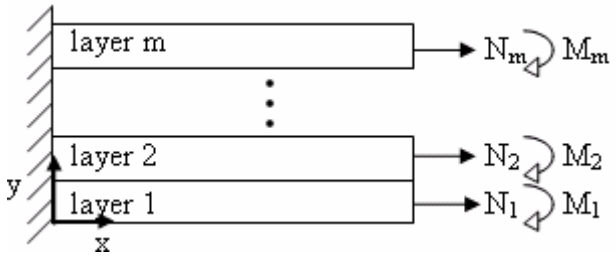

Fig.4.1. One-end-fixed and one-end-free m-layered structure. All layers have same length (L) along x-axis and width (b) along z-axis.

From conservation laws, the sum of forces and moments should sum up to zero when the static equilibrium is reached:

$$N_1 + N_2 + \ldots + N_m = 0 \tag{4.1}$$

$$M_1 + M_2 + \ldots M_m + N_1 \frac{h_1}{2} + N_2 (h_1 + \frac{h_2}{2}) + \ldots + N_m (h_1 + h_2 + \ldots h_{m-1} + \frac{h_m}{2}) = 0 \qquad (4.2)$$

Equation relating the moment to force for each layer can be written as:

$$M_i = \frac{E_i b h_i^{\,3}}{12\rho} \quad \text{for i = 1 to m} \qquad (4.3)$$

where ρ is defined as the radius of curvature for the bent structure. Total strains at layer boundaries should be equal, resulting in a set of (m-1) equations:

$$\alpha_i \Delta T + \frac{N_i}{E_i b h_i} + \frac{h_i}{2\rho} = \alpha_{i+1} \Delta T + \frac{N_{i+1}}{E_{i+1} b h_{i+1}} - \frac{h_{i+1}}{2\rho} \qquad \text{for i = 1 to m-1} \qquad (4.4)$$

Where ΔT is the induced temperature difference. Combining Eqn. 4.1 thru 4.4 results in a set of (m+1) linear equations for a general m-layer case with one-end-fixed and one-end-free structures with (m+1) unknowns N_1, N_2,…, N_m, and $(1/\rho)$[6]:

$$\begin{bmatrix} 1 & 1 & 1 & \ldots & 1 & 0 \\ \frac{h_1}{2} & h_1 + \frac{h_2}{2} & h_1 + h_2 + \frac{h_3}{2} & \ldots & h_1 + h_2 + \ldots + \frac{h_m}{2} & \sum_{i=1}^{m} \frac{E_i b h_i^{\,3}}{12} \\ \frac{1}{E_1 b h_1} & \frac{-1}{E_2 b h_2} & 0 & 0 \ldots & 0 & \frac{h_1 + h_2}{2} \\ 0 & \frac{1}{E_2 b h_2} & \frac{-1}{E_3 b h_3} & 0 \ldots & 0 & \frac{h_2 + h_3}{2} \\ & & & \vdots & \vdots & \\ 0 & 0 & \ldots & 0 \quad \frac{1}{E_{m-1} b h_{m-1}} & \frac{-1}{E_m b h_m} & \frac{h_{m-1} + h_m}{2} \end{bmatrix} \cdot \begin{bmatrix} N_1 \\ N_2 \\ \vdots \\ N_m \\ 1/\rho \end{bmatrix} = \begin{bmatrix} 0 \\ 0 \\ (\alpha_2 - \alpha_1)\Delta T \\ (\alpha_3 - \alpha_2)\Delta T \\ \vdots \\ (\alpha_m - \alpha_{m-1})\Delta T \end{bmatrix} \qquad (4.5)$$

ρ can be solved using the above matrix of equations. Assuming the tip deflection at the free-end of the structure (δ) is small compared to its length, then it can be expressed in terms of ρ as:

$$\delta = \frac{1}{2\rho} L^2 \Delta T \tag{4.6}$$

4.2.2 Verification of Model with a Test Structure

Before the fabrication of the thermal detectors, the analytical model and FEM simulations are verified with a MEMS scanner. MEMS structure analyzed for the verification of the developed analytical solution and the FEM simulations is a raster correction scanner (RCS), which can be added as a third scanner to retinal scanning display systems[7] to improve the raster and image quality. Retinal scanning displays employ two uniaxial or one biaxial scanner to paint a scanned image on the viewer's retina in a 2-D raster format using point light sources with high-luminance.

The scanner is fabricated by Microvision, Inc. at the Washington Tech. Center using a double-side polished 100 Silicon wafer. The mirror and the flexures are formed using DRIE as opposed to KOH etch to maintain better tolerances while etching through the relatively thick wafer. A thin Aluminum film (0.2 μm) forms a highly reflective mirror surface and the gold coils (6 μm) for electromagnetic actuator are deposited at the back surface (see Fig.4.2 for illustration). The scanner is a multi layer MEMS structure and can be thermally deformed during normal operation due to temperature increase induced by the current flowing across the coils of the actuator.

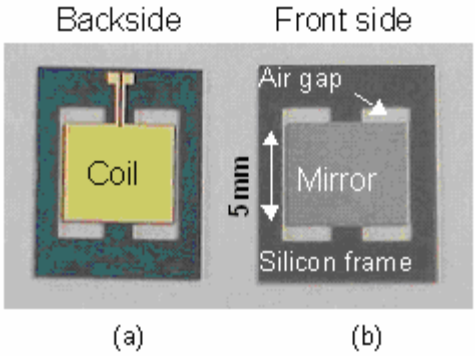

Fig.4.2 Torsional raster pinch scanner (a) front and (b) back sides.

For a three layer structure with thick middle layer (i.e., $h_2 >> (h_1, h_3)$), we can find a 1st order approximate solution for δ using Eq.4.4 – Eq.4.7.

$$\delta = \left[3E_1 h_1(\alpha_2 - \alpha_1) + 3E_3 h_3(\alpha_3 - \alpha_2)\right] \cdot \frac{L^2 \Delta T}{E_2 h_2^2} \tag{4.8}$$

For a parametric design study, we can define dimensionless layer thickness ratio parameters: $x = (h_1 / h_2) << 1$ and $y = (h_3 / h_2) << 1$ and rewrite the above equation:

$$\delta = \left[3E_1 x(\alpha_2 - \alpha_1) + 3E_3 y(\alpha_3 - \alpha_2)\right] \cdot \frac{L^2 \Delta T}{E_2 h_2} \tag{4.9}$$

Mirror deformation was measured with an optical interferometer while applying DC current to the coils without the external magnets. The scanner remains still but heats up due to resistive power dissipation. The zero-stress temperature for the structure is near the deposition temperature of the coils, which is around 35 ^{o}C. When the power dissipated at the coils is 245 mW, the coils heat up an additional ΔT = 46.5 ^{o}C from its zero-stress temperature and the deflected mirror shape is as shown in Fig.4.3.a with a maximum p-v

deflection of 0.51 μm observed at the corners. The FEM simulation result for the same case is given in Fig.4.3.b and shows a maximum p-v deflection of 0.54 μm at the corners, which is in good agreement with the experimental result.

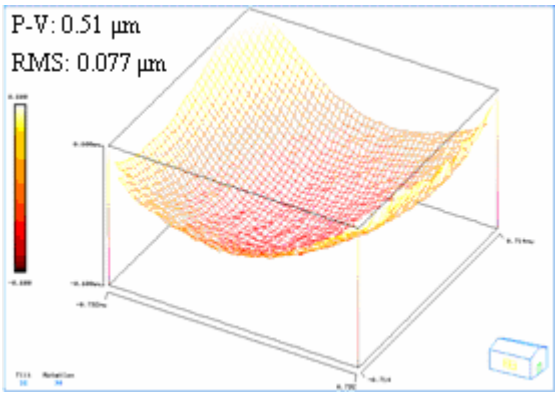

(a)

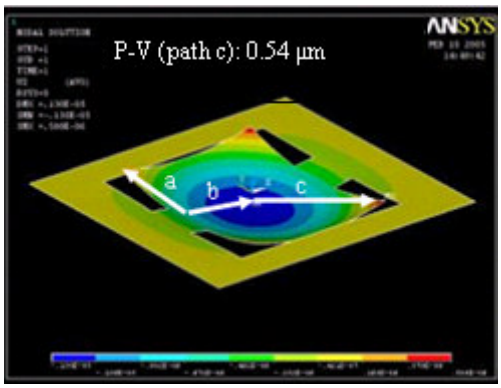

(b)

Fig.4.3 Thermal deformation for $\Delta T=46.5^{o}C$ temperature rise for structure in Fig.4.2. (a) Experimental result measured with an optical interferometer, only mirror surface is shown, (b) FEM simulation result using ANSYS™ including mirror and the frame.

Analytical results can be compared with FEM and experimental results along the three cross-sectional paths *a*, b, and c as defined in Fig.4.3.b. Fig.4.4 shows a comparison between analytical and FEM solutions where Si thickness is a parameter, while Au and Al thickness are fixed at 6μm and 0.2μm. Deformation decreases with square of the Silicon thickness as predicted by Eq. 4.8. Results agree very well along path *a* as the fixed-free beam assumption is valid. Along path b, analytical prediction for deflection amplitude is smaller by 13% (note the sign of deflection is negative in this case). This error is expected as the scanner cross-section behaves as fixed-guided beam from anchor-to-center of the mirror while our formulas predict the deformation for a fixed-free beam. For path c, analytical predictions are larger by 18%. The error is again expected as the scanner cross-section behaves as guided-free beam

from center-to-corner of the mirror while our formula predictions are for a fixed-free beam. For this geometry, the corresponding error factors can be added to the actual analytical predictions to make the analytical predictions more accurate.

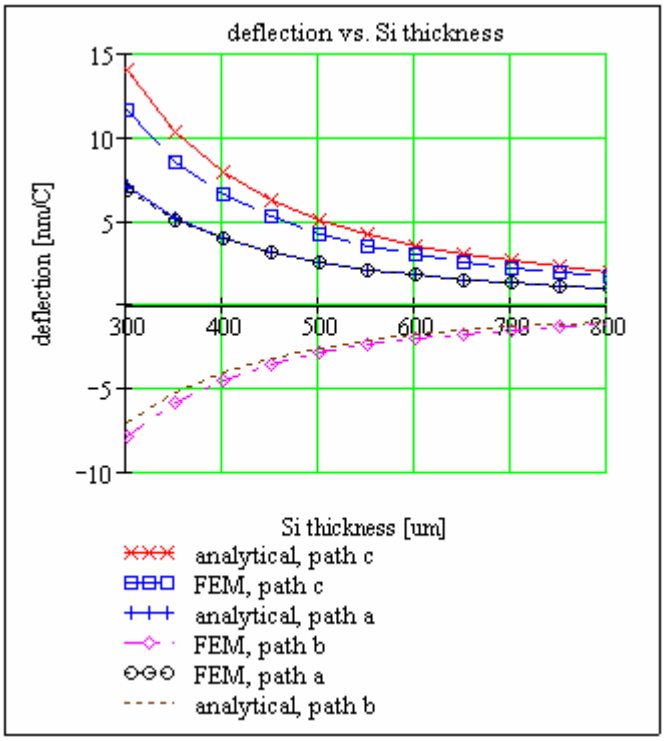

Fig.4.4 Comparison of the deflection amplitude between analytical solution and FEM simulation along paths *a*,b and c. Note that, for $\Delta T>0$, δ_a, $\delta_c > 0$ and $\delta_b < 0$.

Figure 4.5 shows the thermal deformation as a function of temperature and demonstrates that FEM and experimental results agree particularly well for large temperature differences, while the analytical predictions (calculated along path c) are larger than FEM predictions by 18% due to the approximations made by modeling the 3D structure by a fixed-free simple beam.

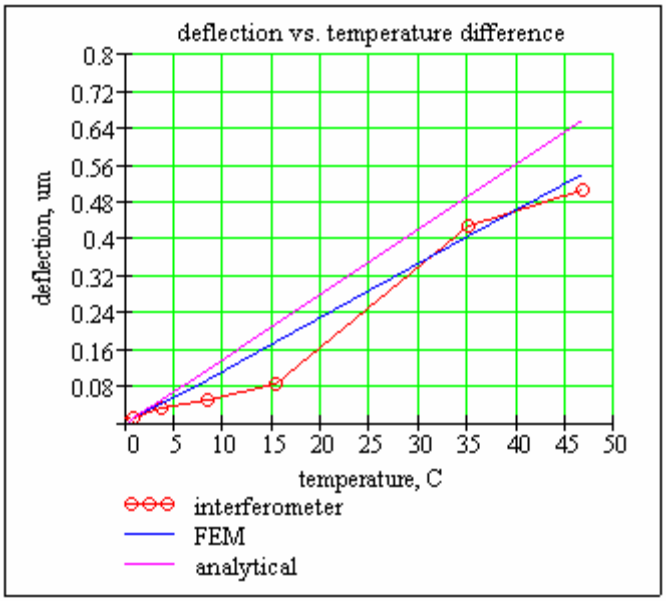

Fig.4.5 Comparison of thermal deflection as a function of temperature difference for analytical solution along path c, FEM simulation, and interferometric measurement results.

Fig.4.6.a illustrates the analytical results for thermal deflection vs. temperature for a large range of Au and Al thickness values assuming Si is 300 μm and the scanner is $5\times5mm^2$. The approximation given for Eq.4.9 is valid for small δ and for x, y smaller than 1/30 (validity range of the assumption is illustrated in Fig.4.6.b). Film thickness larger than 10μm is hard to achieve with standard deposition methods. Even though figure shows one particular design point, the contour plot remains valid if all the thicknesses in the figure labels are divided by a scaling factor and the contour line values are multiplied by the same scaling factor. If the size of the scanner changes, then contour values should be scaled by L^2.

Fig.4.6.b shows the analytical solution given in Eq.4.5 and Eq.4.6 and the approximate analytical solution in Eq.4.8 for a thick Si structure sandwiched between thin Al and Au films. Note that, the approximate formula works well for thin films, particularly around the

δ=0 curve, which gives the thickness combinations that make the structure athermal. For the microscanner application, such a tradeoff helped improve the performance of the scanner. Initial design had 6 μm Au coils and 0.2 μm Al, which is sufficiently thick for good reflectivity. Later the Al thickness was increased to about 3 μm, which reduced the thermal deformation from +7.5 nm/°C to about 1 nm/°C.

Fig.4.6.c illustrates the approximate deformation formula in Eq.4.9 using the thickness ratios x and y. The contour labels show the deformation normalized with a Si thickness, temperature difference, and the scan mirror size. The figure allows for easy performance trades for the 3-layer structure used in our case study.

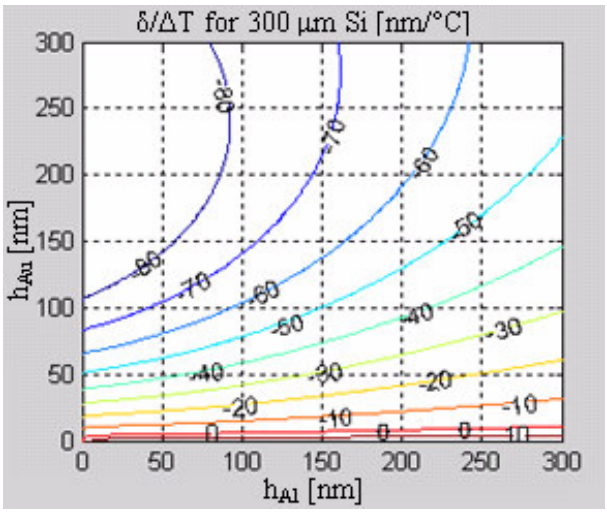

(a)

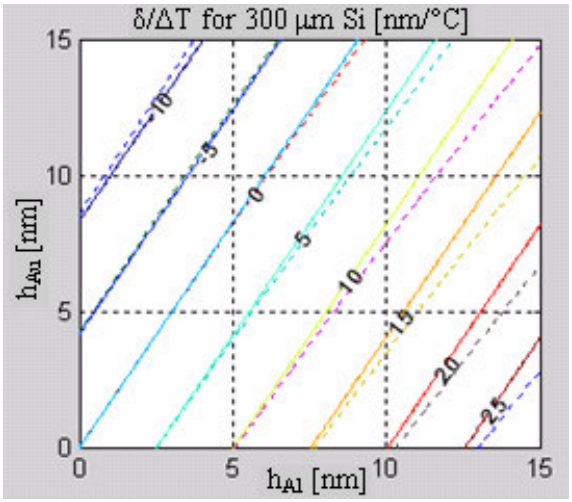

(b)

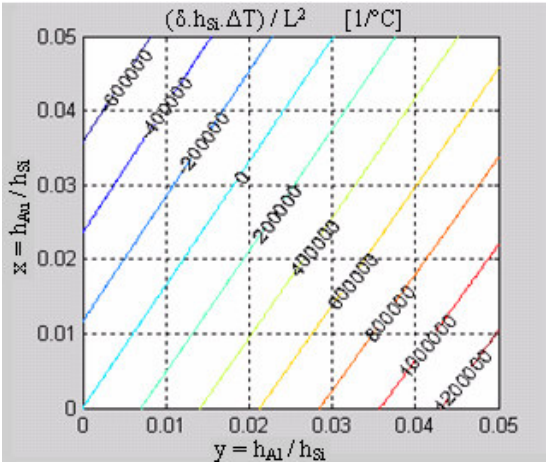

(c)

FIG.4.6 (a) Thermal deformation of the scanner versus metal layer thicknesses. (b) Comparison of exact (dashed) and approximate (solid) expressions. (c) Deformation curve given in dimensionless parameters

4.3 Thermo – Mechanical Response of the Detector

The temperature induced on the detectors as a result of the absorption of radiation is converted into mechanical deflection by the help of the bimaterial legs that support the membranes. Since the deflection is to be sensed by optical means, the deflection per Kelvin temperature induced on the detectors should be maximized. The amount of deflection depends on the material properties as well as the thicknesses and lengths of the cantilever legs as given in Eq.4.5 and Eq.4.6. The general solution for m – layer structures can be simplified for bimaterial (two layer) cantilevers as below:

$$\delta = \frac{3 \cdot E_1 \cdot E_2 \cdot h_1 \cdot h_2 \cdot (h_1 + h_2) \cdot (\alpha_2 - \alpha_1) \cdot \Delta T \cdot L^2}{(E_1 \cdot h_1 + E_2 \cdot h_2) \cdot (E_1 \cdot h_1^{\,3} + E_2 \cdot h_2^{\,3}) + 3 \cdot E_1 \cdot E_2 \cdot h_1 \cdot h_2 \cdot (h_1 + h_2)^2} \qquad (4.7)$$

It is apparent that the larger the mismatch between CTE's of the materials, larger the deflection. Table 4.1 shows some other material constants for the common materials for microfabrication. Table 4.1 illustrates material properties for common IC materials. For our prototypes Al and SiN_x are preferred for large CTE mismatch.

Material	CTE, α (10^{-6} K^{-1})	E (GPa)	k (W/K)	c (J/kg.K)	d (kg/m^3)
Si	2.6	162	149	700	2420
Al	25	69	237	908	2700
Au	14.3	80	318	130	19400
SiN_x	0.8	180	18.5	691	2400
SiO_2	0.4	67	1.4	1000	2660

Table 4.1: Material Properties

The deflection increases quadratically with the bimaterial layer length. On the other hand the dependence of the deflection on the layer thicknesses is more complex. The length of the bimaterial layer is limited by the pixel pitch size for the detector implementation. Pixel pitch size of typical detectors at present is 50 μm and the trend is to design and implement FPAs with 25 μm pixel pitch size. Pixels with 25, 50, 100 and 200 μm pitch sizes were designed for the prototypes. For the design variation that has the longest bimaterial leg, the bimaterial leg length is equal to the pixel pitch size.

Fig.4.7 shows the expected deflection as a function of Al and SiN_x thicknesses assuming 50 μm pixel pitch size.

It is apparent from the given figure that the larger deflection values are achievable for using thinner layers. One limitation for the nitrite layer thickness comes from the IR absorption analysis. The optical absorption is maximized when the thickness of the nitride

layer is about 500 nm. For this specific point, the deflection could be maximized when the thickness of Al layer is about 350nm. The limitation on the thickness of Aluminum layer usually comes from microfabrication. Aluminum is one of the best choices to give large CTE mismatch with Silicon Nitride; however it may easily be oxidized. The material properties may change tremendously if the metal layer is oxidized. Since the oxidation takes place at the surface of the layer, it affects the thinner layers more than the thicker ones. As a result, the metal layer thickness of the fabricated arrays was each varied between 300 nm and 600 nm.

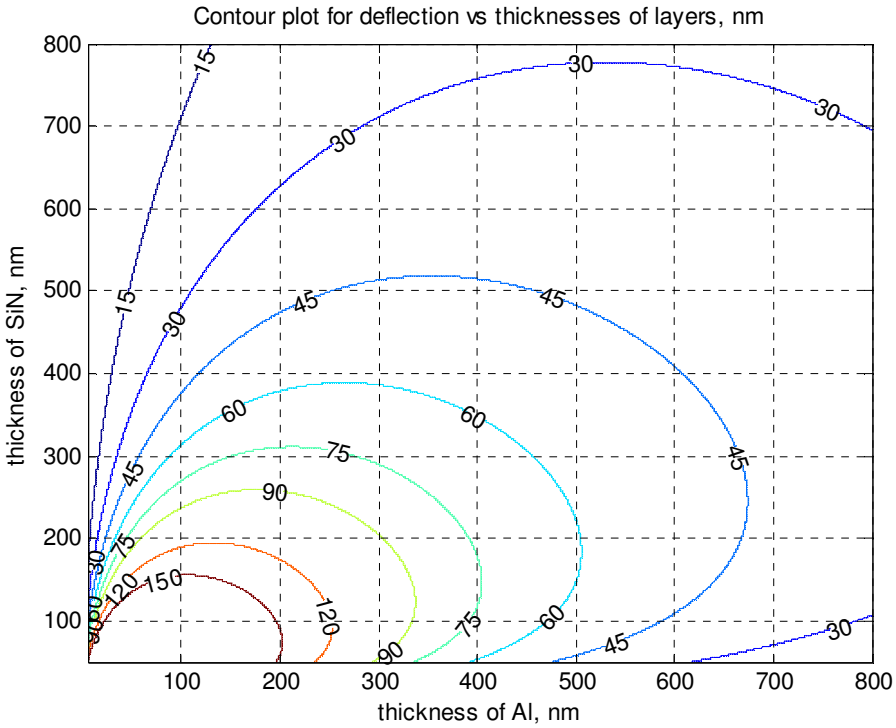

Fig.4.7 Deflection values for a bimaterial made of Aluminum and Silicon Nitride

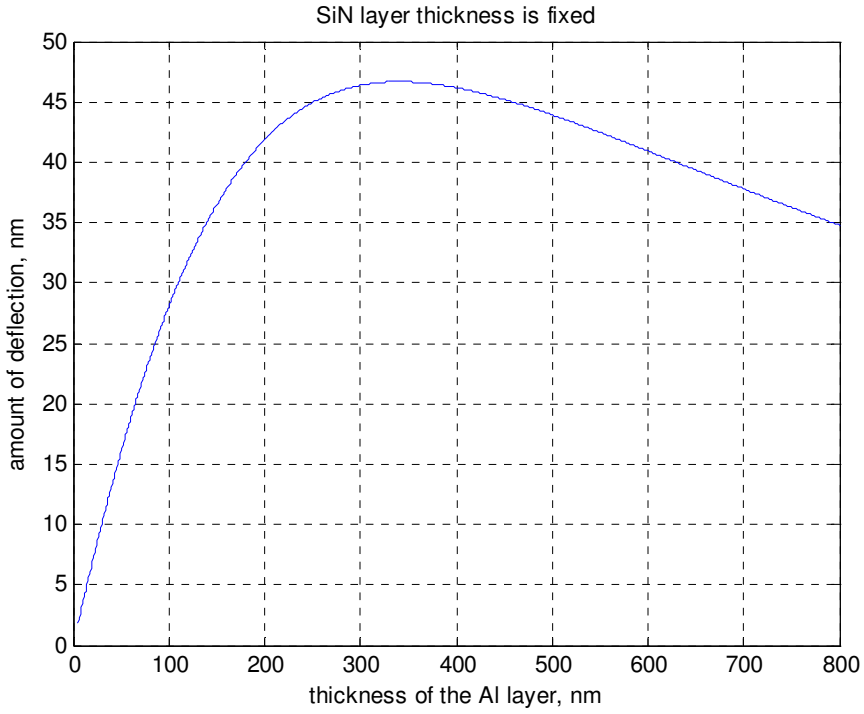

Fig.4.8 Deflection as a function of Al layer when the nitride layer is fixed at 500 nm

The dependence of the deflection to the thickness of SiN_x layer for a fixed thickness of Al is stronger as seen from Fig.4.9. In this graph, the thickness of Al layer is fixed at 350 nm as a case study, which gives maximum deflection for a nitride layer of 500 nm. The deflection can nearly be doubled for thinner SiN_x layers from the optimization for a fixed thickness of Al. To operate the detectors at those thicknesses at bimaterial legs without degrading the absorption, it is necessary to deposit the dielectric layer in two levels, which means another mask is necessary. In order to keep the microfabrication simpler, one nitride layer is deposited at 500 nm, which maximizes IR absorption.

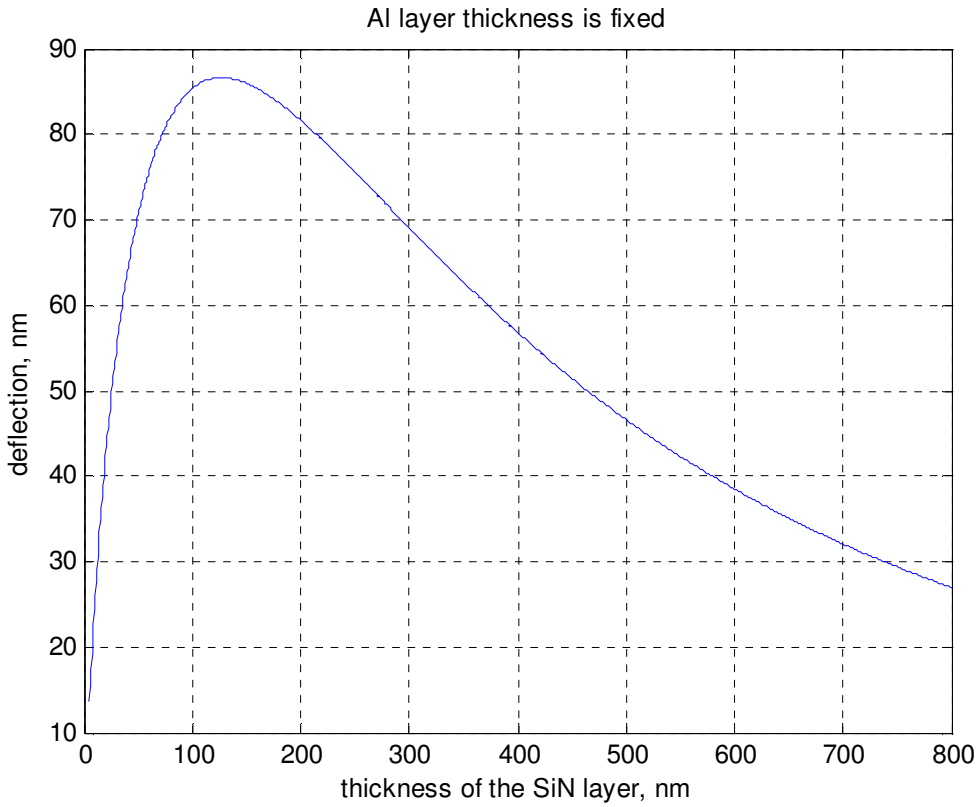

Fig.4.9 Deflection as a function of SiN_x layer when the Aluminum layer is fixed at 350 nm

4.3.1 FEM Simulations

The deflection simulation of the detector with a bimaterial leg of 50 μm for an induced 1°C temperature difference induced on it is shown in Fig.4.10. The maximum deflection is 0.453E-7 m for a bimaterial leg of 500 nm Al on top of 500 nm SiN_x. The analytical model gives a deflection of 45.38nm which is in very good agreement with the FEM results.

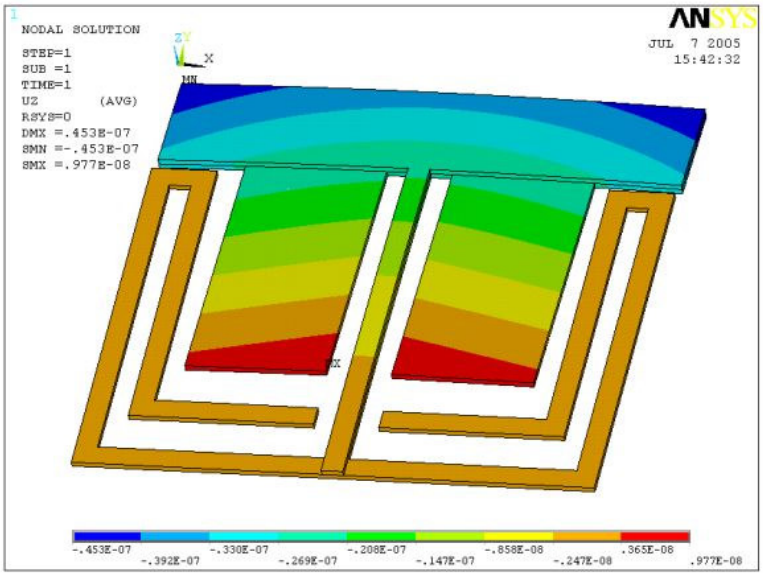

Fig.4.10 FEM simulation for the deflection of thermal detector pixel

For the same detector pixel, modal analysis is performed. As shown in Fig.4.11 the first resonant frequency is almost 40 kHz, and there is a good separation between 1st and 2nd modes, which is around 120 kHz.

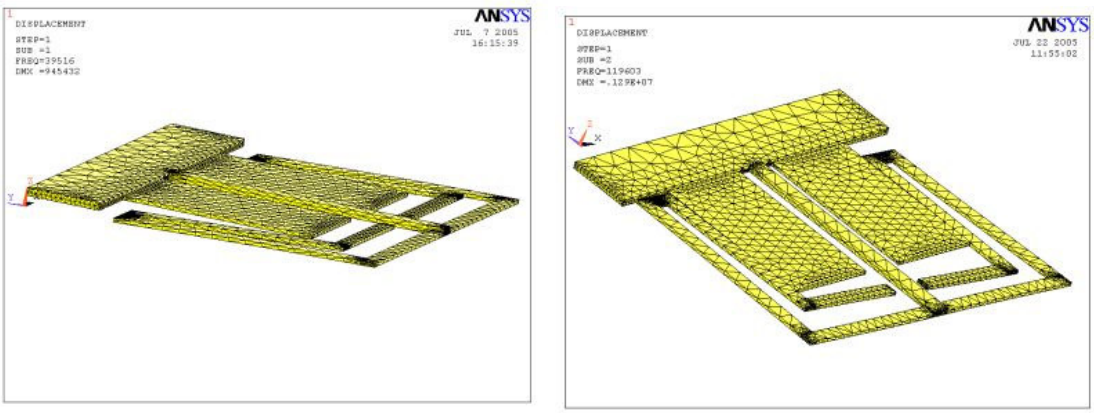

Fig.4.11 (a) 1st mode of the motion (b) 2nd mode of the motion of the detector

FEM deflection result for another design, which was fabricated, is given in Fig.4.12. For this design the bimaterial legs connect the middle of the membranes to the isolation legs. It is apparent from the given figure that the deflection along the bimaterial legs displaces the isolation legs because of the boundary conditions at the intersection points, as a result of which larger deflections are possible.

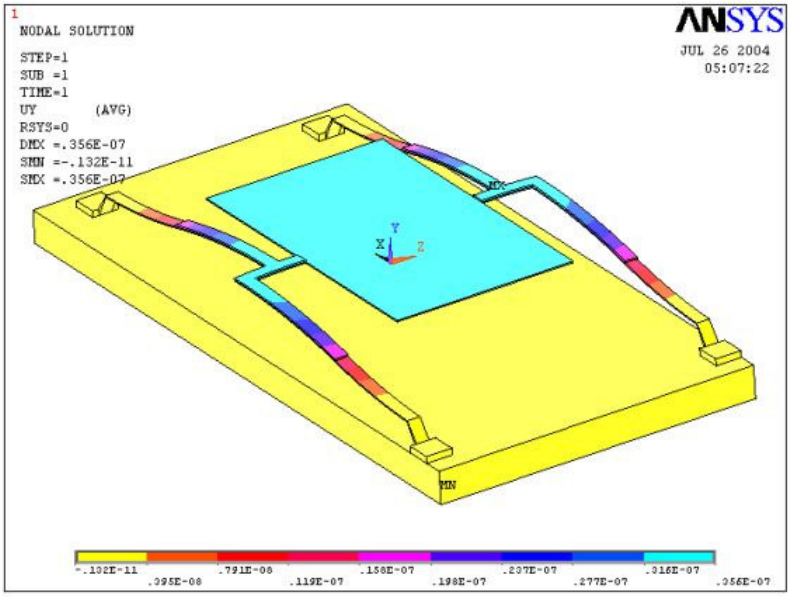

Fig.4.12 FEM simulation for the deflection analysis of the design of which the membranes are connected from the mid parts

For the design given in Fig.4.13, the bimaterial legs are connected to the isolation legs at right angles in order to save space and increase the detector fill – factor; however due to that intersection displacement cancellation occurs. As it may be noticed, the isolation legs bend towards substrate whereas the bimaterial legs bend in the opposite direction. As a result of this, the net displacement becomes negligible, ~0.3 nm. Thus the design is not considered in our prototypes. This design can be modified to give a very good performance by swapping the Al and SiN_x layers[8].

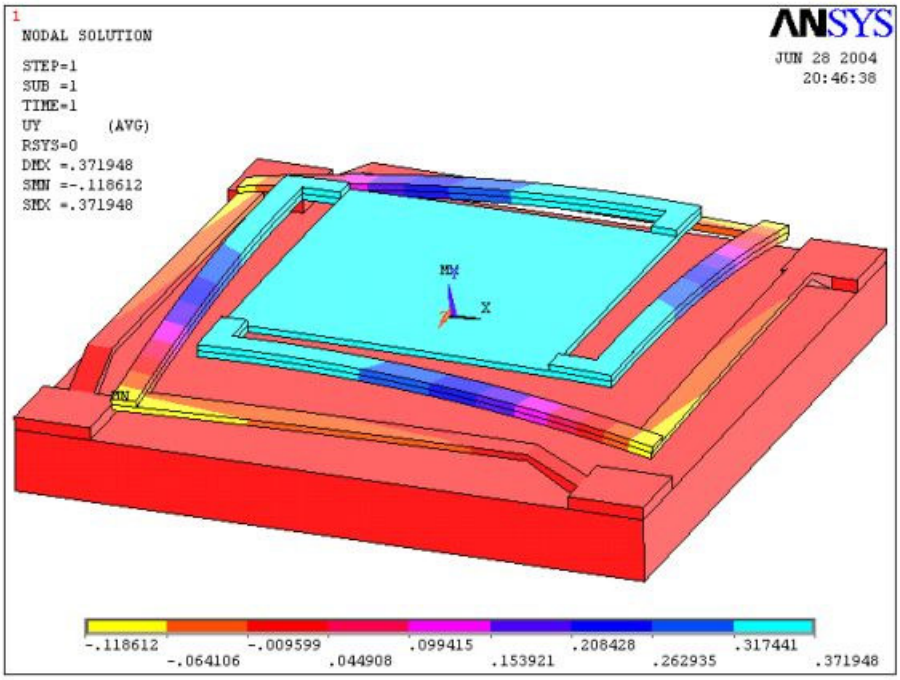

Fig.4.13 FEM simulation for the crab – legged detector pixel

4.4 Noise Analysis

The detector noise performance can be predicted by combining the IR absorption and thermo – mechanical response models developed so far.

4.4.1 Figures of Merit

Noise equivalent power (*NEP):* defined as the input signal power that gives a signal-to-noise ratio of one.

$$NEP = \frac{N}{R} \tag{4.10}$$

where N is the RMS noise magnitude of the measured quantity. For microcantilever type thermal detectors, the measured quantity is the displacement of the microstructure from its rest position. R is the detector responsivity and can be defined as the displacement per absorbed power by the detector.

Detectivity (D):* Since NEP strongly depends on the absorbed power which depends on the various parameters such as the size of the detector and its bandwidth, one can not compare the actual performances of different detectors by just looking at the values of NEP. D^* is a commonly used normalized parameter defined to predict the detector performance more realistically.

$$D^* = \frac{\sqrt{\beta \cdot A \cdot \Delta f}}{NEP} \tag{4.11}$$

where A, β and Δf are the area, fill factor, and the bandwidth of the detector, respectively. Detectivity is usually reported for a $1cm^2$ detector using 1 Hz bandwidth.

Noise Equivalent Temperature Difference (NETD): Detectivity gives much more information on the performance of detectors as compared to NEP, however by definition it still includes dependency on some of the crucial parameters such as the spectral information of the emitted IR radiation from the target, transmission losses of the emitted radiation through propagation, and the ratio of the collected radiation by the IR optics of the detector. NETD, is defined as the ultimate figure of merit that shows the performance of detectors[9].

$$NETD = \frac{4 \cdot f_{no}{}^{2} \cdot NEP}{\eta \cdot \tau_0 \cdot \beta \cdot A \cdot (dP/dT)_{\lambda 1 - \lambda 2}} \tag{4.12}$$

where f_{no} is the f-number of the IR optics, η is the emissivity of the detector, τ_0 is the transmittance of the medium in which IR radiation is propagating and *(dP/dT)* shows the change in power per unit area radiated by a blackbody at temperature *T* measured within spectral window λ_1 to λ_2.

4.4.2 Thermo – Mechanical Noise

Thermo – mechanical noise is a fundamental noise source due to the nature of the released mechanical structures such as microcantilever based thermal detectors. The driving force of this noise source is the thermal energy, which is the product of Boltzmann's constant (k_B) and the temperature (T) in Kelvin specifying the average amount of thermally induced energy that is available per mode of the mechanical structure. For any mechanical structure, which is kept in thermal bath with its environment, there is a continuous energy exchange between the mechanically stored energy and the thermal energy present in the environment.

Microcantilever thermal detectors can be considered as mechanical resonators. The described energy exchange causes some mechanical fluctuations in the vibrating microcantilever. For off-resonance operation the mechanical fluctuations can be formulated as[3]:

$$\delta z_{TM} = \sqrt{\frac{4 \cdot k_B \cdot T_D \cdot \Delta f}{k \cdot \omega_0 \cdot Q}} \tag{4.13}$$

where δz is the RMS noise magnitude of the displacement, k_B is the Boltzmann's constant T_D is the temperature of the detector, and k, Q and ω_0 are the spring constant, quality factor and resonant frequency of the mechanical structure, respectively. This expression, giving a measure of noise specific to the thermomechanical noise, can be combined with Eq.4.10, Eq.4.11 and Eq.4.12 so that the NETD as a result of thermo – mechanical noise can be calculated as:

$$NETD_{TM} = \frac{8 \cdot f_{no}{}^2 \cdot \sqrt{k_B \cdot T_D \cdot \Delta f}}{\eta \cdot \tau_0 \cdot \beta \cdot A \cdot (dP/dT)_{\lambda 1-\lambda 2} \cdot R \cdot \sqrt{k \cdot \omega_0 \cdot Q}} \tag{4.14}$$

4.4.3 Thermal Fluctuation Noise

Thermal Fluctuation noise is the fundamental noise source for all types of thermal detectors, since it causes fluctuations on the temperature of a detector as a result of continuous heat exchange between the detector and its environment. The fluctuations on the temperature can be minimized if the detector is thermally isolated from its environment. In the best case, the heat exchange is only through radiation and this case sets the background fluctuation noise limit. Since this is a special condition, the noise associated to it is examined separately. Apart from that the temperature fluctuations on the detector can be expressed as:

$$\delta T = T_D \cdot \sqrt{\frac{4 \cdot k_B \cdot \Delta f}{G}} \tag{4.15}$$

where G is the thermal conductance of the detector. Sticking to the definitions given before, the temperature fluctuation should be related to the noise magnitude of mechanical displacement in order to calculate the noise equivalent temperature difference value associated with temperature fluctuation noise. Responsivity of the detector can be defined as

the product of temperature difference induced on the detector per absorbed IR power (P_0) and the deflection along the bimaterial leg (z) per temperature difference:

$$R = \frac{T_D}{P_0} \cdot \frac{z}{T_D} \tag{4.16}$$

Thermal conductance is defined as the power increase per unit temperature increase on a system. Combining these definitions together with the Eq.4.15 and Eq.4.16, mechanical fluctuation on the detector as a result of thermal fluctuation and the corresponding NETD can be expressed as:

$$\delta z_{TF} = R \cdot T_D \cdot \sqrt{4 \cdot k_B \cdot \Delta f \cdot G} \tag{4.17}$$

$$NETD_{TF} = \frac{8 \cdot {f_{no}}^2 \cdot T_D \sqrt{k_B \cdot G \cdot \Delta f}}{\eta \cdot \tau_0 \cdot \beta \cdot A \cdot (dP/dT)_{\lambda 1 - \lambda 2}} \tag{4.18}$$

4.4.4 Background Fluctuation Noise

Thermal conductance for any type of structure cannot be minimized any further than the value for which the heat exchange between the detector and the environment is through radiation. This is the fundamental limit for any kind of device that is used to detect infrared radiation. For radiation limited case, heat flux can be given as[10]:

$$q_{net} = \varepsilon\sigma({T_D}^4 - {T_B}^4) \tag{4.19}$$

where σ is the Stefan – Boltzmann's constant, ε is the emissivity of the detector and T_B is the temperature of the background. The thermal conductance for radiative heat transfer can be defined as in Eq.4.20 due to the fact that the detector is operational at a temperature very close to background:

$$G_R = 4 \cdot \beta \cdot A \cdot \sigma \cdot \varepsilon \cdot T_D^{\,3} \tag{4.20}$$

This equation is valid if the detector temperature is close to the temperature of the background environment, which is the case for the uncooled thermal detectors. Substituting the conductance value into equation (4.18), one can get the NETD value associated with the background fluctuation noise:

$$NETD_{BF} = \frac{16 \cdot f_{no}^{\,2} \cdot \sqrt{k_B \cdot \sigma \cdot \Delta f \cdot T_D^{\,5}}}{\eta \cdot \tau_0 \cdot \sqrt{\beta \cdot A} \cdot (dP/dT)_{\lambda 1 - \lambda 2}} \tag{4.21}$$

Note that the BF noise is much lower for cooled detectors at cryogenic temperatures.

4.4.5 Total Noise Performance of the Detector Array

The noise components for the pixel design illustrated in Fig.4.14 are plotted as a function of thermal conductance in Fig.4.15. For the noise analysis, the transmittivity of the atmosphere is assumed 0.9, the operating temperature of the detector array is assumed 300 K, and F/1 imaging lens is assumed. The achievable absorptivity was shown to be 0.8 in Chapter 3. Mechanical parameters such as the spring constant and the resonant frequency are obtained from FEM simulations given in Fig.4.11.

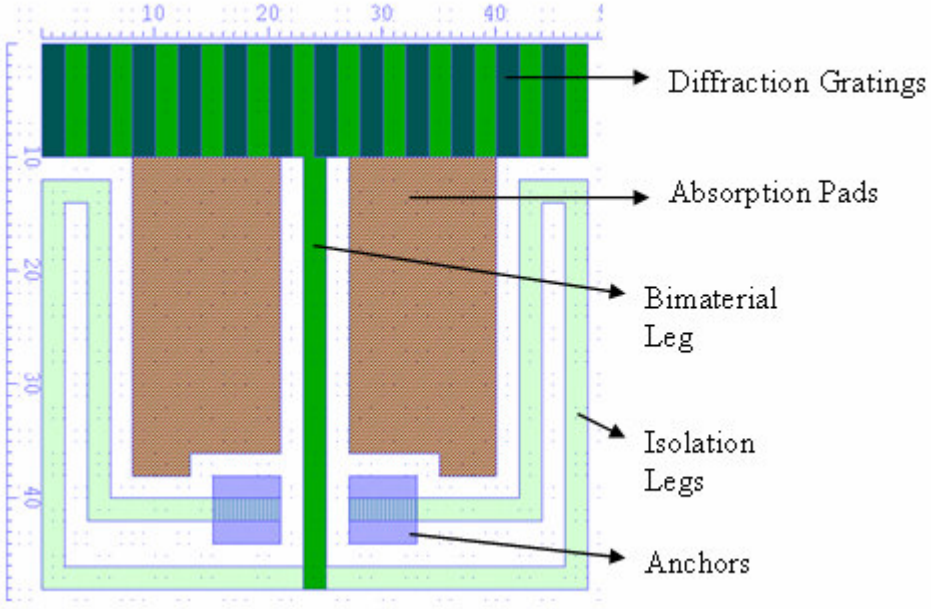

Fig.4.14 Top view of design prototype with a scale in μm

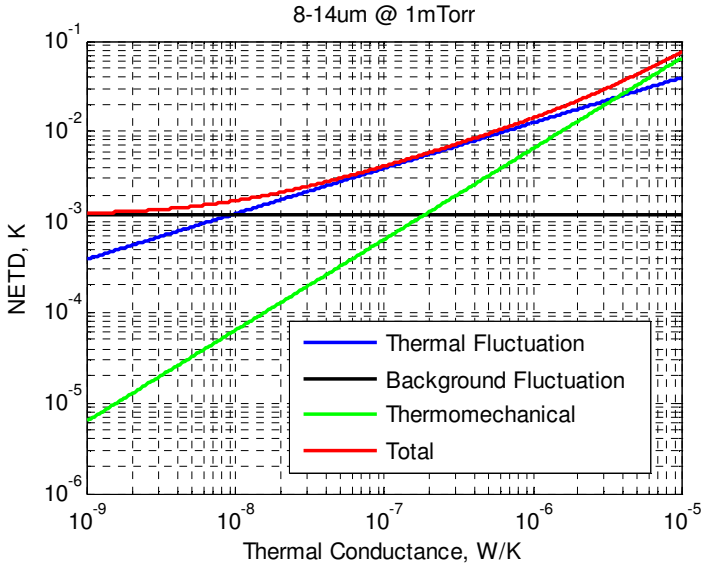

Fig.4.15 Noise Equivalent Temperature Difference as a function of thermal conductance

As seen from Fig.4.15, it is crucial to optimize the pixels such that the thermal conductance would be minimized for better performance levels. The thermal model of the detector design given in Fig.4.14 is given in Fig.4.16. Here *R* is the corresponding thermal resistance, which is *1/G*.

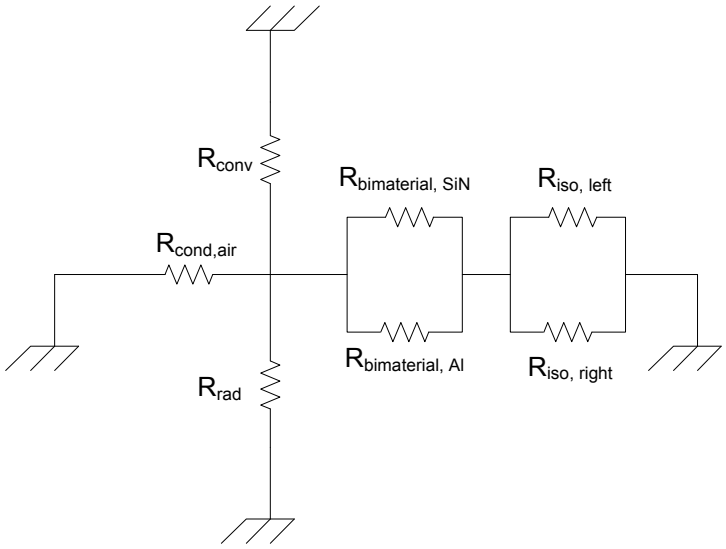

Fig.4.16 Thermal Model of the Detector

First of all there is a thermal path to transfer heat from the absorption pads to the substrate through air by radiation for which the thermal conductance is given in Eq.4.20. For the design prototype, G_{rad} = 6.45 nW/K. Secondly, heat transfer can be made through air convection. For that analysis, Grashof (Gr_L) and Reynold (Re_L) numbers are defined as[11]:

$$Gr_L = \frac{g\beta(T_D - T_S)L^3}{\upsilon^2} \tag{4.22}$$

$$\mathrm{Re}_L = \frac{\rho u_\infty L}{\mu} \tag{4.23}$$

where g, β, T_D, T_S, L, ν, ρ, u_∞ and μ are respectively the gravitational constant, volumetric CTE, temperature of the detector, temperature of the heat sink (i.e. substrate), length between the membrane and the substrate, kinematic viscosity, mass density, mass average fluid viscosity and viscosity, respectively. It is assumed that the detector operates at 300 °K with unity temperature difference between the detector and the substrate. According to these assumptions, the parameters in Eq.4.22 and Eq.4.23 are given in Ref.12. Natural convection may be neglected if $Gr_L / \mathrm{Re}_L << 1$ holds. Assuming the membrane displacement is 1 μm in 1 ms, the given ratio becomes 0.033, then the conductance due to convection (G_{conv}) can be neglected.

Thermal conductance due to the legs that connect the membranes to the substrate may be calculated from Eq.4.24.

$$G_{cond} = \left[\left(R_{bimaterial,SiN}{}^{-1} + R_{bimaterial,Al}{}^{-1} \right)^{-1} + \left(R_{iso,left}{}^{-1} + R_{iso,right}{}^{-1} \right)^{-1} \right]^{-1} \tag{4.24}$$

where thermal resistance is defined as:

$$R = \frac{L}{kA} \tag{4.25}$$

where L is the length of the structure that connects the bodies in heat transfer, k is the thermal conductivity, and A is the cross sectional area of the structure. For the design geometry, G_{cond} = 0.32 μW/K.

Thermal conductance due to air ($G_{cond,air}$) is usually neglected for conventional mechanical structures, however for microstructures, the effect may be dominant. For instance, $G_{cond,air}$ = 50 μW/K for the design geometry since thermal conductivity of air at 300 °K at atmospheric pressure is 26.3E-3 W/m.K. Therefore the performance would be dramatically degraded if the detector is operated at atmospheric pressure. Thermal conductivity of air reduces with pressure, thus the detector needs to be operated in vacuum a common requirement for all IR detectors. In order to decrease the air conductance to an acceptable level, the pressure should be decreased since the thermal conductivity of air depends on pressure[13]. The thermal conductance due to air through conduction can be decreased below 10 nW/K at a pressure of 1mTorr. For that case, the thermal conductance is limited with the conduction through the legs that connect the membranes to the substrate. The legs are optimized such that the conductance is low by selecting the materials with low thermal conductivity and maximizing the length of the isolation legs.

In terms of NETD, going below 10 mK is challenging even for uncooled IR detectors. It is calculated that $NETD_{BF}$ = 1.3 mK, $NETD_{TF}$ = 7.1 mK, and $NETD_{BF}$ = 2.1 mK which makes total NETD 7.5 mK with the current thermal isolation level for the fabricated thermal detector pixels. Further improvements in thermal isolation can be possible by making the legs narrower by decreasing the minimum linewidth for the microfabrication. Moreover, with the optimization of IR absorber and bimaterial legs given previously, it is possible to have an NETD value less than 5 mK.

4.5 Thermal Response Time of the Detector

The membranes should be thermally isolated for the best noise performance. On the other hand, as thermal isolation gets better, it takes longer for the membranes to reach the steady state temperature. For imaging applications it is crucial to limit the time needed to reach

steady state condition, which defines the frame rate of the imager. Quantitatively, the heat diffusion may simply be modeled as in Ref.4.14:

$$\frac{dT}{dt} = -\frac{\bar{h}A}{\rho cV}(T - T_{\infty}) \tag{4.27}$$

where $\bar{h}$ *(W/m²K)* is the heat transfer coefficient, *A* is the area of the thermal body, *c (J/kgK)* is the specific heat capacity, and *V* is the volume of the body. The product of area and heat transfer coefficient is defined as the thermal conductance; whereas ρcV is the heat capacity *(C)* of the structure. Therefore, the solution of this equation for the thermal detector can be given as follows:

$$\frac{T - T_{\infty}}{T_i - T_{\infty}} = \exp(-\frac{t}{\tau}) \tag{4.28}$$

where $\tau = C/G$ is the time constant of the detector. In order to make a faster detector without degrading noise performance, the heat capacity of the detector should be decreased. For the design shown in Fig.4.10 where SiN_x is used as IR absorber, thermal time constant is calculated to be 13 msec, which allows the detector to operate at 60 frames per second (fps).

Thin metal films can be used as IR absorber so that the heat capacity is lower. That is due to the fact that the thermal conductivity for metals are usually much larger than that of dielectric films.

References:

1. H. Urey, in *Optomechatronic Micro/Nano Components, Devices, and Systems*, Philadelphia, Pennsylvania, Proc. SPIE, Vol. 5604, p.218-229 (October 2004).
2. W. Lee, N. A. Hall, Z. Zhou, and F. L. Degertekin, IEEE J. Quantum Electron. **10**, 3 (2004).
3. P. G. Datskos, N. V. Lavrik, and S. Rajic, Rev. Sci. Instrum. **75**, 4 (2004).
4. S. Timoshenko, J. Opt. Soc. Am. **11**, 233 (1925).
5. G. P. Nikishkov, J. Appl. Phys. **94(8)**, 5333-5336 (2003).
6. H. Torun, H. Urey, F. DeWitt, submitted to J. Appl. Phys.
7. H. Urey, Retinal Scanning Displays, in *Encyclopedia of Optical Engineering*, ed. R. Driggers (Dekker, Sept 2003), Vol. **3**, p.2445 - 2457.
8. S.-H. Lim, J. Choi, R Horowitz, and A. Majumdar, "Design and Fabrication of a Novel Bimorph Micro-Opto-Mechanical Sensor" Accepted for publication in the *Journal of Microelectromechanical Systems* (2005)
9. P.W. Kruse, “Uncooled Thermal Imaging, Arrays, Systems, and Applications” in *Tutorial Texts in Optical Engineering*, ed. A.R. Weeks, Jr., (SPIE, 2001), Vol.TT51
10. J. H. Lienhard IV, J. H. Lienhard V, “A Heat Transfer Textbook”, p.536, Third Edition, Phlogiston Press, 2005
11. F. P. Incropera, D.P. DeWitt, “Fundamentals of Heat and Mass Transfer”, p.337 and p.539, Fifth Edition, John Wiley and Sons, 2002
12. F. P. Incropera, D.P. DeWitt, “Fundamentals of Heat and Mass Transfer”, p.917, Fifth Edition, John Wiley and Sons, 2002
13. http://www.electronics-cooling.com/html/2002_november_techdata.html
14. J. H. Lienhard IV, J. H. Lienhard V, “A Heat Transfer Textbook”, p.145, Third Edition, Phlogiston Press, 2005

Chapter 5

OPTICAL READOUT DESIGN AND TESTING

5.1 Introduction

The deflection of the cantilever like micro-structures is determined by optical methods. For that purpose, pixel level micro-interferometers with diffraction gratings, which serve as reference reflectors, are designed. Under each membrane of the pixels there are diffraction gratings, through which the membranes are illuminated by coherent light as illustrated for a generic pixel in Fig.5.1. The reflected light from the gratings and the membranes create interference pattern on the observer plane with intensity I_{out}. The gap between the membranes and the gratings, denoted by d is modulated by the absorbed IR radiation incident on the membranes due to the thermal deformation on bimaterial legs. On the other hand, the displacement of the membranes modulates the output intensity on the observer plane. Therefore the thermal distribution of the target on which the focal plane array is looking can easily be mapped to the intensity of the readout light reflected from the pixels.

The same readout method, which offers atomic level displacement measurement, has been implemented successfully before for measuring the deflection of the membranes of capacitive micromachined transducers (CMUT)[1,2,3]. It was experimentally shown that the minimum detectable displacement[4] is 2.08×10^{-4} A/$\sqrt{}$Hz at 20 kHz.

In the remainder of this chapter diffraction-grating interferometer theory, pixel optical readout, optical array readout architectures, the effect of the readout on the system NETD, and finally optical readout test results using other similar devices are discussed.

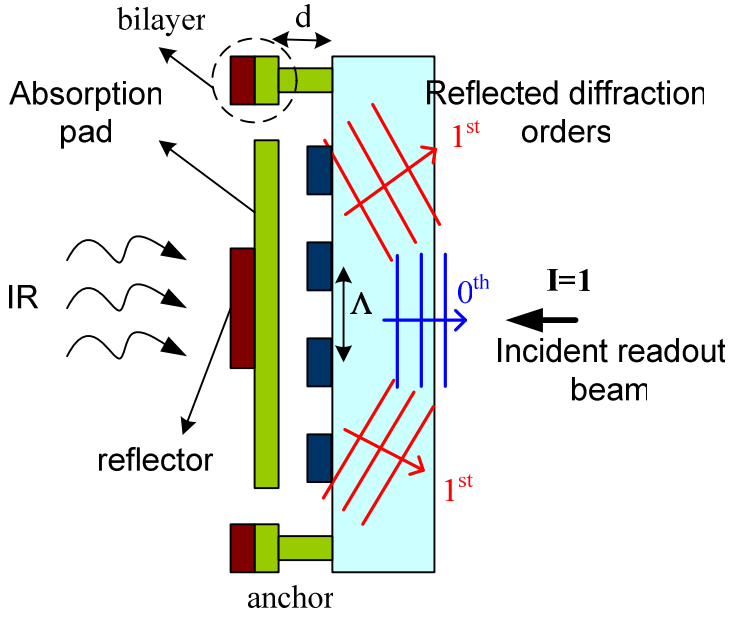

Fig.5.1 Schematics of the micro-interferometer with diffraction grating for readout optics

5.2 Diffraction-Grating Interferometer Pixel Readout

5.2.1 Diffraction-grating – Interferometer Theory

For the analysis of the intensity of the light at the observer plane, the problem can be simplified by separately computing the components of the light at observer plane. Instead of computing the amplitude of the output light reflected from the pixel of the detector, equivalent problem deals with a unity intensity light transmitted through a diffraction grating that models the light reflected directly from the diffraction grating; together with a unity intensity light propagated in free space having an optical path difference (OPD) of δ with the former one that models the light reflected from the reflector and absorption pad as labeled in Fig.5.1. The resultant amplitude of the output light is the sum of the amplitudes of each component.

The problem of diffraction by many slits is a well-known one and the output optical disturbance is given as follows[5], assuming half of the amplitude of light is incident on the grating.

$$E_{out,1} \propto \frac{\sin(\beta)}{\beta} \cdot \frac{\sin(2N\beta)}{\sin(2\beta)} \cdot \sin(\omega t - kR + 2(N-1)\beta)$$

$$\beta = \frac{\pi}{4\lambda} \Lambda \sin(\theta) \tag{5.1}$$

where Λ is the period of the diffraction gratings with N fingers having a duty cycle of 50%, θ is the diffraction angle at which the output wave propagates and R is the distance from the diffraction grating to the observer plane along the output wave. From the optical disturbance, the output intensity can be given as:

$$I_{out,1} = \frac{I_{in}}{4N^2} \left(\frac{\sin(\beta)}{\beta} \right)^2 \cdot \left(\frac{\sin(2N\beta)}{\sin(2\beta)} \right)^2 \tag{5.2}$$

For the computation of second component of the amplitude and intensity of light at the observer plane, the OPD should be taken into account. The detailed illustration for the OPD is given in Fig.5.2. From that figure, the total OPD is divided into two components as δ_1 and δ_2. From basic geometry, the OPD components are given in Eq.5.3. As a result of the resultant optical path difference; phase shift, which is given in Eq.5.4, is created between the portion of light directly reflected from the gratings and the other portion of light reflected from the membrane.

$$\delta_1 = d \ , \qquad \delta_2 = d\cos(\theta) + \frac{\Lambda}{4}\sin(\theta) \tag{5.3}$$

$$\Omega = \frac{2\pi}{\lambda}(\delta_1 + \delta_2) \tag{5.4}$$

The resultant optical disturbance at the observer plane can be written as follows, where u is the amplitude of the disturbance due to the portion of light directly reflected from the grating as given in Eq.5.1.

$$E_{out} = u\left[1 + \exp\left(-j\frac{2\pi}{\lambda}(\delta_1 + \delta_2)\right)\right] \tag{5.5}$$

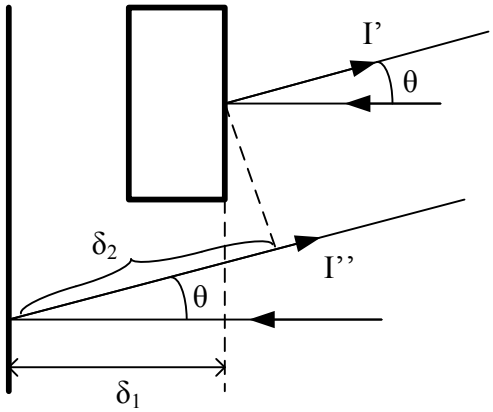

Fig.5.2 Detailed view for the OPD calculation

From the optical disturbance given above the resultant intensity at the observer plane can be found as follows:

$$I_{out} = 2|u|^2\left[1 + \cos\left(\frac{2\pi}{\lambda}(\delta_1 + \delta_2)\right)\right] = 4|u|^2\left[\cos\left(\frac{\pi}{\lambda}(\delta_1 + \delta_2)\right)\right]^2 \tag{5.6}$$

where $|u|^2 = uu^*$ is the output intensity given in Eq.5.2 due to the transmitted light through the diffraction grating. Combining Eq.5.2 and Eq.5.6, the overall intensity is given in Eq.5.7.

$$I_{out} = \frac{I_{in}}{N^2}\left(\frac{\sin(\beta)}{\beta}\right)^2 \cdot \left(\frac{\sin(2N\beta)}{\sin(2\beta)}\right)^2 \left[\cos\left(\frac{\pi}{\lambda}(\delta_1 + \delta_2)\right)\right]^2 \tag{5.7}$$

Finally the diffraction angle θ, along which the reflected beam from the pixels propagates, can be given as follows[5]:

$$\Lambda \sin(\theta_m) = m\lambda, \qquad m = \pm 1, \pm 2, \pm 3, \ldots \tag{5.8}$$

where m is the diffraction order. Eq.5.7 together with Eq.5.8 is very important in the sense that they quantitatively specify how the intensity at an order at the observer plane is modulated as a function of gap, d between the membrane and the diffraction gratings. It is shown in Fig.5.3 that all of the optical power falls in the 0^{th} order when the gap is the half wavelength. Theoretically, the power fell on 0^{th} order vanishes when the gap is the quarter of the wavelength, and the power is shared when the gap is λ/8. By measuring 0^{th}, or $\pm 1^{st}$, or both orders; one can specifies how much the membrane displaces. Therefore, the intensity fell on these orders are important and are given explicitly as follows:

$$I^0 = I_{in}\left(\cos\left(\frac{2\pi d}{\lambda}\right)\right)^2, \qquad I^{\pm 1} = \frac{4}{\pi^2} I_{in}\left(\sin\left(\frac{2\pi d}{\lambda}\right)\right)^2 \tag{5.9}$$

Based on the expressions given above, the intensities of light going to 0^{th} and 1^{st} diffraction orders are plotted as a function of ratio of the gap to the wavelength, which is an unitless expression as seen in Fig.5.4.

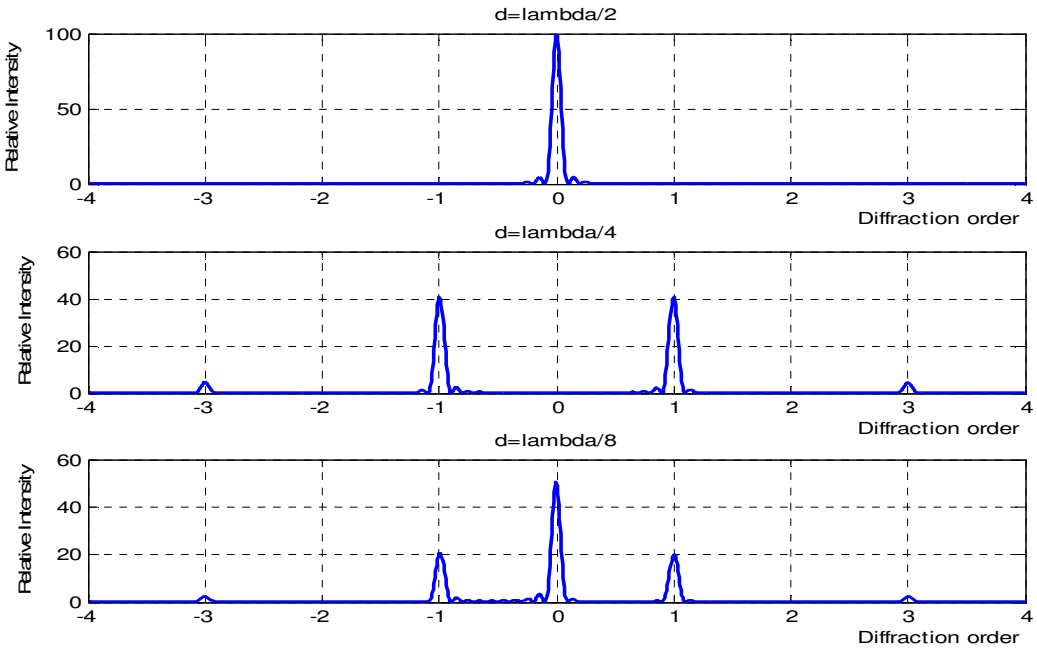

Fig.5.3 Modulation of output intensity with the distance from the membranes to the diffraction gratings with 10 periods of diffraction gratings

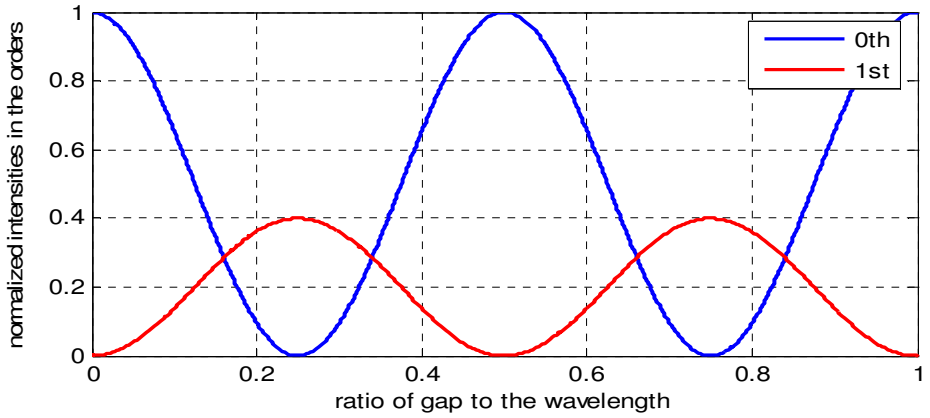

Fig.5.4 Intensity of light going to diffraction orders as a function of the distance from the membranes to the diffraction gratings

5.2.2 Micro – Interferometer Design for Membranes with Piston Motion

The pixel overview of the detector design is shown in Fig.5.1 where the membrane is hanged from the mid portions by the cantilever like structures. Due to the symmetry in the design the membrane motion is parallel to the substrate on which there are the fingers of diffraction gratings. As the membrane moves up and down relative to the gratings as a result of absorbed IR radiation, the light intensity at the diffraction orders is modulated. For this design the period of diffraction gratings and the number of periods are selected as 4 μm and 4, respectively. The minimum size is limited by microfabrication. Assuming that the readout laser has a wavelength of 632 nm, the diffraction angle is approximately 0.158 rad in air from Eq.5.8. The refractive index of quartz substrate is 1.5 and taking that into account, the separation between orders in the substrate becomes 0.107 rad. The thickness of quartz substrate is 500 μm and the output intensity as the gap between the membrane and the diffraction grating changes is shown in Fig.5.5. Comparing Fig.5.4 with Fig.5.3, it can be clearly observed that the tails of the sinc function is more dominant as the number of diffraction grating period decreases.

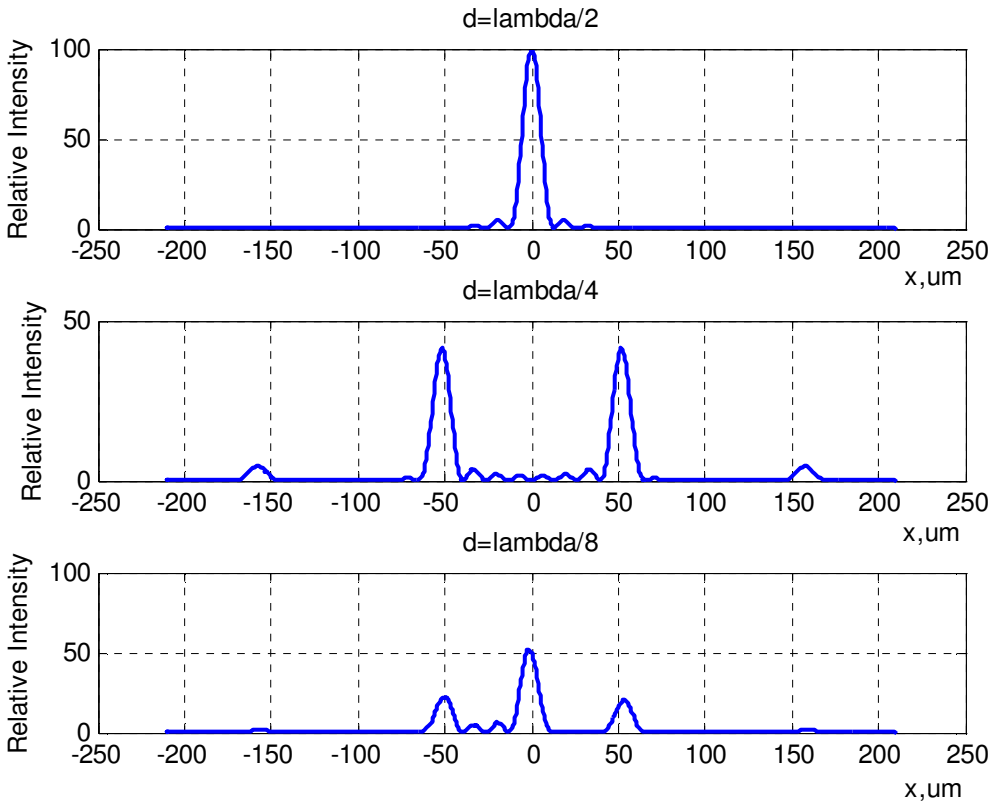

Fig.5.5 Modulation of output intensity at the observer plane with varying gap between the membranes and the diffraction gratings

5.3 Array Readout Architectures

The light from each pixel is deflected into diffraction orders. One can use a laser diode and a detector per pixel, which we call the optoelectronic readout. This can be accomplished by integrating a VCSEL array and a PIN photodiode array as discussed in 5.3.1. However, this architecture doesn't lend itself well into scaling to large array sizes. A better method is to use a single light source and use one or a few detectors to capture the light from all the pixels. This can be accomplished using a MEMS scanner that addresses each pixel in a raster

fashion. This scanned-beam array readout method, discussed in 5.3.2, is simpler and scalable up to SVGA resolution (800x600 pixels) detector array architectures.

5.3.1 Optoelectronic Readout

One of the architectures for measuring the output intensity at the diffraction orders is to illuminate each pixel with a vertical cavity surface emitting laser (VCSEL) and collect the light at orders with photo detectors. For the capacitive transducers, this architecture was implemented for both single transducers or an array of transducers[1,2,3,4].

The proposed pixelated readout optics for the designed thermal detectors is illustrated in Fig.5.6. In this architecture the pixels are illuminated by a VCSEL on a Ga-As chip from backside. The Ga-As chip is bonded to a Fused Silica one with a thickness of t3 on top of which there is a microlens to collect and collimate the beam emitted by the VCSEL. The Fused Silica chip is bonded to Silicon one on which there are through holes to let the beam pass through and the PIN diodes to collect the beam reflected from the detector pixels.

The spot size of the beam on the diffraction grating plane (s_{grat}) is set to 16 μm since the period of diffraction gratings is 4 μm and the total number illuminated periods is 4. Assuming that the microlens collimates the beam incident on itself, the thickness of Fused Silica wafer (t3) can be calculated from Eq.5.10. Here the emission area of the VCSEL is assumed to be 5 μm with a numerical aperture (NA) of 0.15.

$$t3 = \frac{s_{grat}\, n}{2NA} \tag{5.10}$$

where n is the refractive index of Fused Silica. The thickness t3 is calculated to be 80 μm. The focal length of the microlens should be equal to t3 so that the beam is collimated. Collimated beam, incident on the grating, is then reflected back. The reflected beam is diffracted in the orders and the separation angle between them is given in Eq.5.8. For the small angle approximation, the separation between the orders at the PIN diodes plane ($d_{seperation}$) is given in Eq.5.11. By placing PIN diodes with the given spacing, it is possible to measure the intensity of light at the diffraction orders -1, 0 and 1. The intensity of light at 0^{th} order can be collected partly by PIN diodes located adjacent to the through holes.

$$d_{seperation} = \frac{\lambda}{n\Lambda} t1 \tag{5.11}$$

For the VCSEL emitting light at 850 nm, the separation between orders can be calculated to be approximately 71 μm for 500 μm thick Quartz wafer. The given architecture requires one VCSEL per pixel and at least one PIN diode to capture the reflected light. For large FPA's such a configuration adds complexity and increases the power consumption due to large number of elements. Many pixels of the FPA can be illuminated with one light source using a diffractive optical fan-out grating as suggested in Fig.5.7.

In that case, a single laser diode can illuminate 1000 or more pixels; it is possible to illuminate even larger number of camera pixels with some sacrifices in the light source efficiency. For high-resolution thermal camera systems that have more than 100,000 pixels, two DOE-based illumination modules can be used in series to increase the number of diffraction orders. Using an array of light source-DOE modules where each module provides illumination to a set of pixels, allows a scalable architecture for higher resolution camera systems.

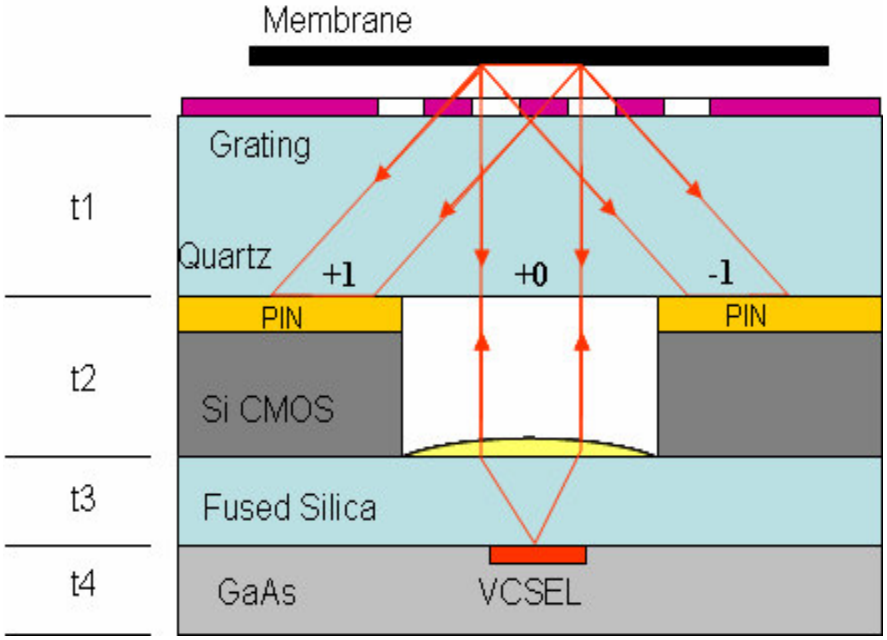

Fig.5.6 Pixelated optoelectronic readout architecture

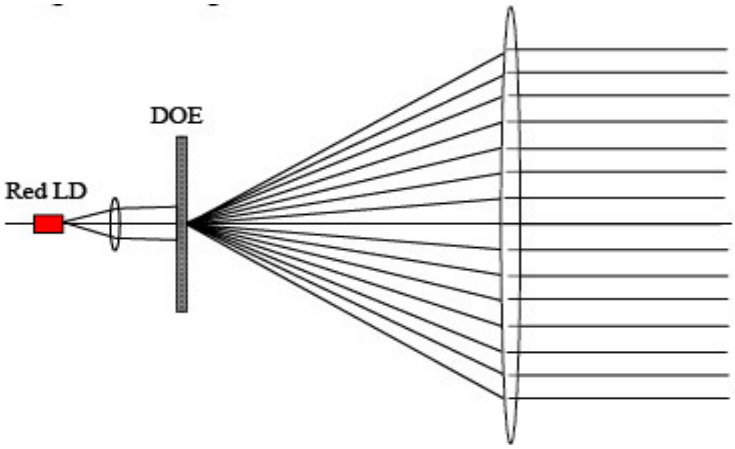

Fig.5.7 Configuration for the illumination of multiple pixels with a single light source

5.3.2 Scanned Beam Readout

With the given read – out configurations, the number of laser diodes can be either one for the whole FPA or one for each pixel, but in any case the number of photodiodes is at least one for each pixel. To reduce the number of photodiodes, even make it one for the whole FPA is possible with a use of scanner architecture. MEMS scanners are already quite well developed. As an example, the 2D MEMS scanner developed by Microvision Inc. is capable of producing a 2D raster at 60fps with SVGA (800x600) resolution and already used in commercial products[6,7].

In this configuration given in Fig.5.8, a 2D raster pattern is scanned at the detector plane by collecting the reflected light from the scanner with the focusing lens. The beam reflected from the pixels of the detector array is then collimated by the same lens. The Collimated beam is then focused onto PIN diodes located at diffraction orders by using other lenses.

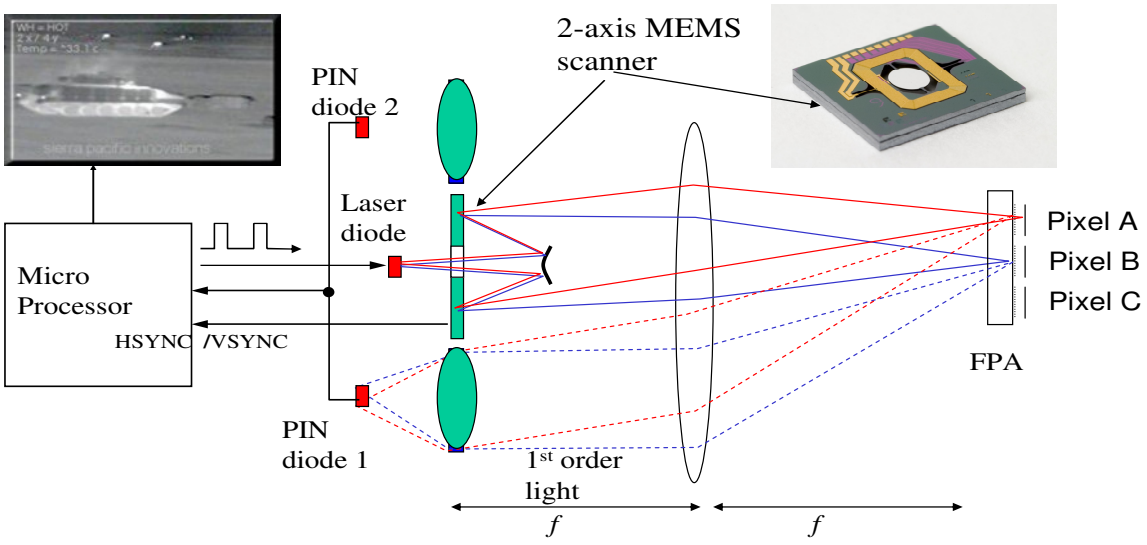

Fig.5.8 Scanned beam readout architectures

System architecture for retinal scanning display technology is presented in Ref. 8 and sticking to the definitions given there, the required speed for scanning a whole FPA (s_{FPA}) can be calculated as follows:

$$s_{FPA} = \frac{N_h N_v \Delta f}{K_d} \tag{5.12}$$

where N_v and N_h are the number of pixels in columns and rows of FPA, respectively. Δf is the measurement bandwidth of single detector and K_d is the pixel duty-cycle. Assuming 50% duty-cyle and K_{os}=0.8, s_{FPA} becomes ~37 Mps (mega-pixels per second). Therefore total time period allocated for a single pixel is 27 ns, which means that PD is read for about 9 ns, and 18 ns is the waiting time between pixels, and then next pixel can be readout similarly.

5.3 Noise Contribution of Optical Readout

From the intensity distribution at the diffraction orders given in Eq.5.9, the current generated on the PIN diodes can be calculated as follows:

$$i^0 = I_{in} AR\left(\cos\left(\frac{2\pi d}{\lambda}\right)\right)^2, \qquad i^{\pm 1} = \frac{4}{\pi^2} I_{in} AR\left(\sin\left(\frac{2\pi d}{\lambda}\right)\right)^2 \tag{5.13}$$

where R is the responsivity (in A/W) and A is the effective area of the diodes. The maximum sensitive point for the diodes can be calculated by equating the second derivative of the PIN currents with respect to the value of the distance between the membrane and the diffraction gratings to zero. For both orders, the maximum sensitive point can be achieved when $d = m\lambda/8$ where m=1,3,5,… as apparent from Eq.5.14

$$\frac{\partial^2 i^0}{\partial d^2} = -\frac{8\pi^2}{\lambda^2} I_{in} AR\cos\left(\frac{4\pi d}{\lambda}\right), \qquad \frac{\partial^2 i^{\pm 1}}{\partial d^2} = \frac{32}{\lambda^2} I_{in} AR\cos\left(\frac{4\pi d}{\lambda}\right) \tag{5.14}$$

At the maximum sensitive point the sensitivity of the PIN diodes is given as follows:

$$S_o : \frac{\partial i^0}{\partial d} = \frac{2\pi}{\lambda} I_{in}\, AR\ , \qquad S_1 : \frac{\partial i^{\pm 1}}{\partial d} = \frac{8}{\pi\lambda} I_{in}\, AR \tag{5.15}$$

The minimum detectable displacement MDD can be defined as the ratio of the noise current on the diodes to the sensitivity given above. Assuming shot noise limited detection, the noise current is given as $i_N = \sqrt{2\,q\,P_{in}\,R}\ (A/\sqrt{Hz})$, q=1.6×10^{-19} C, where P_{in} ($P_{in} = AI_{in}$) is the power incident on the diodes. Therefore MDD can be calculated as:

$$MDD_0 = \frac{i_N}{S_0} = \frac{\sqrt{2\,qP_{in}R}}{\frac{2\pi}{\lambda} P_{in}\,R} = \frac{\lambda}{\pi}\sqrt{\frac{q}{2P_{in}\,R}}\ , \qquad MDD_1 = \frac{i_N}{S_1} = \frac{\sqrt{2\,qP_{in}R}}{\frac{8}{\pi\lambda} P_{in}\,R} = \frac{\pi\lambda}{4}\sqrt{\frac{q}{2P_{in}\,R}} \tag{5.16}$$

With R = 0.6 (A/W), λ = 850nm, and P_{in} = 150 μW, the values of MDD_0 and MDD_1 can be calculated numerically as $\approx 8\cdot 10^{-15}\, m/\sqrt{Hz}$ and $\approx 2\cdot 10^{-14}\, m/\sqrt{Hz}$, respectively. These noise parameters can be mapped to NETD due to readout optics ($NETD_{ro}$) with following equation:

$$NETD_{ro} = \frac{MDD}{\Delta T_D / \Delta T_S}\Delta f \tag{5.17}$$

where Δf is the bandwidth of the readout electronics and $\Delta T_D / \Delta T_S$ is the temperature response of the thermal detector, which is defined as the amount of temperature difference on the detector pixels per unity temperature difference on the target[9].

$$\Delta T_D / \Delta T_S = \frac{1}{G} \frac{\eta \cdot \tau_0 \cdot \beta \cdot A \cdot (dP/dT)_{\lambda 1 - \lambda 2}}{4 f_{no}{}^2} \tag{5.18}$$

Together with the performance parameters of the detector given in Chapter 4, $NETD_{ro}$ can be calculated as 0.98 mK and 2.42 mK for 0^{th} and 1^{st} order PIN diodes, respectively. Combining the readout noise together with the mechanical noise presented in Chapter 4, the overall NETD of the design becomes 7.9 mK.

5.4 Testing of Micro – Interferometer with CMUTs

The pixelated readout architecture was first implemented for the capacitive transducers that were designed and fabricated at Georgia Institute of Technology, Atlanta. Since this architecture is the same as our proposed readout for the thermal detectors, we obtained some samples and performed some test and characterization experiments using the capacitive transducers with optical readout. The tests increased our understanding of the optical readout architecture and helped with out modeling efforts.

For the tests, a sensor with a circular membrane, which is anchored to the quartz substrate 2 μm below itself with a radius of 160 μm, is used. The membranes of the transducers can be actuated by applying a voltage difference between the electrodes attached to the membranes and the gratings on the substrate. For that configuration, the transducers can be modeled as parallel plate capacitors, assuming that the gratings act as a planar

electrode. Therefore, the net force on the membrane can be written as follows for a voltage difference of ϑ applied between the electrodes:

$$F_{net} = k(d_0 - d) - \frac{\varepsilon_0 A \vartheta^2}{2d^2} \tag{5.19}$$

Where k is the spring constant, d_0 is the initial gap between gratings and the membrane, ε_0 is the permittivity of air, and A is the area of the membrane. As seen from Eq.5.18 the dependence of the membrane displacement to the applied voltage is nonlinear. In order to map the voltage to the displacement, the setup given in Fig.5.9 is built. The backside of the transducer is illuminated by using a HeNe laser (λ = 632 nm) and the reflected light at 0^{th} order is detected. In order to collect 0^{th} order of the reflected beam, the transducer is slightly (<10°) rotated.

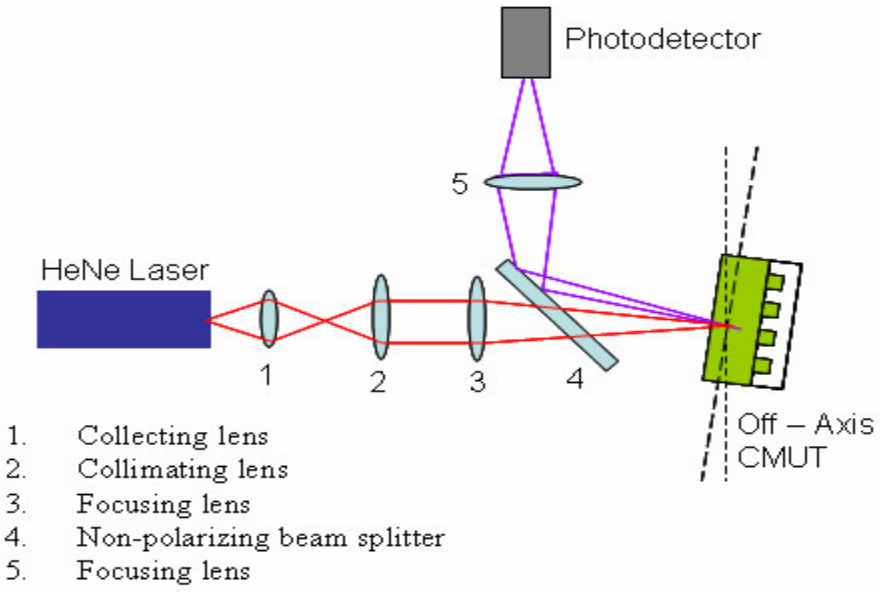

Fig.5.9 The schematics of the setup for characterization

The experimental result is given in Fig.5.10 with the label “experimental, 0^{th} order”, where the photodetector (PD) output is normalized to its maximum in order to get rid of DC bias present at the PD output due to the sum of ambient light and the reflected light from the stationary parts of the transducer. Thereafter it can be said that the PD output vanishes at around 30 VDC. According to Fig.5.5, the membrane height from the substrate should be quarter wavelength. From Eq.5.13, the behavior of the membrane displacement can be modeled and the PD output as a function of excitation voltage is plotted in Fig.5.10 where the spring constant is ~220 N/m. The model fits to the experimental data well when the excitation voltage is larger than 30 VDC. For smaller voltages the experimental data is ~30% larger than that of the model, which is an anticipated result since the membrane displaces with very small amplitudes for lower voltages due to nonlinear behavior. The smaller amplitudes cannot be measured precisely with the given setup in which bulky optical elements are used. As seen in Fig.5.10, the power of the reflected light at 1^{st} diffraction order, which is normalized to its maximum, is also estimated by using the model and the normalized. Finally the deflection vs. excitation voltage plot is given in Fig.5.11 by using the model developed from the experimental data.

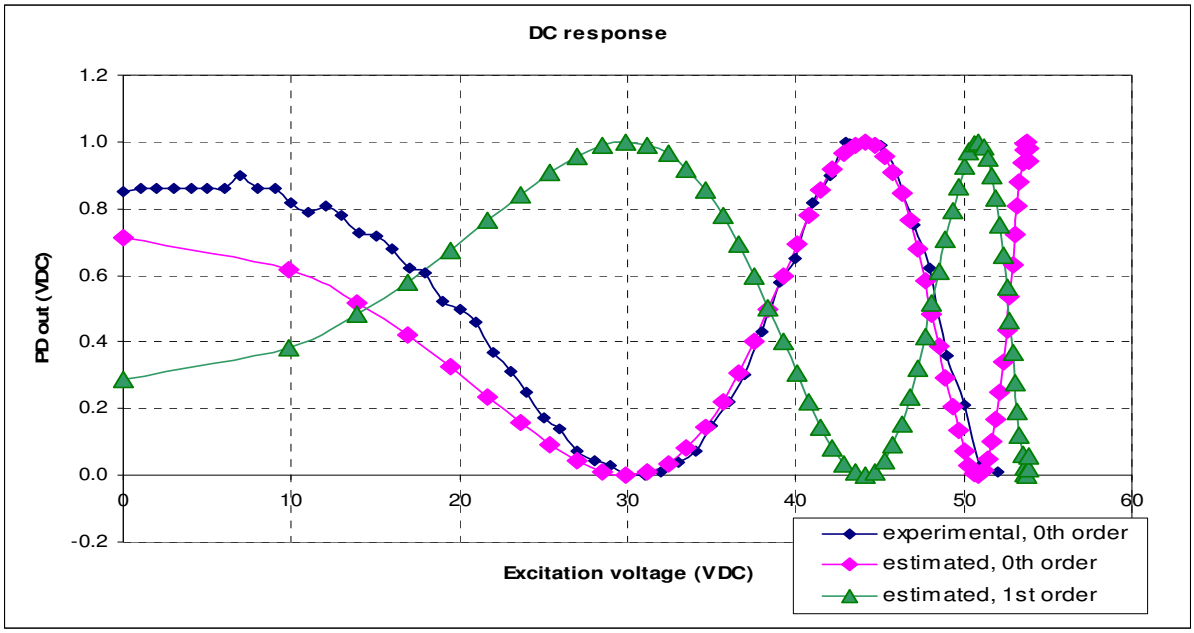

Fig.5.10 The photodetector response as the membrane of the sensor displaces due to the excitation voltage

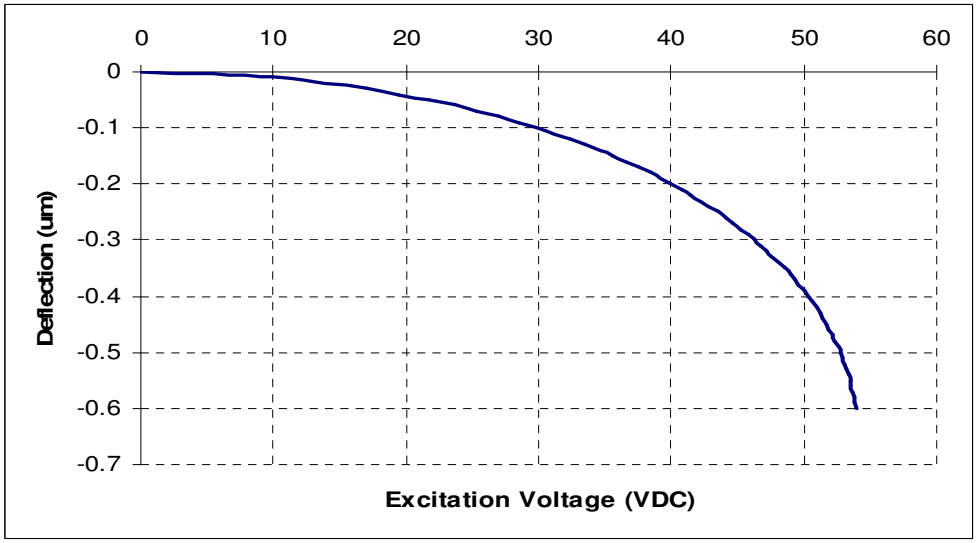

Fig.5.11 The deflection of the transducer membrane as a function of excitation voltage

After DC characterization of the transducers, the excitation voltage is changed to a sinusoidal one on top of a DC bias. DC bias is required to pull the membranes to a point so that the sensitivity of the membranes as a function of applied voltage is increased. By sweeping the frequency of the sinusoidal signal, the frequency response can be obtained. The experimentally derived frequency response is given in Fig.5.12. Then the nonlinear model is linearized around the DC point for which the excitation voltage is 40 VDC. The bode plot of the linearized model, which is in good agreement with the experimental frequency response is given in Fig.5.13. Here the output parameter is selected as the ratio of the displacement to the applied DC voltage.

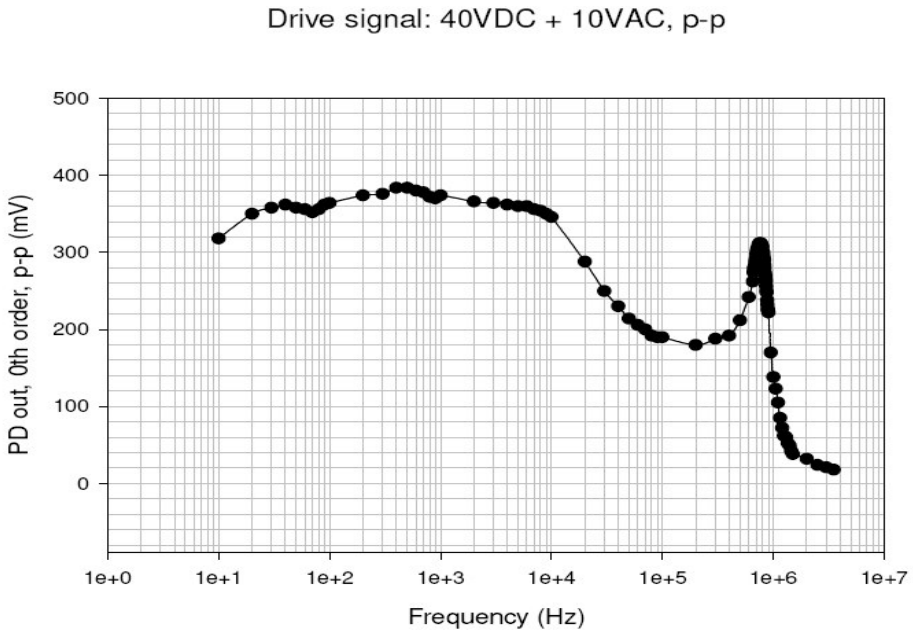

Fig.5.12 Frequency response of the membranes found experimentally

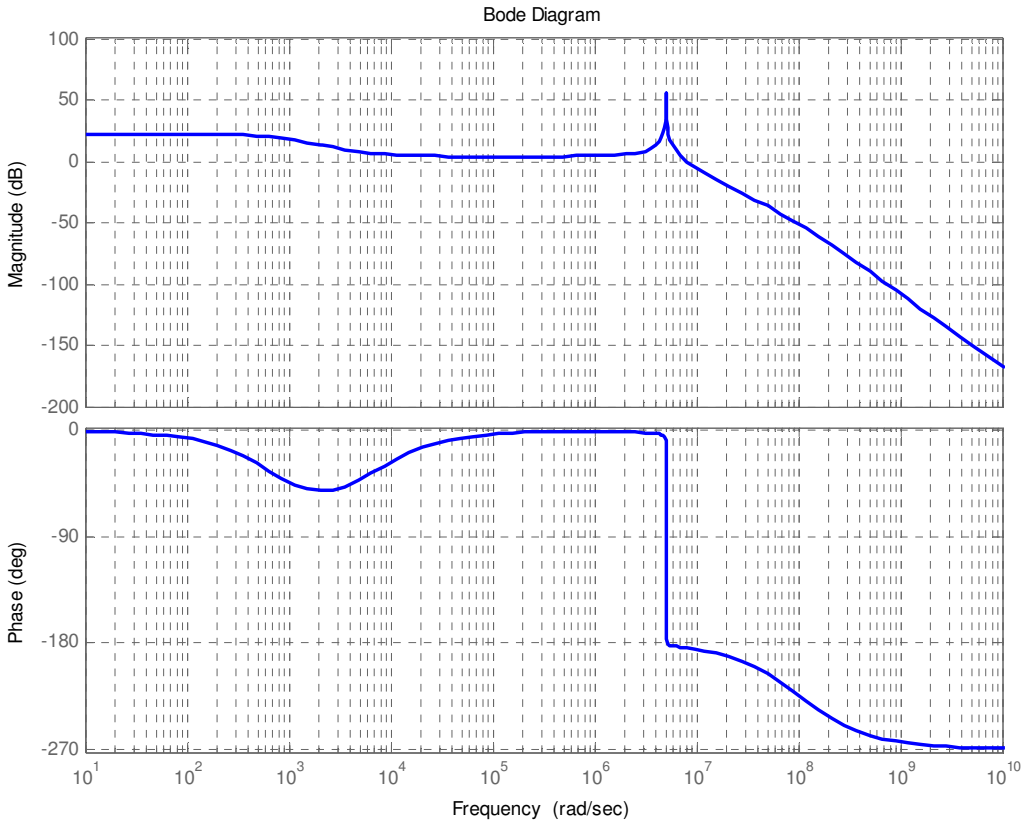

Fig.5.13 Frequency response of the membrane after linearization at the excitation voltage of 40 VDC

The tests performed with the given characterization setup shows that the theoretical results developed for the interferometer readout is in good agreement with the experimental results. Moreover, it is also possible to characterize the mechanical structures by the help of diffraction – grating interferometer as Fig.5.12 and Fig.5.13 suggests.

References:

1. N. Hall, F. L. Degertekin, "An Integrated Optical Detection Method for Capacitive Micromachined Ultrasonic Transducers", 2000 IEEE Ultrasonics Symposium
2. F. L. Degertekin, N. A. Hall, W. Lee, "Capacitive Micromachined Ultrasonic Transducers with Integrated Optoelectronic Readout", 2001 IEEE Ultrasonics Symposium
3. N. A. Hall, W. Lee, F. L. Degertekin, "Capacitive Micromachined Ultrasonic Transducers with Diffraction – Based Integrated Optical Displacement Detection", IEEE Transactions on Ultrasonics, Ferroelectrics and Frequency Control, Vol.50, No.11, November 2003
4. W. Lee, N. A. Hall, Z. Zhou, F. L. Degertekin, "Fabrication and Characterization of a Micromachined Acoustic Sensor With Integrated Optical Readout", IEEE Journal of Selected Topics in Quantum Electronics, Vol. 10, No. 3, May/June 2004
5. E. Hecht, "Optics", Addison Wesley, 4th ed, 2002, p.460-p.464
6. http://www.mvis.com/
7. Hakan Urey, "MEMS Scanners for Display and Imaging (Invited paper)," IEEE-LEOS Optical MEMS Conference 2005, Finland, August 2005
8. H. Urey, "Retinal Scanning Displays", Encyclopedia of Optical Engineering, Marcel Dekker, Inc., 2003, p.2445-p.2457
9. Yang Zhao, "Optomechanical Uncooled Infrared Imaging System", Dissertation for the Degree of Doctor of Philosophy, University of California, Berkeley, Fall 2002.

Chapter 6

MICROFABRICATION OF TEST DETECTORS AND TESTING

6.1 Introduction

In this chapter the developed fabrication steps are detailed for the design prototypes fabricated at Microelectronics Research Center, Georgia Institute of Technology, Atlanta, USA. As explained in the previous chapters; smaller the design features, better the performance. On the other hand, due to the process limitations, the photolithography masks were designed such that the minimum line width is 2 μm. In that sense the performance is mainly limited by the microfabrication. A 4-mask process was developed with standard materials that are commonly used in the semiconductor industry. Pyrex and Quartz wafers, which provide transparent media for the readout optics, were used in the batches. Chromium, Aluminum and Gold layers were deposited as metal layers by using DC Sputterer and filament evaporator. Silicon dioxide and silicon nitride layers that are deposited using Plasma Enhanced Chemical Vapor Deposition (PECVD) machine at 250 °C were the dielectric layers. Reactive Ion Etching (RIE) machine together with wet etching techniques were used to pattern the layers.

6.2 Process Flow

6.2.1. Cleaning Wafers

Cleaning step is necessary before starting the processing steps for each batch. For both pyrex and quartz wafers, cleaning was performed by using acetone and methanol.

6.2.2. Lift-off

Lift-off step is divided into three sub-steps as follows: Photoresist spinning, photolithography, metal deposition and patterning.

6.2.2.1 Photoresist Spinning

For the success of lift-off process, the PR should be as thick as possible compared to the thickness of metal layer. Photoresist SC1813 was used to give the desired profile.

6.2.2.2. Photolithography

Photolithography for each processing steps was performed by using Karl Suss™ MA-6 Mask Aligner. The exposed wafers were then developed by PR developer "MF319". The exposure time was first calculated theoretically using the sensitivity data for SC 1813 given by Shipley™. Then the correct exposure time was found experimentally by varying the calculated exposure time.

The successful results for the lift off process can be obtained if the PR is soft. Therefore, the wafers were not prebaked after development.

6.2.2.3. Metal Deposition and Patterning

The metal deposition for the lift – off process was performed with Kurt J. Lesker™ PVD-75 Filament Evaporator. The first batches were started with Pyrex wafers, however after few attempts Pyrex wafers were replaced by Quartz ones. The main problem observed during

photolithography was the low adhesion between the wafers and PR. As the wafers were developed, the PR layer tended to be stripped off.

Even if the photolithography step was accomplished successfully with the Pyrex wafers, the metallization step failed as a result of adhesion problem between metal and the layer. Initially the material for the gratings was selected as Al, but due to low adhesion, some Cr layer was used as an adhesion layer. Even though the results improved by the help of adhesion layer, the yield was very low. The stiction problem is apparent in Fig.6.1 which shows a portion of a Pyrex wafer after the lift-off.

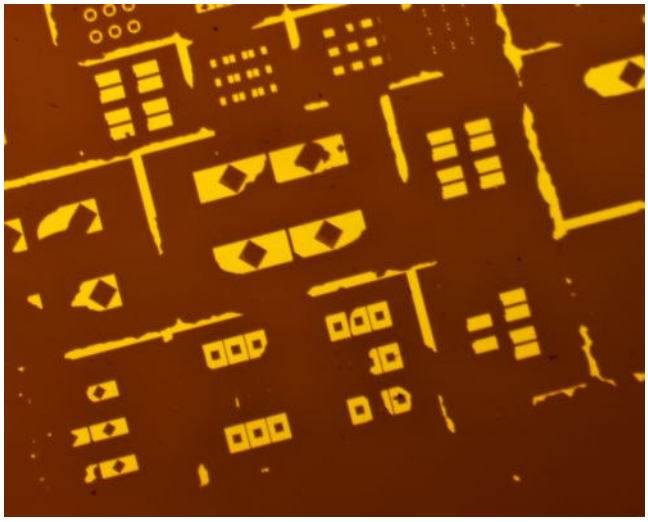

Fig.6.1 General View of Pyrex wafer after lift-off process

After a few unsuccessful attempts with Pyrex wafers, wet etching was tried to define the gratings. Since the mask was designed for the lift – off process, negative photoresist was needed. First Chromium, then Aluminum blanket layers was deposited on top of Pyrex wafers. After the deposition, the metal layers were patterned by proper wet etchants.

As seen from Fig.6.2, the adhesion between the wafer and the metal layer is good in this case; although the resolution is not good enough to have operational diffraction gratings. That problem could not be solved and as a result of this, Pyrex wafers were replaced by the Quartz ones as explained before.

Even with quartz wafers, development step should be carried out with extra care to prevent PR from peeling off the wafer. After metallization, the wafers were put in a dish full of acetone to lift the PR layer together with the metal on top of it. The lift – off step was completed by using the ultrasonic cleaner. Successfully defined gratings on top of Quartz wafers can be seen in Fig.6.3.

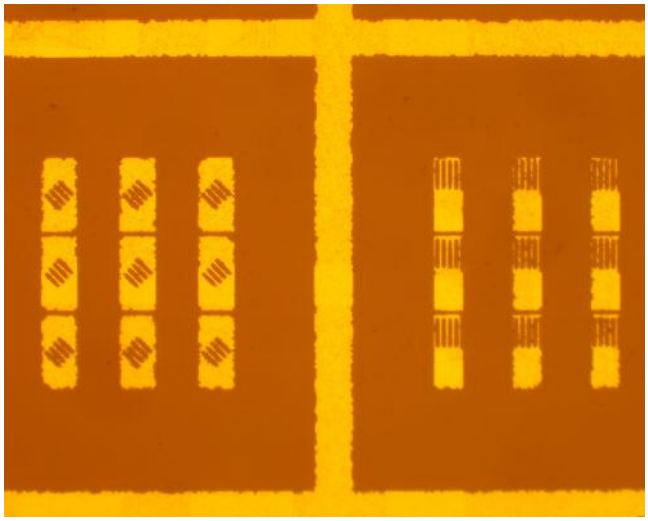

Fig.6.2 Grating definition on top of Pyrex wafer by wet etching techniques with negative photoresist

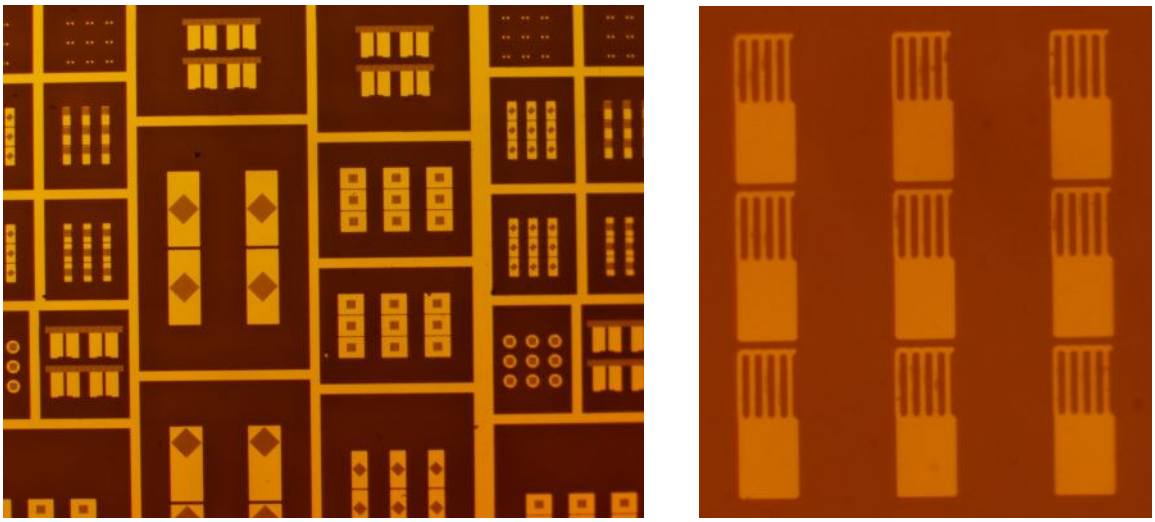

(a) (b)

Fig.6.3 (a) General view of defined gratings on top of Quartz wafer by lift-off. (b) Detailed view of gratings from one specific device

6.2.3. Deposition of SiO_2 layer to protect gratings

The best candidate for the sacrificial layer was Chromium. That is due to the easiness of removing Cr layer by wet etchants and good adhesive properties of Cr layer. On the other hand, one problem for deposition of thick Cr layer is the high stress inherent to the Cr layer. After depositing thick Cr layers (> 2 μm) on top of test wafers, it was observed that the wafers were buckled slightly even though the buckling was not quantitatively measured.

In order to use Cr as a sacrificial layer, it was needed to protect the gratings during the etching phase to release the devices. As a result, SiO_2 layer was deposited on top of gratings to protect them. Apart from that, the dielectric layer served also as a protection layer from the collapse and permanent stiction of the membranes to the gratings.

6.2.4. Deposition and Patterning of Cr Sacrificial layer

After the deposition of Cr sacrificial layer, photolithography was needed to define the anchors. By experimentally finding the optimum exposure time, the steps given in 6.2.2.2 were followed. Then the Cr layer was patterned with Cr etchant and after patterning the openings for anchors, the PR on top of the wafers were removed with acetone. In order to completely remove the PR, the wafers were cleaned using RIE by O_2 plasma. The patterned anchors can be seen in Fig.6.4.

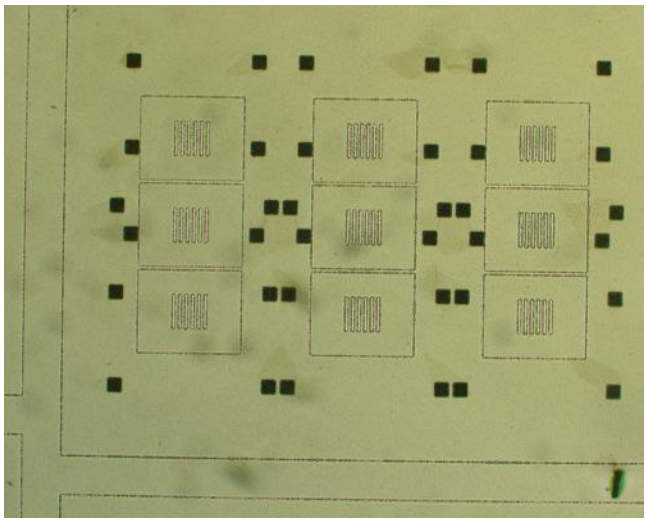

Fig.6.4 Anchor definition on Cr sacrificial layer

6.2.5. SiN_x Deposition:

Silicon nitride is the material choice for the absorption pads and bimaterial legs as explained in earlier chapters. 0.5 μm SiN_x was deposited at 250 °C

6.2.6. Al Layer Deposition and Patterning:

After the blanket deposition of Al layer, photolithography was needed to define the bimaterial legs. No problems regarding to adhesion were faced for the deposition of Al layer on top of the nitride layer. The deposition was performed with CVC^{TM} DC Sputterer. After photolithography, the bimaterial legs were defined by using the aluminum etchants. The patterned metal layer can be seen in Fig.6.5.

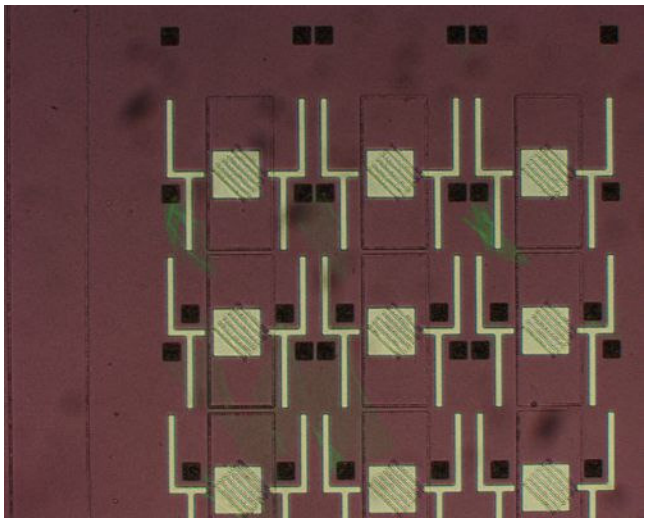

Fig.6.5 Aluminum layer patterned for bimaterial legs

Apart from Al, Au is also deposited and patterned as the metal layer in bimaterial legs as a design variation, and Fig.6.6 shows the patterned gold layer for the bimaterial legs.

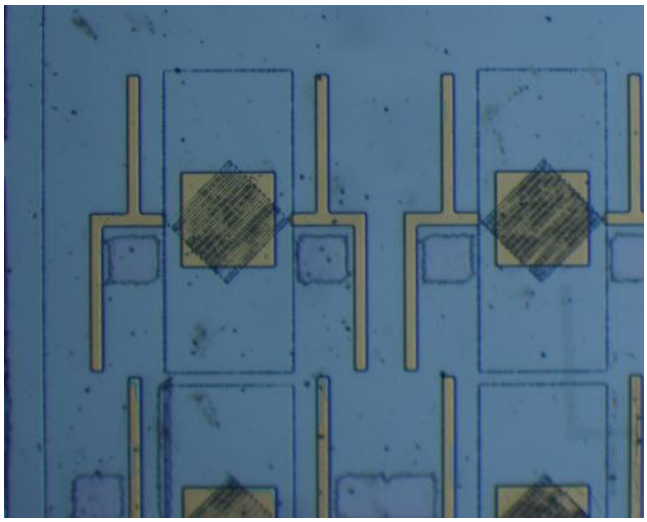

Fig.6.6 Definition of bimaterial legs made of Gold and Silicon Nitride

6.2.7. Patterning SiN_x Layer:

PlasmaTherm™ RIE machine was used to etch the nitride layer in order to define the isolation legs and absorption pads. Since the recipe for RIE attacks PR, SC 1813 was replaced by SC 1827 that gives thicker profile. Different devices can be seen in Fig.6.7 after this step.

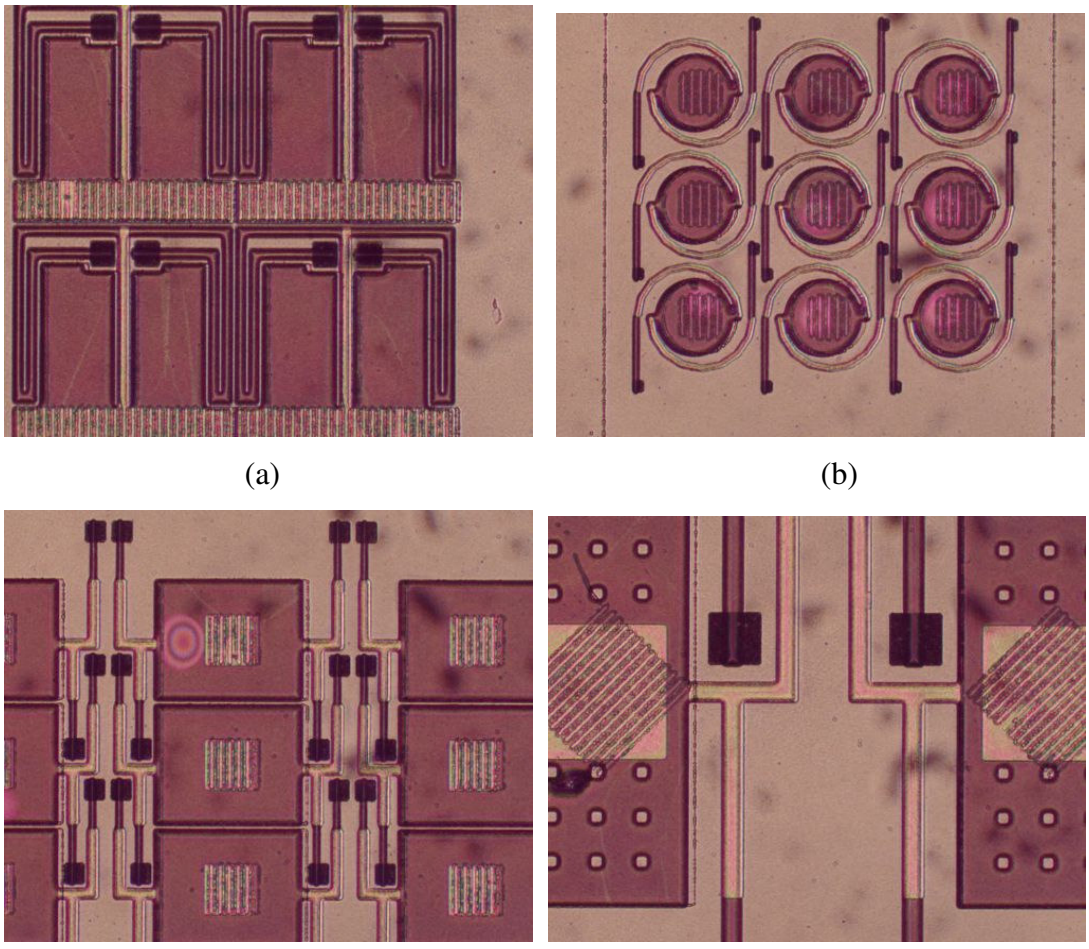

(a) (b)

(c) (d)

Fig.6.7 The devices on top of sacrificial layer after the RIE step

6.2.8. Dicing:

The wafers were taken outside the cleanroom for the dicing and then the releasing steps. The wafers were coated with PR to protect the features on top of the sacrificial layer. The dies were designed such that each one is a 1.5 cm x 1.5 cm square as seen from the mask

layouts given in the appendices. In order to have a good edge profile after the dicing, the intersection regions between the dies were left as metal coated quartz wafer.

6.2.9. Releasing the Dies:

The releasing of the devices started with the removal of protective photoresist layer with acetone. After the removal of photoresist, it was needed to etch the Cr sacrificial layer. The etching step should not attack the Aluminum and the nitride layer. For that reason, a highly selective Cr (Cyantek^{TM} Cr-14S) etchant was planned to be used. Since the etchant was not available immediately, the ingredients of the etchant were added together.

6.3 Packaging Requirements

The first requirement for the package is to provide a vacuum environment to the devices so that the thermal conductance of air between the membranes and the substrate is negligible. The relationship between the conductivity of air and the environment pressure level is given in Ref.6.1. The thermal conductance due to air through conduction can be decreased below 10 nW/K as described in Chapter 4.4.4 at a pressure of 1mTorr, which requires a vacuum sealed package.

The second requirement for the package is to provide thermal stabilization between the environment and the focal plane array. Thermoelectric coolers (TEC) from Marlow^{TM} are used to stabilize the arrays at the room temperature by a closed loop controller. For the closed loop system, temperature sensor IC's (LM335, National Semiconductor^{TM}) are used to sense the temperature of the detector array. Fig.6.8 shows a conceptual drawing of the package, where TEC and the temperature sensor are placed on the edges of the detector

array, which is attached to the case of the package through the heat sink required to cool the hot side of TEC.

The control algorithm of the temperature controller LDC3724B from ILX Lightwave™ offers a hybrid PI one that is capable of regulating the temperature of the FPA with the temperature measurement noise due to the feedback sensor LM335. Temperature error for the sensor is given[2] as 0.5 °C. To further improve the temperature stability, feedback control loops with Kalman filters were demonstrated[3] in the literature to regulate the FPA temperature with a standard deviation less than 100 μK.

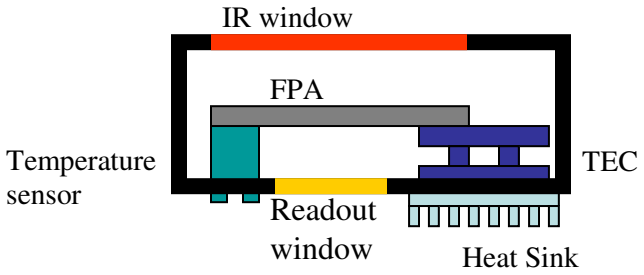

Fig.6.8. The devices on top of sacrificial layer after RIE step

References:

1. http://www.electronics-cooling.com/html/2002_november_techdata.html
2. National Semiconductor, LM135/LM235/LM335, LM135A/LM235A/LM335A Precision Temperature Sensors Datasheet, Feb. 1995
3. J. Choi, et. al., "Design and Control of a Thermal Stabilizing System for a MEMS Optomechanical Uncooled Infrared Imaging Camera", Sensors and Actuators A 104 (2003) 132 – 142

Chapter 7

CONCLUSIONS

In this research, a novel thermo – mechanical type uncooled thermal detector array with optical readout is designed and fabricated. The primary aim of the device is to generate a thermal map of targets based on the absorbed infrared radiation in LWIR band. The mechanical structure of the detector array is pixelated to allow for large format FPAs for imaging applications. The NETD of our optimized system including the readout optics is about 8 mK and mainly limited by the thermal fluctuation noise. The assumptions are 50μm pixels, 60fps, and f/1 optics. This performance level is far superior to the other current state-of-the-art uncooled detector arrays and is comparable to that of the best cooled IR detector arrays. In addition to high-performance, the architecture proposed is scalable to high-resolutions as the pixel readout is based on integrated diffraction gratings and the readout electronics is completely eliminated by the use of scanned beam readout.

The design phase of the research focused on the design and optimization of pixel structures that form the FPA. The main design effort has three important parts where significant contributions were made: (i) IR absorber design, (ii) thermo – mechanical deflection analysis, and (iii) optical readout design. .

(i) IR Absorber Design: For the IR absorber design, a multilayer IR absorption analysis method is presented. Using the analytical model, the theoretical IR absorption structure is designed. The optimization is focused on maximizing the absorption in LWIR band by selecting suitable materials and engineering the geometrical properties of the absorber. Among the different possible absorber structures, the one with silicon nitride is selected since it is a good absorber in LWIR band and is a widely used material in IC industry. A novelty in

the current design is the addition of the optical resonant cavity to improve the absorption. Theoretical calculations show that > 85% absorptance is possible with the offered structure.

One of the most important drawbacks of thermal detectors for infrared imaging is the slow response time. The reason behind this is the relatively high heat capacity of the structures that limits the response speed. Silicon nitride, whose specific heat capacity is 974 J/kg.K, can be a good absorber but the required thickness for good absorption is in the order of 500 nm, which results in a large thermal mass. We proposed, for the first time to our knowledge, the use of thin metallic films in combination with optical resonant cavities to achieve good IR absorption while providing very low thermal mass, thus fast response time. Thin metallic films show interesting properties apart from bulk ones that make them a good candidate for IR absorbing applications. As a case study, it is shown that a unity theoretical absorptance is possible with a resonant cavity by using ~50 nm thick Al layer, whose specific heat capacity is 900 J/kg.K. Therefore 10 times reduction in heat capacitance is possible by using thin Al as an absorber. Moreover, in the literature the researchers showed that 17 nm thick Au – with a specific heat capacity of 130 J/kg.K – layer is capable to absorb ~50% of IR radiation even without a resonant cavity. With a resonant cavity it is possible to enhance the absorption close to unity. That implies a 220x reduction in the heat capacitance and the response time. We have sufficient evidence from the literature that thin metal IR absorber and the resonant cavity concepts should work as proposed, however, the experimental verification remains as future work.

(ii) Thermo – mechanical deflection analysis: Thermo – mechanical response of the detector pixels are presented with analytical method that estimates the deflection for n-layer structures as a result of thermal stresses. The analytical results are in good agreement with FEM simulations carried out for the design variations. Before fabricating the detector arrays, both analytical and FEM results are compared with the experimental data obtained from a

test structure to show the accuracy of the models. Optimization is focused on maximizing the possible deflection for a fixed pixel area. The results of this study will soon be submitted to the AIP Journal of Applied Physics.

The structures that are responsible for the deflection of the pixels are bimaterial cantilevers which are attached to single layer cantilevers to provide thermal isolation, which is the most important parameter that determines the noise performance of the detector. Noise components for the detector array are presented and it is shown that the detectors are thermal fluctuation noise limited.

(iii) Optical readout design: It is proposed to measure the deflection of the pixels by optical means. The proposed architecture for that purpose is pixel level micro – interferometers with diffraction gratings. This method was successfully implemented for the capacitive ultrasound transducers designed and fabricated by Prof. Levent Degertekin's group at Georgia Institute of Technology, Atlanta. Such a readout method offers an atomic level displacement measurement. Therefore it is possible to detect the temperature difference on the target with a resolution on the order of mK (i.e., temperature resolution of a few 10s of μK at the detector). The analytical model explaining how that method works is presented together with the experimental results obtained with the capacitive transducers. Two array readout architectures are proposed: VCSEL and photo diode array based optoelectronic readout, and the MEMS scanner-based readout. MEMS scanner based readout is easily scalable up to SVGA resolution using existing state-of-the art MEMS scanners. The scheme simplifies the system as no electronic wires are needed at the FPA for the readout. The only thing that might be needed at the FPA is electrostatic or electromagnetic tuning mechanism to tune the air gap for optimal pixel performance and to improve the pixel uniformity.

Microfabrication: The designed detectors were fabricated at Microelectronics Research Center, Georgia Institute of Technology, Atlanta. A 4-mask process is developed using standard IC materials for the microfabrication. The pixels were fabricated on top of a transparent (Quartz) substrate using low temperature processing steps. The fabricated structures look good under the microscope; however, we haven't been able to complete the thermal tests. Our initial tests will be performed in ambient pressure using TEC and by directly heating the substrate and later by localized heating using IR lenses and targets. In the future, a packaging solution that includes TEC and 1mTorr vacuum, where one side is IR window and the other side is a visible window need to be developed. We expect the initial tests will be completed during the next few months.

Fabricated devices do not include integrated readout electronics or the special packaging. As a future work, the fabricated FPAs can be integrated to additional chips including VCSELs and photodiodes or alternatively can be integrated with a scanned beam readout architecture. After integrating with the readout architecture and the proper package, we expect to be able to obtain thermal images.

APPENDICES

A.1 Mask Layouts

The mask set designed for the microfabrication of the detector arrays is given in this section. Four quartz optical photolithography masks with a minimum linewidth of 2 μm were designed and the masks were manufactured by Adtek Photomask, Montreal, QC, Canada.

A.1.1 Overall View

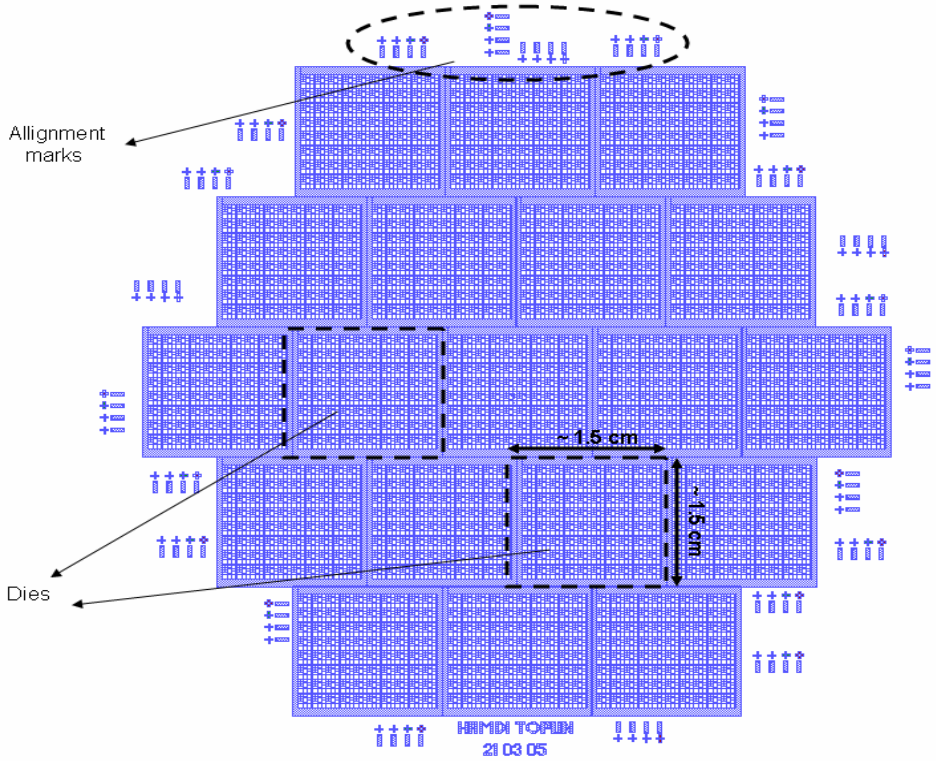

Fig.A.1 General view of mask layouts with clearly indicating the dies and alignment marks

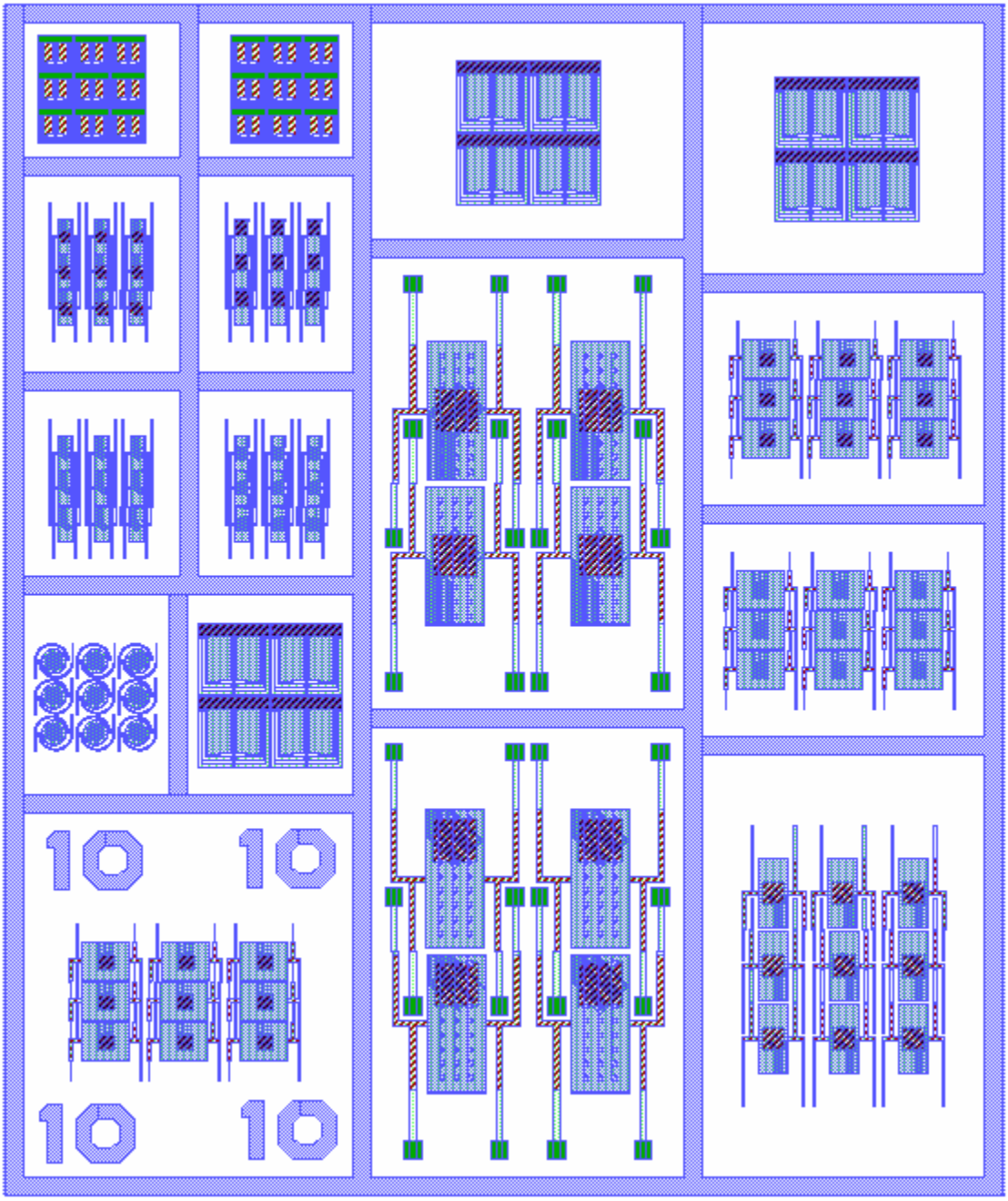

Fig.A.2 Unit cell in one die including all design variations

A.1.2 Pixels of Detector Arrays

Mask layouts for the unit cells of the different design variations are given below. Here different colors represent separate photolithography masks. Each material associated with the masks are labeled on the figures together with a scale in μm.

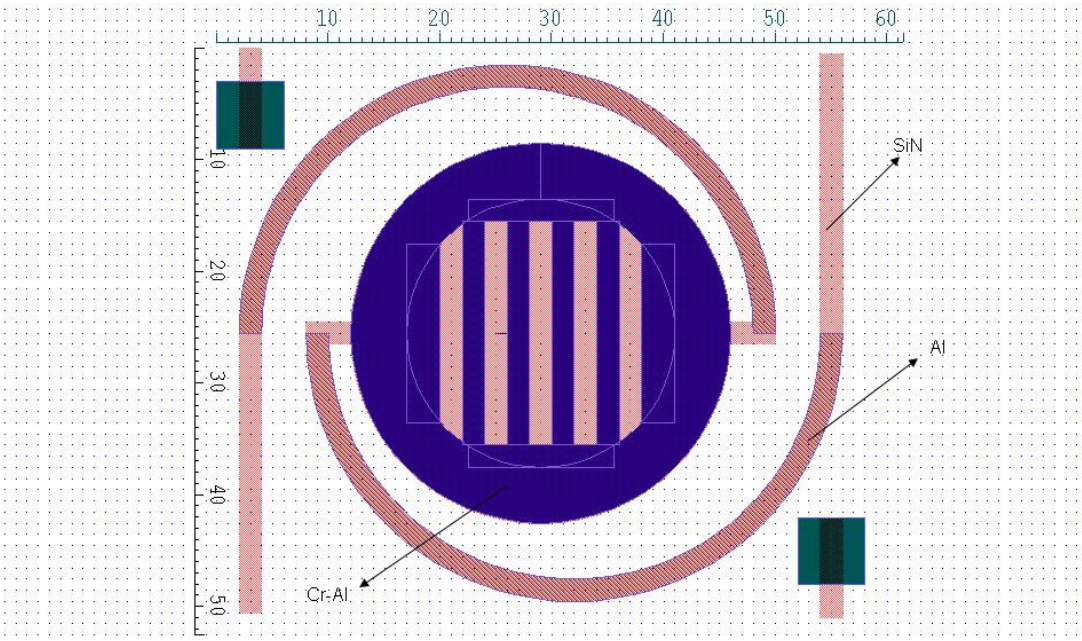

(a)

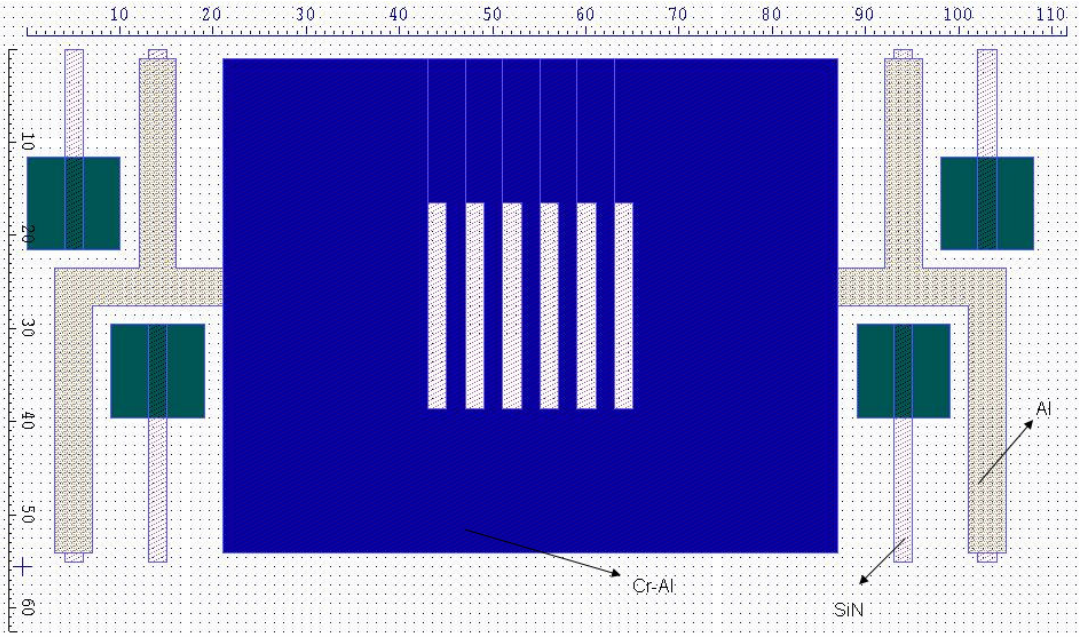
10
20
30
40
50
60
70
80
90
100
110
Al
Cr-Al
SiN

(b)

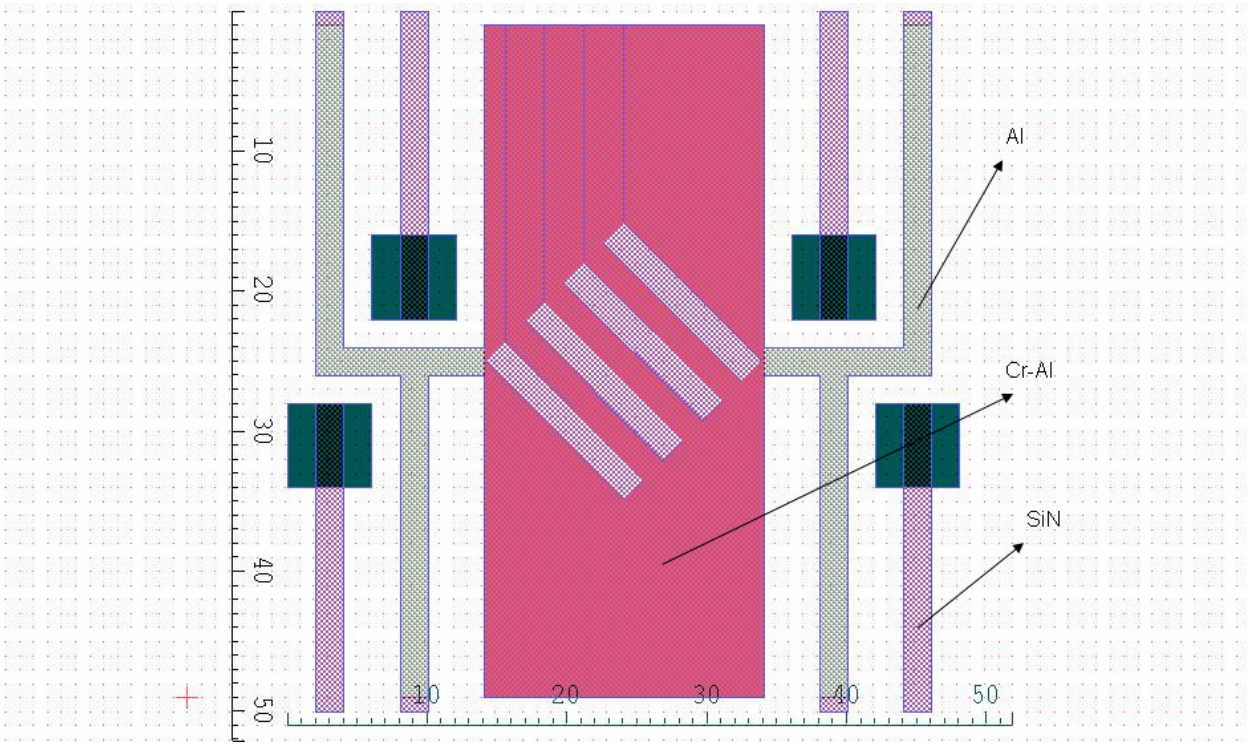
Al
Cr-Al
SiN
10
20
30
40
50

(c)

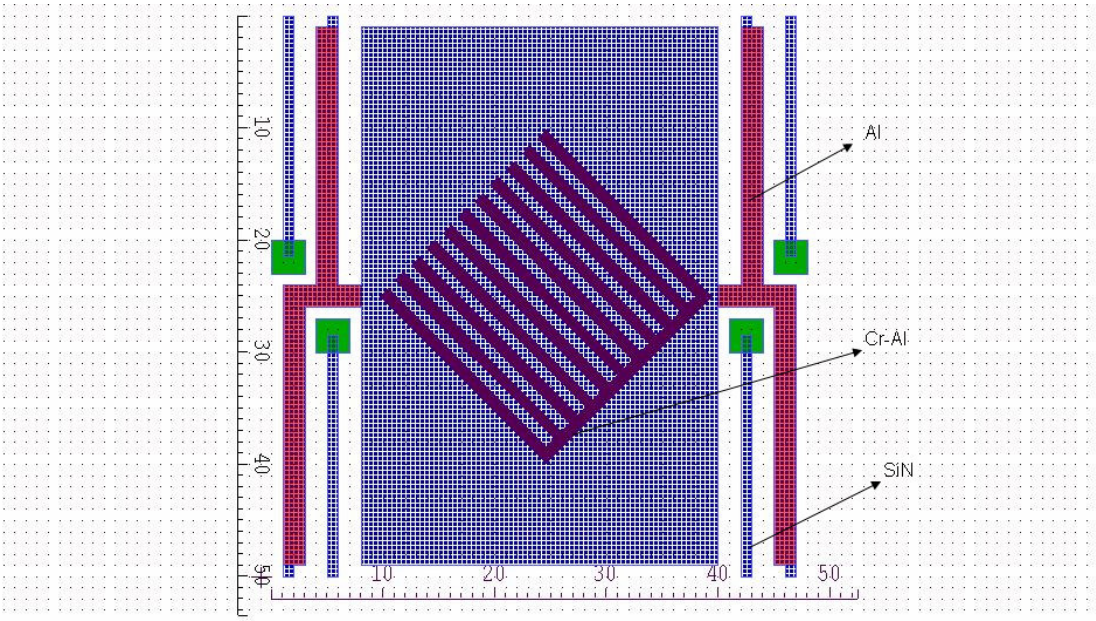

(d)

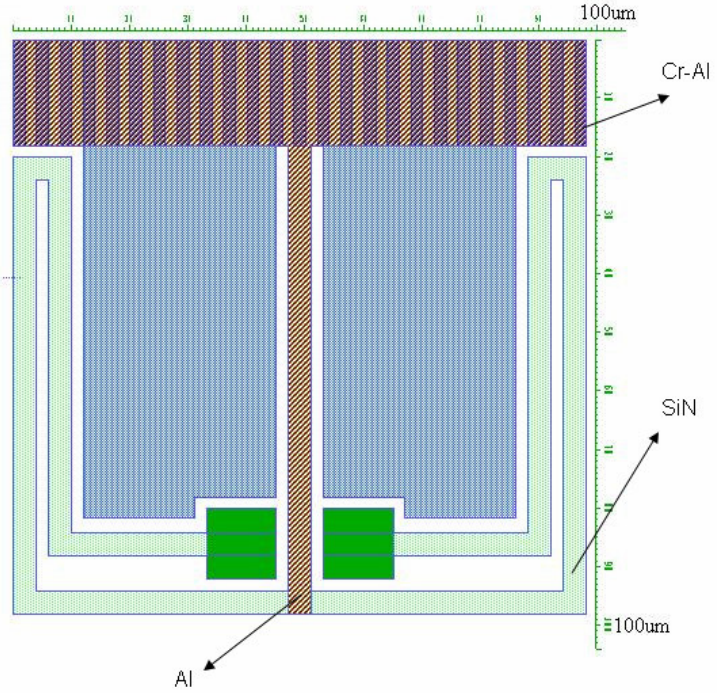

(e)

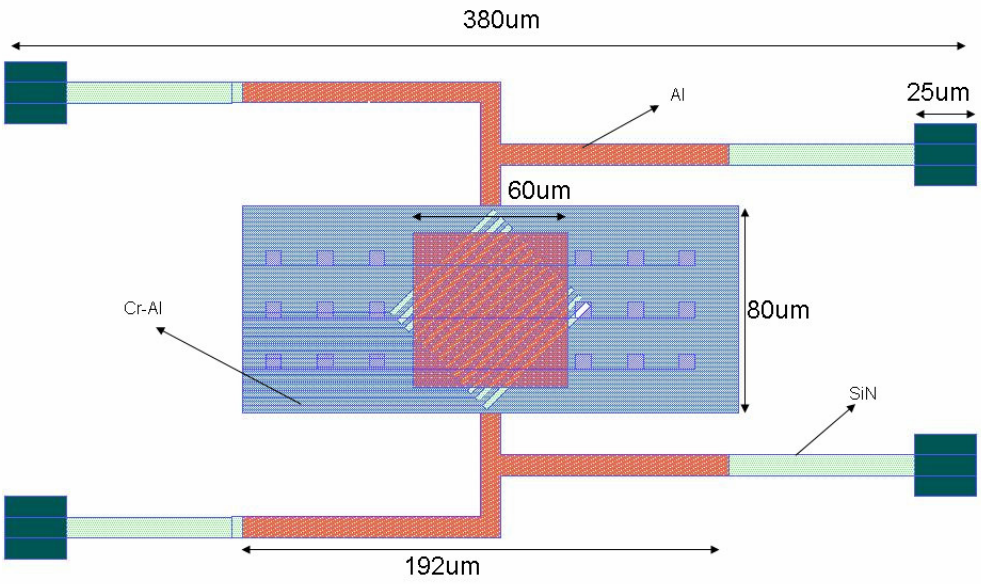
380um
Al
25um
60um
Cr-Al
80um
SiN
192um

(f)

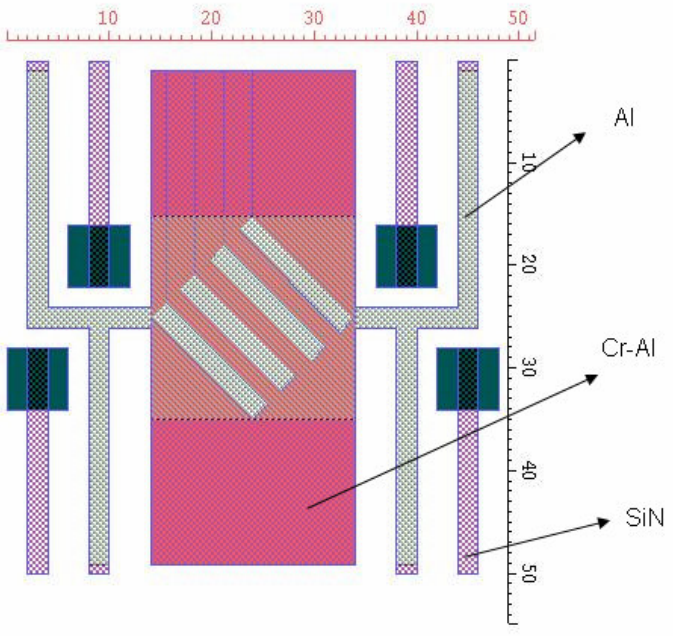
10
20
30
40
50
Al
Cr-Al
SiN

(g)

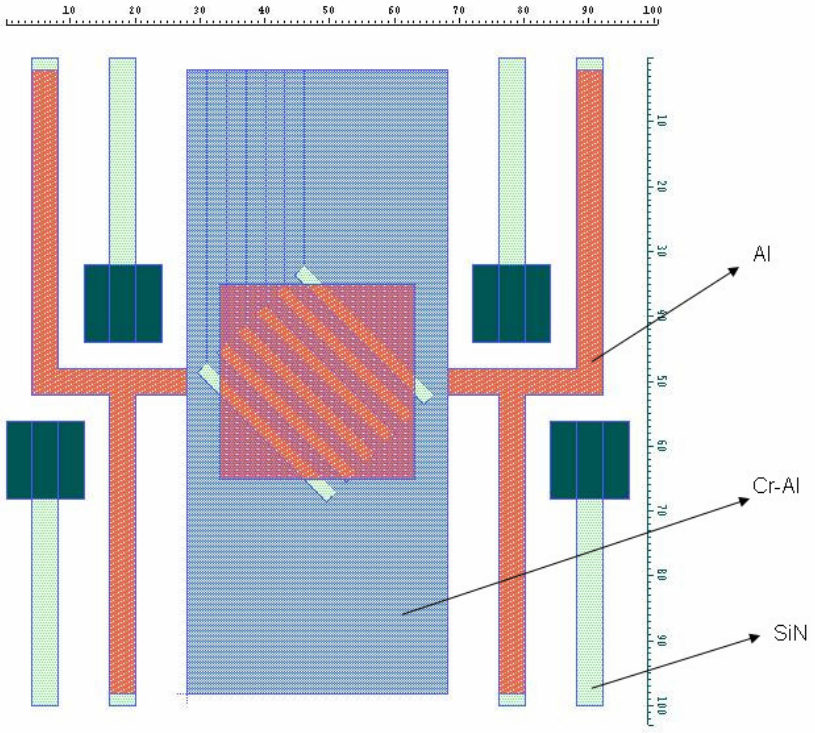

(h)

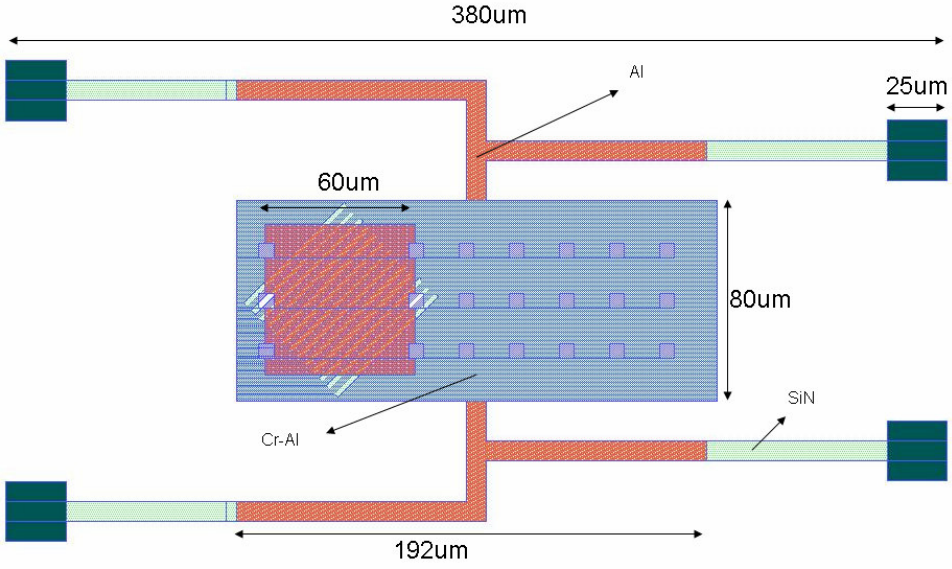

(i)

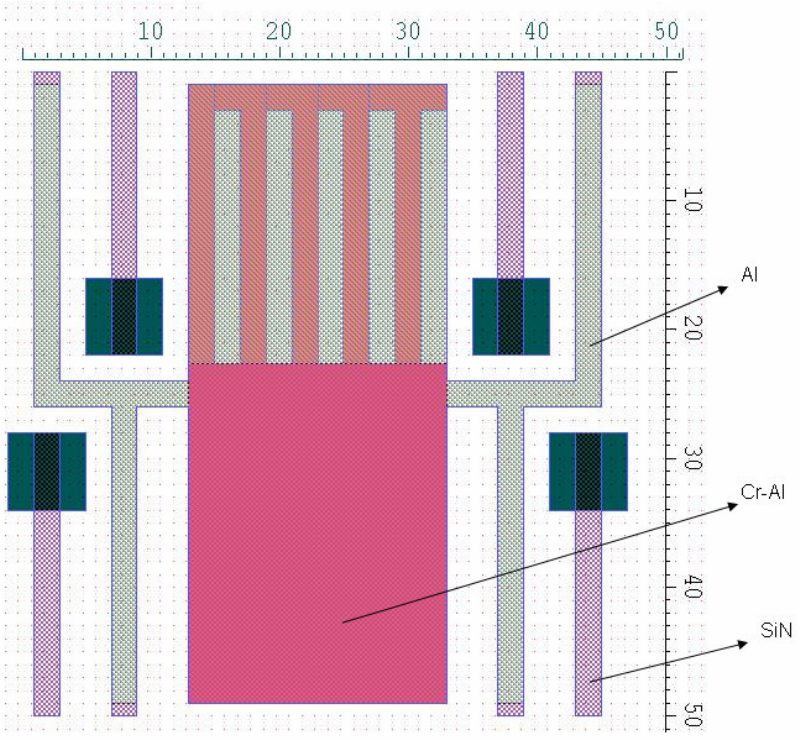

(j)

Fig.A.3 Unit cells of each different design variations

VITA

Hamdi Torun was born in Ankara, Turkey in 1981. He received his B.Sc. degree from Middle East Technical University, Ankara in 2003. He worked in Aselsan Electronic Industries Inc., Ankara as a student technical staff (8/2002 – 7/2003) and then as an analog design engineer (7/2003 – 9/2003). He then joined Optical Microsystems Laboratory (OML) of Koç University, Department of Electrical Engineering as a graduate student. He worked in Georgia Institute of Technology, Department of Mechanical Engineering as a visiting research assistant (3/2005 – 7/2005). Hamdi Torun is a student member of SPIE and IEEE.